STRUCTURAL AND FUNCTIONAL STUDIES OF THE MUNC13 MUN DOMAIN

AND THE RIM C_2B DOMAIN

APPROVED BY SUPERVISORY COMMITTEE

Jose Rizo-Rey, Ph.D., Advisor

Helmut Krämer, Ph.D., Committee Chair

Ilya Bezprozvanny, Ph.D.

Yuh Min Chook, Ph.D.

Jane Johnson, Ph.D.

Diana Tomchick, Ph.D.

DEDICATION

To my family, friends and all the people from my hometown, Cenxi

STRUCTURAL AND FUNCTIONAL STUDIES OF THE MUNC13 MUN DOMAIN AND THE RIM C_2B DOMAIN

by

RONG GUAN

DISSERTATION

Presented to the Faculty of the Graduate School of Biomedical Sciences

The University of Texas Southwestern Medical Center at Dallas

In Partial Fulfillment of the Requirements

For the Degree of

DOCTOR OF PHILOSOPHY

The University of Texas Southwestern Medical Center at Dallas

Dallas, Texas

December, 2007

Copyright

by

RONG GUAN, 2007

All Rights Reserved

ACKNOWLEDGEMENTS

First, I would like to thank my dissertation advisor, Dr. Jose Rizo-Rey for his insightful guidance and continuous support during all these years. He is a truly terrific mentor. He has always been excited and encouraging about every result I obtained and always willing to discuss my project to provide insightful suggestions. He was able to recognize my strengths while at the same time help me to improve on my weaknesses. He also fosters a very nice lab environment which I am happy to work in. I have learned a lot of useful technical skills as well as a great scientific attitude from him. I could never thank him enough for his guidance and support.

I thank my dissertation committee members, Dr. Helmut Krämer, Dr. Ilya Bezprozvanny, Dr. Yuh Min Chook, Dr. Jane Johnson and Dr. Diana Tomchick for their continuous support and helpful suggestions. I thank our collaborators Dr. Diana Tomchick and Dr. Mischa Machius in the Structural Biology Laboratory (SBL) of UT Southwestern for their help with X-ray crystallography. I thank our long-term collaborator Dr. Thomas Südhof in the Department of Neuroscience of UT Southwestern for his continuous support and providing helpful suggestions. I also thank my previous mentor Dr. Zhjijian Chen in the Department of Molecular Biology of UT Southwestern. I cherish everything I learned from him and his laboratory.

I would also like to give my thanks to current and past members of the Rizo-Rey

laboratory, big thanks for their keeping work fun. They have been my good friends and teachers.

My deepest thanks go to my family — my parents, Yongming Guan and Honglan Ye, my husband, Han Dai, my brother, Zhi Guan as well as my sisters, Xuan Guan, Qing Guan, Ning Guan, for their love, encouragement and support through my life. My success is owed to them.

Finally, I want to thank all the people from my hometown — Cenxi. They recognize the importance of me. I want to bring glory to my hometown. This idea helps me to overcome all of my frustrations.

STRUCTURAL AND FUNCTIONAL STUDIES OF THE MUNC13 MUN DOMAIN AND THE RIM C_2B DOMAIN

Publication No. _____

Rong Guan, Ph.D.

The University of Texas Southwestern Medical Center at Dallas, 2007

Supervising Professor: Jose Rizo-Rey, Ph.D.

Neurotransmitter release is essential for normal brain function and is achieved through exocytosis of synaptic vesicles. Many proteins are involved the regulation of neurotransmission. The central fusion machinery includes the SNARE proteins and Munc18-1. Besides these universal components, many other neuronal specific proteins are also involved in regulating Ca^{2+}-triggered neurotransmitter release, such as the key priming factors RIMs and Munc13s. Munc13s are essential for vesicle priming. RIMs form a protein scaffold in the presynaptic nerve terminal. My studies have focused on the structures and

functions of the Munc13 MUN domain and the RIM C_2B domain.

I have studied the structure and function of the Munc13 MUN domain. On one hand, I have tried to determine the three dimensional structure of the Munc13 MUN domain by X-ray crystallography. I have successfully obtained crystals of the Munc13-1 MUN domain, Munc13-3 MUN domain and a fragment containing the Munc13-1 C_1, C_2B and MUN domains. These crystals will be further optimized to enable structure determination. On the other hand, I have tried to identify the binding partners of the MUN domain using various methods. Cross-linking experiments revealed an interaction between the Munc13-1 MUN domain and endogenous Munc18-1. In addition, cofloatation assays revealed an interaction between MUN and reconstituted SNARE complex. Detailed analysis using cofloatation assays suggested both MUN and complexin can compete with Munc18-1 for SNARE complex binding in a membrane environment. Our studies also suggested that the membrane environment can modulate the strength of protein-protein interactions remarkably, which emphasize the importance to include membranes in the studies of protein-protein interactions involved in neurotransmission.

I have also analyzed the structural and biochemical properties of the RIM1 C_2B domain. NMR spectroscopy and FRET experiments demonstrated no interaction between the RIM1 C_2B domain and Ca^{2+}, phospholipids, or its putative binding partners, synaptotagmin 1 and liprins. X-ray crystallography revealed the existence of a RIM1 C_2B domain homodimer, which was confirmed by analytical ultracentrifugation and NMR spectroscopy. Our results suggested a model that RIM1 C_2B dimerization might facilitate the Munc13 C_2A homodimer to Munc13 C_2A/RIM zinc finger heterodimer switch during synaptic vesicle priming.

TABLE OF CONTENTS

PRIOR PUBLICATIONS

Haiyan Wang, Rong Guan, Chunhai Fan, Dexu Zhu, Genxi Li. A hydrogen peroxide biosensor based on the bioelectrocatalysis of hemoglobin incorporated in a kieselgubr film. *Sensors and Actuators B*, 2002, 84: 214-218

Chunhai Fan, Jun Zhong, Rong Guan and Genxi Li. Direct electrochemical characterization of Vitreoscilla sp. Hemoglobin entrapped in organic films. *Biochimica et Biophysica Acta - Proteins and Proteomics*, 2003, 1649(2): 123-126

Xin Zhao, Jian Liu, Rong Guan, Yi Shen, Ping Xu, Jianguo Xu. Estrogen affects BDNF expression following chronic constriction nerve injury. *Neuroreport,* 2003, 14(12):1627-31.

Jayeeta Basu, Nan Shen, Irina Dulubova, Jun Lu, Rong Guan, Oleg Guryev, Nick V Grishin, Christian Rosenmund, Josep Rizo. A minimal domain responsible for Munc13 activity. *Nature structural & molecular biology*, 2005 12(11):1017-8

Rong Guan, Han Dai, Diana R. Tomchick, Irina Dulubova, Mischa Machius, Thomas C. Südhof, Josep Rizo. Crystal Structure of the RIM C_2B domain at 1.7 Å resolution. *Biochemistry*, 2007 46(31): 8988-98

Rong Guan, Han Dai, Josep Rizo. Binding of the Munc13-1 MUN Domain to Membrane-Anchored SNARE Complexes. (Submitted)

LIST OF FIGURES

LIST OF TABLES

LIST OF DEFINITIONS

1D	one -dimensional
2D	two-dimensional
3D	three-dimensional
APS	Advanced Photon Source
ASU	asymmetric unit
BoNT	botulinum neurotoxin
BS3	Bis (Sulfosuccinimidyl) suberate
C.elegans	*Caenorhabditis elegans*
CAZ	cytoskeletal matrix at the active zone
CCP4	the collaborative computational project number 4
CD	circular dichroism
CIP	calf intestine phosphatase
CMC	critical micellar concentration
CORD7	autosomal dominant cone-rod dystrophy
DAG	diacylglycerol
Dansyl	5-(dimethylamino)naphthalene-1-sulfonyl
DLS	dynamic light scattering
d_{min}	high resolution limit (Å)
DOPE	1,2-dioleoyl phosphatidylethanolamine
DOPS	1,2-dioleoyl phosphatidylserine

DTT	dithiothreitol
E. coil	*Eschericheria coli*
EDC	1-Ethyl-3-[3-dimethylaminopropyl]carbodiimide hydrochloride
EDTA	ethylene diamine tetraacetic acid
EGTA	ethylene glycol-bis (β-aminoethyl ether)-tetraacetic acid
EM	electron microscopy
EPR	electron paramagnetic resonance
FPLC	fast performance liquid chromatography
FRET	fluorescence resonance energy transfer
GAP	GTPase activating factor
GDI	GDP dissociation inhibitor
GEF	guanine nucleotide exchange factor
GST	glutathione-S-transferase
HEPES	N-(2-hydroxyethyl) piperizine-N'2-ethanesulphonic acid
HSQC	heteronuclear single quantum correlation
IPTG	isopropyl β-D-thiogalactopyranoside
ITC	isothermal titration calorimetry
Ka	association constant
Kd	dissociation constant
kDa	kilodalton
LB	luria broth

LMV	large multilamellar vesicle
LTP	long-term potentiation
LUV	large unilamellar vesicle
MAD	multiple wavelength anomalous dispersion
MBP	myelin basic protein
MES	2-(N-morpholino)ethanesulfonic acid
MHD	Munc13 homology domain
MIR	multiple isomorphous replacement
NHS	N-hydroxysuccinimide
Ni-NTA	nickel-nitrilotriacetic acid
NMR	nuclear magnetic resonance
NSF	N-ethylmaleimide-sensitive factor
OD	optical density
PAGE	polyacrylamide gel electrophoresis
PBS	phosphate buffered saline
PC	phosphatidylcholine
PCR	polymerase chain reaction
PDB	protein data bank
PE	phosphatidylethanolamine
PEG	polyethylene glycol
PKC	protein kinase C

PMSF	phenylmethylsulphonyl fluoride
POPC	1-palmitoyl, 2-oleoyl phosphatidylcholine
ppm	parts per million
PS	phosphatidylserine
RIM	Rab3-interacting molecule
RIM-BP	RIM-binding protein
rms	root mean square
rpm	revolutions per minute
SAD	single wavelength anomalous dispersion
SBC	Structural Biology Center
SDS	sodium dodecylsulfate
SeMet	Selenomethionine-derivatized
SIR	single isomorphous replacement
SM	Sec1/Munc18
SNAP	soluble NSF attachment protein
SNAP-25	synaptosome-associated protein of 25 kDa
SNARE	SNAP receptor
TCA	trichloroacetic acid
TCEP	Tris(2-carboxyethyl) phosphine
TeNT	tetanus toxin
TEV	tobacco etch virus

Tris	tris (hydroxymethyl) aminomethane
t-SNARE	target membrane SNARE
UV	ultraviolet
VAMP	vesicle-associated membrane protein
v-SNARE	vesicle SNARE
β-OG	octyl-β-D-glucopyranoside

Chapter 1 General Introduction

1.1 The brain

As we all know, all the feelings that we carry are a set of functions marshaled by the brain. Although primitive animals such as sponges do not have a brain, the brain is very important for advanced animals. Invertebrates usually have either a centralized brain or collections of individual ganglia. In all vertebrates, the brain is responsible for behavior, including not only relatively simple motor behaviors such as looking, hearing, and tasting, but also delicately affective behaviors such as feeling, thinking and learning.

Figure 1.1 shows the morphology of the human brain and the rat brain. The brain is composed of two main types of cells –neurons and glial cells. Neurons are the functional units that receive and send electrochemical signals while the glial cells mainly function to provide a supporting environment for the neurons. Although these basic units are very simple, they can achieve very complex behavior because a large number of neurons act simultaneously. The primary sensory apparatus senses the environmental stimuli and sends signals to the brain, where the signals are processed and broken down into components that produce perceptions, part of which will become memories and will be retained in the brain. The brain then sends orders to coordinate the bodily responses, such as muscle movements, based on this processed information. To achieve these extremely accurate events, the brain has been developed to be very complex. For instance, there are more than 100 billion neurons

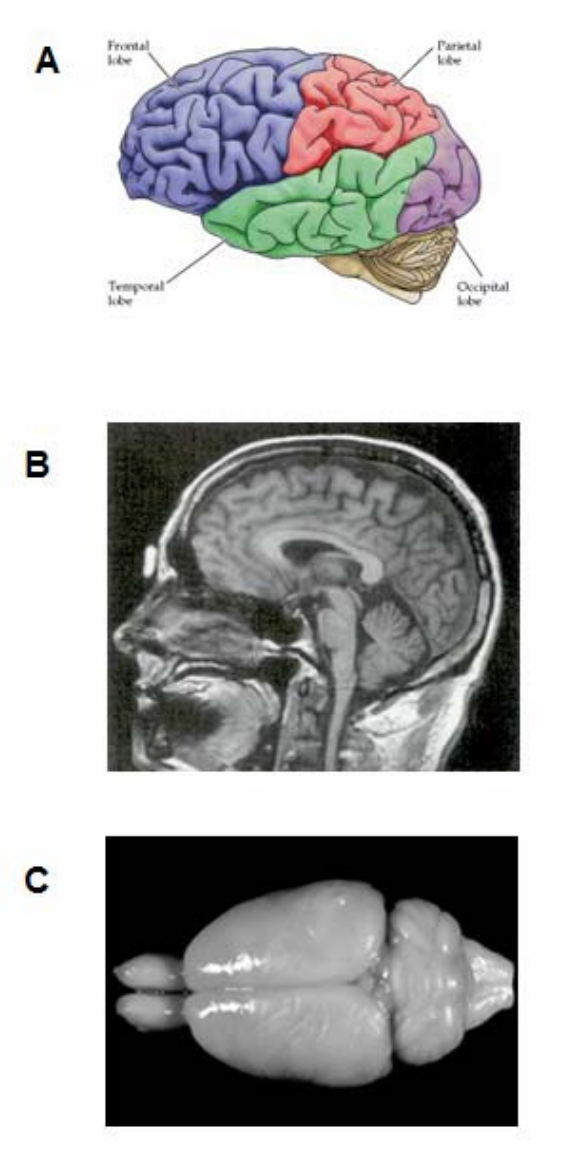

Figure 1.1 Diagrams of the brain

(A) Diagram of the human brain. Lateral view of the human brain shows the four lobes of the brain. (Neuroscience, second edition, Purves et al., 2001)

(B) MRI image of the human brain

(C) Picture of the top view of the rat brain

in the human brain. Each neuron is connected with up to 10 thousand other neurons, forming a very complex communication network.

1.2 Neuron

Neurons (also referred to as nerve cells, neurones or nerve fibers) are electrically functional cells in the nervous system that process and transmit information. A typical neuron consists of a cell body (also called soma), ramified dendrites and an axon (Figure 1.2) (Kandel et al., 1991). The cell body usually is triangular or pyramidal, and contains the nucleus and perikaryon. The cell body is the place where the synthesis of neuronal proteins and membranes as well as metabolism occurs. Each cell body produce several dendrites and the dendrites, as the name indicates, forms a tree-like structure. The cell body also gives rise to one axon in each neuron. The axon usually exists as a tubular projection and can be as long as five meters in some organisms. The dendrite is the main component for receiving input signals, while the axon is the main conducting unit of the neuron. Usually, the neurons receive input signals from the dendritic branch or sometimes from the cell body and transduce the output signal through the axon to other neurons or non-neuronal effector cells.

Even though all the neurons share the basic aforementioned architecture, a significant heterogeneity in their morphology and function exist among different parts of the nervous system and across different species. Neurons can be classified into perhaps as many as 10 thousand different types. Different neurons are precisely connected with each other or with

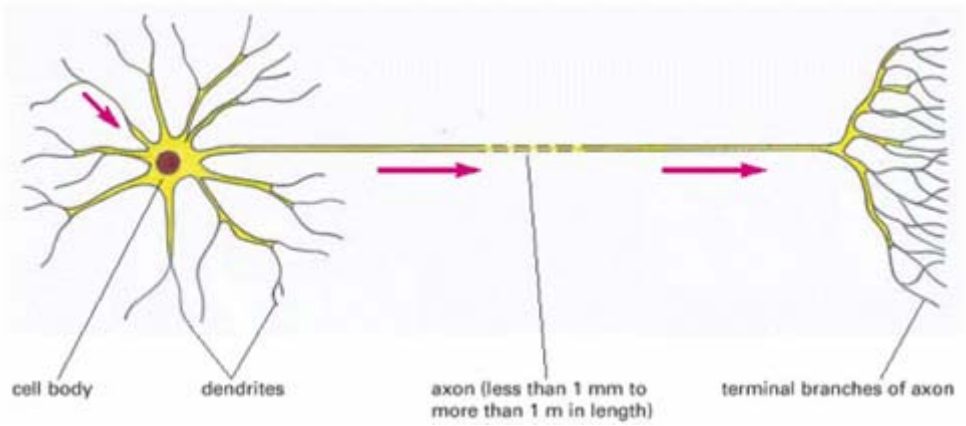

Figure 1.2 Diagram of a typical vertebrate neuron

The cell body, dendrites, axon and the terminal branches of the axon of a typical vertebrate neuron are shown. The red arrows indicate the direction of the signal flow, from the multiple dendrites to the terminal branches of the axon. (Molecular Biology of the Cell, fourth edition, Alberts et al., 2002).

sensory and effector cells, which enables the brain to perform very different and intricate functions.

1.3 The synapse and the active zone

Interneuronal communication is essential for normal brain function. Perturbation of interneuronal communication can lead to the occurrence of many neuropsychiatric diseases, such as schizophrenia, Parkinson's disease, and Huntington's disease. The axon terminal of each neuron is connected to the dendrites of other neurons across a small cleft, termed a synapse. Synapse is a special type of cell-cell contact responsible for reliable and highly-regulated transduction of signals from a neuron to other neurons or effector cells. Synapse formation involves two neurons, which are named presynaptic and postsynaptic neurons, respectively, according to the directionality of the signal transduction. The neuron providing the axon to send information is referred to as the presynaptic neuron while the neuron providing dendrites to receive information is referred to as the postsynaptic neuron. The unidirectionality of signal transmission occurring at synapses, from the presynaptic axon to the postsynaptic dendrites, is integrated with the unidirectional signal transmission within a single neuron to maintain the directionality of signal transmission in the nervous system.

There are two types of synapses, electrical synapse and chemical synapse, depending on the properties of the signals transduced between neurons. In electrical synapse, also called gap junction, the electrical signal is directly transmitted from the presynaptic neuron to the

postsynaptic neuron through connected ion flux. In chemical synapse, the electrical signal is first converted to a chemical signal through the release of chemical messengers, known as neurotransmitter, from the presynaptic neuron. The signal is then transmitted to the postsynaptic neuron through binding of neurotransmitters with their cognate receptors, which elicits ion channel opening and converts the chemical signal back to an electric one. My studies were focused on the chemical synapses.

Electron microscopy studies of chemical synapses have revealed a characteristic anatomy (Figure 1.3). Electron dense materials can be observed on both presynaptic and postsynaptic sides of a synapse, which were referred to as the presynaptic active zone and postsynaptic density, respectively. The active zone is a special region of the presynaptic axon terminal plasma membrane and is highly rich in various proteins. The neurotransmitters reside in small membrane-bound vesicles about 40 nm in diameters, the so-called synaptic vesicles, which were observed to cluster around the active zone, where the synaptic vesicles dock and release the neurotransmitters. The postsynaptic density is rich in various receptors to receive chemical signals. The synapses can be either excitatory or inhibitory, depending on whether the firing of the presynaptic neuron increase or decrease the probability of the firing of the postsynaptic neuron.

1.4 Neurotransmitter release

Neurotransmitter release is the key step for chemical synapse signal transmission.

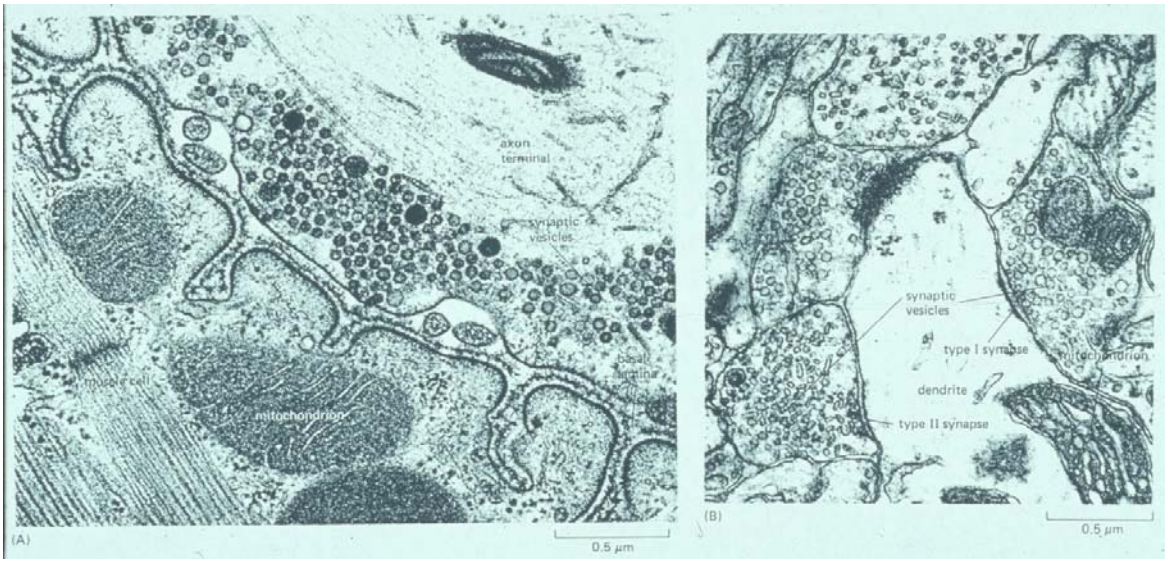

Figure 1.3 Electron micrographs of chemical synapses

(A) Electron micrograph of neural neuromuscular junction, the synapse of the axon terminal of a motor neuron with the motor end plate.

(B) Electron micrograph of chemical synapses. A cross section of a dendrite forming several chemical synapses with presynaptic axon terminals filled with synaptic vesicles. (Molecular Biology of the Cell, fourth edition, Alberts et al., 2002).

Neurotransmitter release is archived through Ca^{2+}-triggered exocytosis of synaptic vesicles at the presynaptic plasma membrane. Initially, the synaptic vesicles are filled with chemical neurotransmitters by the vesicular transporters. The loaded vesicles then dock at the presynaptic active zone, presumably through specific protein-protein interactions between the two opposing membranes. The docked vesicles undergo an ATP-dependent priming process, which make them competent for fusion. When the action potential is transmitted along the axon to the nerve terminal, voltage-gated Ca^{2+}-channels are activated, which results in massive Ca^{2+} influx into the nerve terminal and elevation of intracellular Ca^{2+} concentration. The Ca^{2+} influx triggers the exocytotic fusion of synaptic vesicles with the presynaptic plasma membrane and the consequent neurotransmitter release. The process is extremely fast, occurring less than 0.5 ms after Ca^{2+} influx (Sabatini and Regehr, 1999). After fusion, the synaptic vesicle proteins are resorted and undergo endocytosis to be recycled. The released neurotransmitters diffuse across the extracellular space between the presynaptic and postsynaptic neurons, the so-called synaptic cleft, and bind to their cognate receptors on the postsynaptic density to elicit downstream signal transduction and propagation (Sudhof, 1995; Sudhof, 2004) (Figure 1.4).

1.5 The proteins involved in neurotransmitter release

Neurotransmitter release is an exquisitely regulated process that is essential to interneuronal communication (Jahn and Sudhof, 1999). Many proteins are involved in this process, including the general fusion machinery that participates in synaptic vesicle

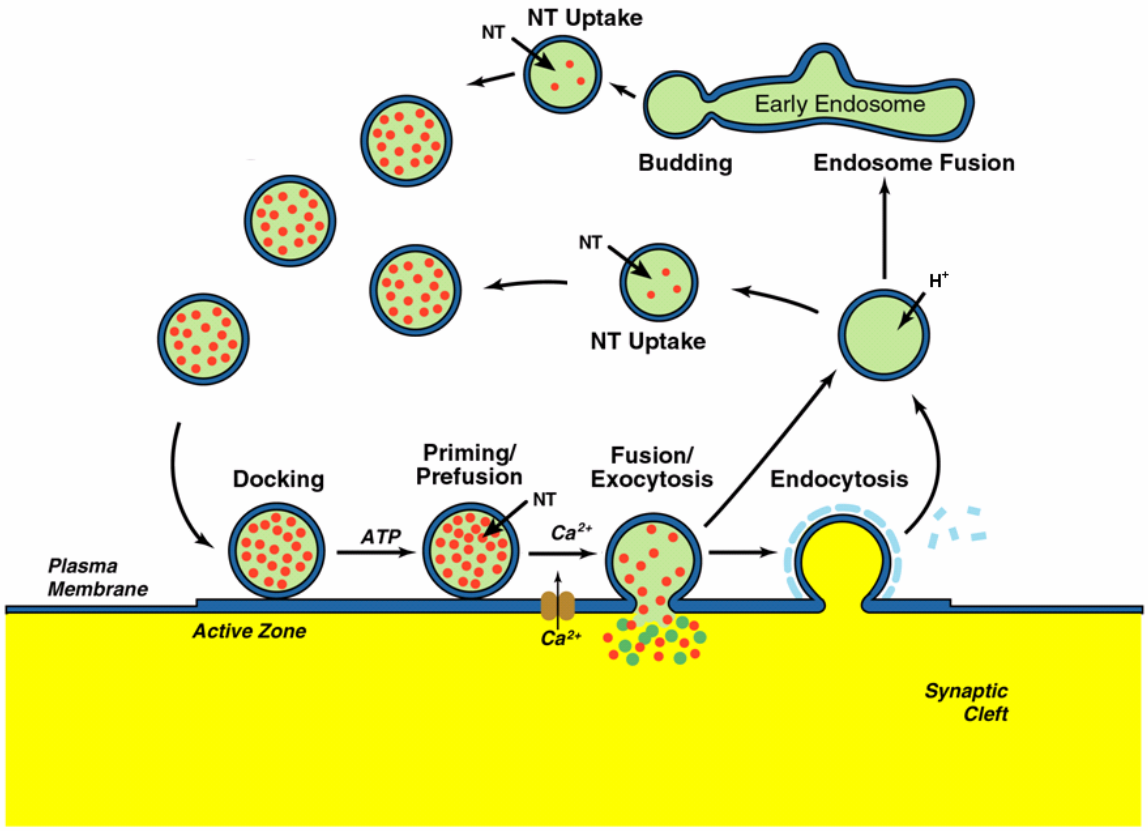

Figure 1.4 Synaptic vesicle cycle

Neurotransmitter-loaded synaptic vesicles dock at a specialized region of the presynaptic plasma membrane, called the active zone. The docked vesicles undergo a priming process, which makes them competent for fusion. Upon Ca^{2+} influx, the synaptic vesicles fuse with the presynaptic plasma membrane and release the neurotransmitters into the synaptic cleft. Clathrin-mediated endocytosis recycles the synaptic vesicle membrane and proteins to maintain the synaptic vesicle cycle (Sudhof, 1995; Sudhof, 2004).

exocytosis: the soluble N-ethylmaleimide-sensitive factor (NSF) attachment protein (SNAP) receptors (SNAREs), the Sec1/Munc18-1 homologs (SM proteins), and small GTPases of the Rab3 family (Bennett and Scheller, 1993; Ferro-Novick and Jahn, 1994). Besides these universal components, many other neuronal specific proteins are also involved in regulating Ca^{2+}-triggered neurotransmitter release such as the Ca^{2+} sensor synaptotagmins and the small SNARE-associating proteins known as complexins (Sollner, 2003; Sudhof, 2004). At the presynaptic active zone, a protein network called cytoskeletal matrix at the active zone (CAZ) is assembled to organize the synaptic vesicle cycle. The protein network enriched at the active zone includes several large multidomain proteins such as Munc13s, Rab3-interacting molecules (RIMs), CAST/ERK/ELKS proteins, Bassoon and Piccolo, and the liprins (Schoch et al., 2002). These active zone proteins are critical for the diverse functions performed by the presynaptic active zone.

1.5.1 SNARE proteins

SNARE proteins are a large family of proteins involved in a variety of membrane trafficking processes. A critical role of SNARE proteins is to mediate the membrane fusion event between the intracellular transport vesicles and the target compartment membrane. The best-characterized SNARE proteins are those involved in neurotransmitter release, which include the synaptic vesicle protein synaptobrevin 2/vesicle-associated membrane protein 2 (VAMP2), the presynaptic plasma membrane proteins syntaxin 1A and synaptosomal-associated protein of 25 kDa (SNAP-25) (Baumert et al., 1989; Bennett et al., 1992; Oyler et

al., 1989; Trimble et al., 1988). Neuronal SNARE proteins are the targets of proteolytic cleavage by clostridial neurotoxins such as botulinum toxin (BoNT) and tetanus toxin (TeNT), which block neurotransmitter release and cause paralysis (Blasi et al., 1993a; Blasi et al., 1993b; Link et al., 1992; Schiavo et al., 1992).

SNARE proteins are classified into two categories, v-SNAREs and t-SNAREs, depending on their localization (Sollner et al., 1993). v-SNAREs refer to those SNARE proteins residing on the transport vesicle, e.g. synaptobrevin, whereas t-SNAREs refer to those SNARE proteins residing on the target membrane, e.g. syntaxin and SNAP-25. All SNARE proteins contain a characteristic cytoplasmic heptad-repeat motif, called the SNARE motif, which is usually 60-70 residues long (Hayashi et al., 1994; Jahn and Sudhof, 1999). Synaptobrevin 2 contains an N-terminal SNARE motif and a C-terminal transmembrane anchor (Trimble et al., 1988). Syntaxin 1A contains an N-terminal H_{abc} domain, a central SNARE motif and a C-terminal transmembrane anchor (Fernandez et al., 1998). SNAP-25 contains two SNARE motifs separated by a long cysteine-rich loop, which is palmytolated to anchor SNAP-25 to the plasma membrane (Hess et al., 1992). The SNARE motifs from synaptobrevin 2, syntaxin 1A and SNAP-25, or more generally, the four SNARE motifs from v- and t-SNARE proteins, can form a highly stable four-helix bundle structure, called the core complex (Hayashi et al., 1994; Fasshauer et al., 1998a) (Figure 1.5). Biochemical analysis showed that the core complex is SDS-resistant and only denatures at temperature higher than 95 ºC (Hayashi et al., 1994; Fasshauer et al., 1998a). Deep-etch electron microscopy and electron paramagnetic resonance (EPR) studies showed a parallel

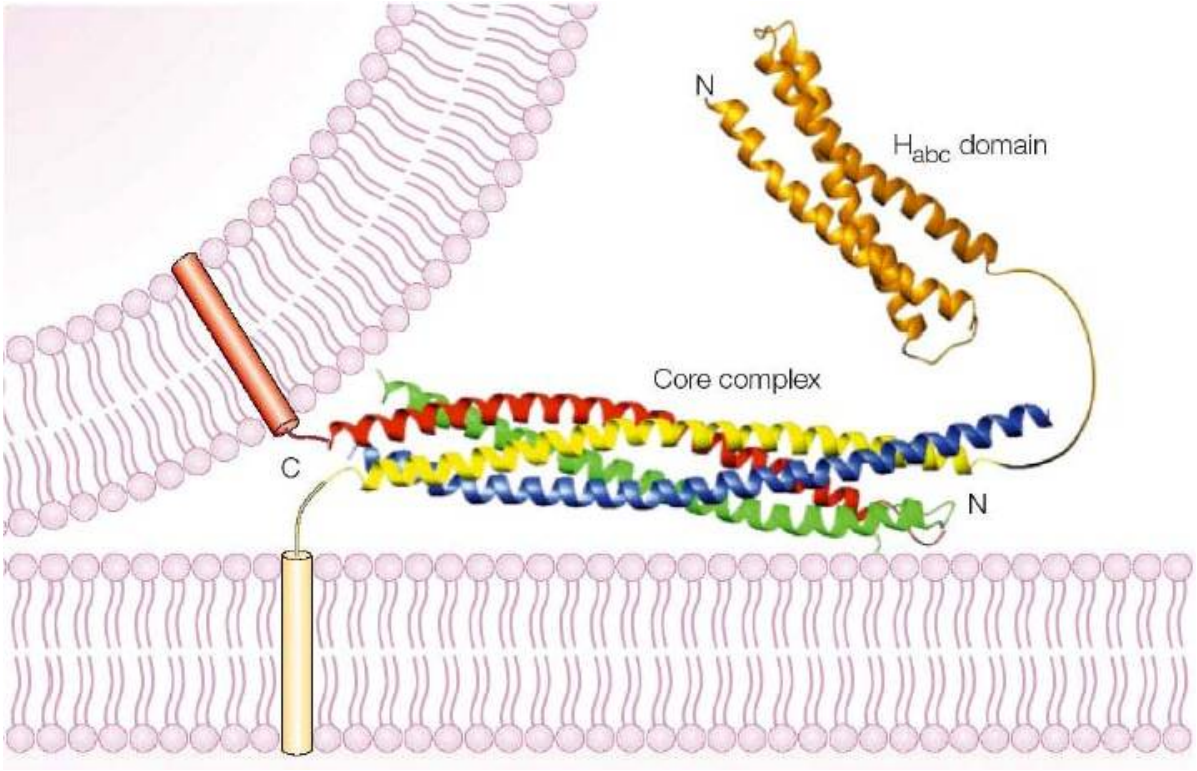

Figure 1.5 The formation of the SNARE complex brings the two opposing membrane to close proximity

The crystal structure of the neuronal SNARE complex together with the syntaxin 1A N-terminal Habc domain are shown with respect to the synaptic vesicle membrane and the presynaptic plasma membrane. The SNARE motifs from syntaxin 1A, synaptobrevin, N-terminal SNAP-25 and C-terminal SNAP-25 are colored in yellow, red, blue, and green, respectively. The syntaxin 1A N-terminal Habc domain is colored in orange. The transmembrane regions of syntaxin 1A and synaptobrevin are represented as cylinders inside the lipid bilayers (Sutton et al., 1998; Fernandez et al., 1998; Rizo and Sudhof, 2002).

arrangement of t-SNAREs and v-SNARE in the assembled SNARE complex, which is confirmed by its crystal structure (Hanson et al., 1997; Poirier et al., 1998b; Sutton et al., 1998). The crystal structure of the neuronal SNARE complex revealed an elongated four-helix bundle of about 12 nm in length intertwined by the four SNARE motifs from synaptobrevin 2, syntaxin 1A and SNAP-25. The binding interface of the SNARE complex is mainly hydrophobic in nature except at the center, where three glutamines from the t-SNAREs and one arginine from the v-SNARE form a central ionic layer, which was called the "zero layer" and has been suggested to be critical for the proper register of the four-helix bundle formation (Fasshauer et al., 1998b; Sutton et al., 1998).

The isolated SNARE motifs are largely unstructured and only adopt a helical conformation upon assembly into the SNARE complex (Fasshauer et al., 1998a; Poirier et al., 1998a). Among the three neuronal SNARE proteins, syntaxin 1A is unique due to the presence of its N-terminal H_{abc} domain. The H_{abc} domain forms an antiparallel three-helix bundle (Fernandez et al., 1998) and can fold back to interact with its own SNARE motif to form a so-called "closed" conformation, which can be stabilized through interaction with Munc18-1 (which is discussed in more detail in next section) (Dulubova et al., 1999). Isolated syntaxin 1A undergoes the open-closed conformation equilibrium in solution. The closed conformation of syntaxin 1A sequesters the SNARE motif from participation in SNARE complex formation whereas its open conformation liberates its SNARE motif to be ready for SNARE complex formation (Dulubova et al., 1999).

In vitro liposome-based fusion assay using reconstituted SNARE proteins showed that SNARE proteins alone could mediate fusion of synaptobrevin-containing v-vesicles and syntaxin/SNAP-25-containing t-vesicles, which led to the notion that SNAREs constitute the minimal machinery necessary for intracellular membrane fusion (Weber et al., 1998). However, the fusion kinetics observed was quite slow and there was no evidence of content mixing and lack of leakiness. Later, independent fusion assay studies using endogenous brain synaptic vesicle and reconstituted syntaxin/SNAP-25-containing t-vesicles revealed no observation of membrane fusion, which challenged the notion that the SNAREs are the minimal fusion machinery (Hu et al., 2002; Kweon et al., 2003; Chen et al., 2006). Recently, studies from Rothman's group and our lab suggested that besides the SNARE proteins, Munc18 might be part of the core of the membrane fusion apparatus (Dulubova et al., 2007).

1.5.2 SM proteins

Sec1/Munc18 (SM) proteins are cytosolic proteins of ca. 65 kDa and are required for all types of intracellular membrane traffic events, similar to the SNAREs (Rizo and Sudhof, 2002; Gallwitz and Jahn, 2003). The first SM protein, UNC18, was identified in genetic screens for uncoordinated locomotion phenotypes of *C. elegans* (Brenner, 1974). Its mammalian homologues identified later are named as Munc18s. In particular, the functional importance of the neuronal SM protein involved in neurotransmitter release, Munc18-1 (also called nSec1 or rbSec1), has been demonstrated by the total abrogation of spontaneous, sucrose-induced and Ca^{2+}-triggered release observed in Munc18-1 knockout mice (Verhage

et al., 2000).

X-ray crystallography and biochemical studies have revealed that Munc18-1 is composed of three domains, forming an arch-shaped structure with a cavity in the middle, and binds tightly through its central cavity to the closed conformation of syntaxin 1, preventing SNARE complex formation (Dulubova et al., 1999; Misura et al., 2000; Yang et al., 2000). Together with the fact that overexpression of the Munc18-1 homologue ROP in *Drosophila* caused a decrease in neurotransmission, this finding suggested an inhibitory role for Munc18-1, which is in contrast to the Munc18-1 knockout phenotype in mice (Wu et al., 1998; Verhage et al., 2000). However, other studies showed that several other SM proteins involved in membrane trafficking between different intracellular compartments bind to a short evolutionarily conserved N-terminal peptide of the cognate syntaxin homologues instead of to the closed conformation, and thus do not interfere with SNARE complex formation (Yamaguchi et al., 2002; Dulubova et al., 2003). To complicate matters further, the yeast SM protein Sec1 was shown to bind to the assembled SNARE complexes (Carr et al., 1999). More recently, several studies suggested that Munc18-1 can also bind to assembled SNARE complexes as well as the N-terminal peptide of syntaxin 1. These findings led to a unified hypothesis that Munc18-1 binds simultaneously to the closed conformation of syntaxin 1 and its N-terminal peptide, which might act as an anchor point to facilitate the transition from the Munc18-1/syntaxin 1 complex to the Munc18-1/SNARE complex assembly. This transition might be key for membrane fusion and probably universally conserved in all types of intracellular membrane trafficking (Dulubova et al., 2007; Shen et

al., 2007). It seems that the additional binding of Munc18-1 to the closed conformation might be unique to the neuronal system, probably to achieve a tighter control of the membrane fusion reaction.

A severe docking defect was observed in *C. elegans* lacking the munc18-1 homologue unc18, as well as in chromaffin cells of Munc18-1 kncokout mice, but docking was normal in brain synapses of these mice (Voets et al., 2001; Verhage et al., 2000; Weimer et al., 2003). In addition, genetic studies in yeast have suggested that Sec1 functions after SNARE complex assembly (Grote et al., 2000). However, the exact function of SM proteins is still unclear. Given their essential role and absolute requirement in all types of intracellular fusion events, their functions and action mechanisms must be elucidated before we can reach a definitive model of neurotransmitter release.

1.5.3 Complexins

Complexins are small neuronal proteins of 15-16kDa and are tightly associated with the ternary SNARE complex formed by syntaxin, SNAP-25 and synaptobrevin. There are four isoforms of complexins, I-IV. Complexins I and II are soluble whereas complexin III and IV are attached to the membrane through C-terminal farnesylation (Reim et al., 2005). Complexin I and II double knockout in mice leads to a lethal phenotype, which suggests the essential role of complexins in the nervous systems (Reim et al., 2001). Electrophysiology studies of the neurons isolated from the complexin I and II double knockout mice revealed

that removal of complexin I/II selectively impairs the Ca^{2+}-triggered neurotransmission, but shows no effect on the hypertonic sucrose-induced neurotransmitter release, suggesting the involvement of complexins in the Ca^{2+}-triggering step (Reim et al., 2001).

The crystal structure of complexin/SNARE complex revealed that complexin forms a short α-helix and binds antiparallel to the middle toward the C-terminus of the SNARE complex (Chen et al., 2002). The binding site of complexin on the SNARE complex is located in the groove between synaptobrevin from the synaptic vesicle and syntaxin from the presynaptic plasma membrane, which suggests that the binding of complexin might function as a "molecular glue" to stabilize the SNARE complex formation (Chen et al., 2002). Recently, several studies using different systems and methods, including a cell-based fusion assay, an *in vitro* liposome-based fusion assay, *in vivo* electrophysiology studies and *in vitro* fluorescence microscopy studies led to a coherent conclusion that complexin inhibits the premature fusion of synaptic vesicles with the plasma membrane and that Ca^{2+} bound synaptotagmin 1 can displace complexin from the SNARE complex to release its inhibitory effect and lead to the fusion pore formation (Giraudo et al., 2006; Schaub et al., 2006; Tang et al., 2006).

1.5.4 Synaptotagmins

Synaptotagmins constitute a family of proteins involved in membrane trafficking. Synaptotagmins are transmembrane proteins containing two cytoplasmic tandem C_2 domains,

the C_2A and C_2B domain (Perin et al., 1990). The founding member of the synaptotagmin family, synaptotagmin 1, has been suggested by extensive biochemical, structural and physiological studies to be the Ca^{2+} sensor for Ca^{2+}-evoked synaptic vesicle exocytosis (Davletov and Sudhof, 1993; Fernandez-Chacon et al., 2001; Geppert et al., 1994b). More than fifteen isoforms of synaptotagmins have been identified in mammals and they have been suggested to form a hierarchy of Ca^{2+} sensors performing different functions and with different intrinsic Ca^{2+}-binding affinity (Sugita et al., 2002).

Synaptotagmin 1 is localized on the synaptic vesicles via the N-terminal transmembrane region with the two C-terminal C_2 domains in the cytoplasm. The C_2 domain was initially identified in protein kinase C (PKC) and named after its second conserved domain (Perin et al., 1990; Perin et al., 1991). Similar to the C_2 domain in PKC, both the C_2A and the C_2B domain of synaptotagmin 1 have been shown to be able to bind to Ca^{2+} and interact with negatively charged phospholipid in a Ca^{2+}-dependent manner (Davletov and Sudhof, 1993; Fernandez et al., 2001). Nuclear magnetic resonance (NMR) spectroscopy and X-ray crystallography have revealed the three dimensional structure of both C_2 domains of synaptotagmin 1. The synaptotagmin 1 C_2A domain adopts a β-sandwich structure composed of eight antiparallel β-strands (Sutton et al., 1995; Shao et al., 1998). The synaptotagmin 1 C_2B domain adopts a similar β-sandwich core structure with an α-helical insertion between strand 7 and strand 8 as well as a C-terminal additional helix after strand 8 (Fernandez et al., 2001). The Ca^{2+}-binding sites of the C_2A and C_2B domains are formed by highly conserved aspartate and serine residues from two loops on the top of the β-sandwich (Fernandez et al.,

2001; Shao et al., 1996). Ca^{2+} titrations by ^{1}H, ^{15}N HSQC spectra and NMR structures of the synaptotagmin 1 C_2 domains showed that the C_2A domain binds three Ca^{2+} ions whereas the C_2B domain binds two Ca^{2+} ions and that the intrinsic Ca^{2+} binding affinity is very low due to the incomplete coordination of Ca^{2+} ions (Fernandez et al., 2001; Shao et al., 1996). However, the Ca^{2+} affinity of both C_2 domains increases remarkably upon binding to negatively charged phospholipids, which presumably help to complete the Ca^{2+}-coordination (Fernandez et al., 2001; Zhang et al., 1998).

Knockout of synaptotagmin 1 in mice causes a selective abolishment of Ca^{2+}-evoked fast synchronous neurotransmitter release, which supports the notion of synaptotagmin 1 as a Ca^{2+} sensor for this highly regulated process (Geppert et al., 1994b). More convincing evidence came from the remarkable correlation between the Ca^{2+}-evoked neurotransmission and Ca^{2+}-dependent phospholipid binding in the mutagenesis studies of either loss-of-function mutations such as R233Q in the Ca^{2+}-binding loops, polybasic region charge neutralization or gain-of-function mutations such as hydrophobicity enhancement by replacing hydrophobic residues in the Ca^{2+}-binding loops with tryptophans (Fernandez-Chacon et al., 2001; Rhee et al., 2005; Li et al., 2006).

1.5.5 Munc13s

1.5.5.1 The Munc13 family

Invertebrate unc13 and mammalian Munc13s constitute a family of large (ca. 200 kDa), phorbol ester dependent proteins localized at the active zone that act as targets of the diacylglycerol (DAG) second messenger signaling pathway (Maruyama and Brenner, 1991; Brose et al., 1995; Betz et al., 1998; Lackner et al., 1999). Unc13 was initially identified in *C. elegans* from screening for uncoordinated movement mutant phenotypes (Brenner, 1974). Mammals contain five Munc13 genes, Munc13-1, Munc13-2, Munc13-3, Munc13-4 and BAP-3. Munc13-1 and Munc13-3 encode proteins specific to neuron and neuroendocrine cells. Munc13-2 gene encodes a ubiquitously-expressed N-terminal splicing variant, ubMunc13-2, in addition to the brain-specific variant bMunc13-2 (Song et al., 1998; Betz et al., 2001). All the brain-specific Munc13s are specifically enriched at the presynaptic active zone. Munc13-1 plays an important role in the priming of synaptic vesicle exocytosis. Munc13-2 is functionally redundant with Munc13-1 in inhibitory neurons. However, Munc13-2 cannot compensate for loss of Munc13-1 in excitatory neurons even though Munc13-1 can compensate for loss of Munc13-2, indicating their distinct functions (Varoqueaux et al., 2002). Munc13-4 is ubiquitously expressed with predominant expression in lung. Munc13-4 has been shown to regulate cytolytic granules secretion in immunological synapses (Feldmann et al., 2003). Unc13 nulls in *C. elegans* and double knockout of Munc13-1 and the closely related Munc13-2 in mice led to total abrogation of spontaneous, sucrose-induced and Ca^{2+}-triggered release, which likely arises from defects in synaptic vesicle priming, indicating the essential role of unc13/Mun13s in neurotransmission (Richmond et al., 1999; Augustin et al., 1999; Varoqueaux et al., 2002). The abrogation of release observed in unc13 nulls in *C. elegans* can be partially rescued by overexpression of a

constitutively open syntaxin 1 mutant that is unable to interact with Munc18, but not by syntaxin 1 wild type (Dulubova et al., 1999; Richmond et al., 2001). This finding and a report that Munc13-1 binds to syntaxin 1A led to a widespread model whereby Munc13-1 helps to open syntaxin 1A from the closed conformation bound to Munc18, allowing the SNARE complex formation (Betz et al., 1997; Richmond et al., 2001). However, the interaction between Munc13-1 and syntaxin 1A has not been verified in solution.

The major mammalian isoform, Munc13-1, contains one DAG/phorbol ester binding C_1 domain, three C_2 domains (referred to as C_2A, C_2B and C_2C domains, respectively) and a Munc13 homology region, the MUN domain (Brose et al., 1995; Basu et al., 2005). This architecture is largely conserved in the unc13/Munc13 family, but the N-terminal region is variable. Munc13-1 mediates different forms of presynaptic plasticity, presumably through multiple protein-protein and protein-ligand interactions (Rosenmund et al., 2002). The DAG/phorbol ester binding C_1 domain is responsible for DAG/phorbol ester-dependent augmentation of neurotransmission (Rhee et al., 2002). The NMR structure of the Munc13-1 C_1 domain showed that its DAG/phorbol ester binding site is occluded by a conserved tryptophan side chain, indicating that significant conformational changes are required for ligand binding (Shen et al., 2005). The N-terminal C_2A domain of Munc13-1 binds to α-RIMs, which are large Rab3 effectors of the active zone that are also involved in synaptic vesicle priming and different forms of short- and long-term presynaptic plasticity (Betz et al., 2001; Castillo et al., 2002; Wang et al., 2000; Dulubova et al., 2005). Electrophysiological studies showed that a structure-based mutation designed to disrupt the interaction between

RIM2α and Munc13-1 impairs neurotransmitter release at the calyx of Held synapse (Dulubova et al., 2005). Interestingly, the Munc13-1 C_2A domain forms a homodimer in solution (Lu et al., 2006), indicating an additional level of regulation by Munc13-1 homodimer to Munc13-1/RIM heterodimer switch. The sequence conservation of its Ca^{2+}-binding site suggests that the central C_2B domain of Munc13 is capable of Ca^{2+}-binding, and potentially Ca^{2+}-dependent phospholipid-binding. Very little is known about the C-terminal C_2C domain except that it lacks the consensus Ca^{2+}-binding residues. An alternative Ca^{2+}-dependent regulation of Munc13s is mediated by a conserved calmodulin-binding sequence in the front of the C_1 domain, which interacts with calmodulin in a Ca^{2+}-dependent manner. The calmodulin-binding sequence together with the C_2B domain of Munc13-1 contribute to some forms of Ca^{2+}-dependent short-term plasticity (Shin et al., unpublished data).

1.5.5.2 The MUN domain of Munc 13s

Sequence analyses have revealed two regions between the C_2B and C_2C domain, referred to as Munc13 homology domain (MHD) 1 and 2 (Koch et al., 2000). However, efforts in our lab to express rat Munc13-1 fragments encompassing the MHD regions failed to yield properly folded proteins. Computational analysis of the sequence predicts that a longer α-helical fragment covering both MHD domains and extra N- and C-terminal sequences could potentially be an autonomously folded module. Indeed, the construct containing the predicted rat Munc13-1 fragment (859-1531 amino acids) can be expressed in high yield in bacteria. Gel filtration, dynamic light scattering and circular dichroism (CD)

spectroscopy showed that this fragment is monomeric, highly α-helical and autonomously folded, and was referred to as the MUN domain (Basu et al., 2005). It was found that the critical role of unc13/Munc13s in synaptic vesicle priming step of neurotransmission is mediated by the MUN domain. Overexpression of the rat Munc13-1 MUN domain could rescue neurotransmitter release in cultured excitatory and inhibitory hippocampal neurons from Munc13-1 and Munc13-2 double knockout mice (Augustin et al., 1999; Basu et al., 2005). These observations suggested that regulation of the efficiency of neurotransmission by different agents such as Ca^{2+}, DAG and Rab3/GTP during diverse presynaptic plasticity processes may converge on the activity of the MUN domain in synaptic vesicle priming, but the mechanism of action of the MUN domain is still not clear and is currently under active investigation (Basu et al., 2005) (Figure 1.6).

1.5.6 Rab3s

Rab (Ras in the brain) proteins consist of a large family of small membrane associated GTP-binding proteins that are localized to discrete subcellular compartments, regulate intracellular membrane trafficking and contribute to the specificity of intracellular membrane fusion events (Grosshans et al., 2006). More than sixty different types of Rab proteins have now been identified in mammals. Rab proteins are usually anchored to the membrane through posttranslational geranylgeranylation of the two C-terminal cysteines (Johnston et al., 1991). The Rab proteins involved in neurotransmitter release, Rab3s are localized on the synaptic vesicles and consist of four isoforms, Rab3A, Rab3B, Rab3C, and

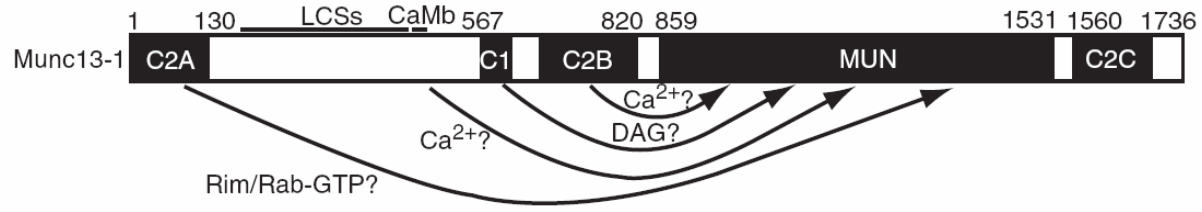

Figure 1.6 Definition of the domain structure of the rat Munc13-1

Domain structure of Munc13-1 resulting from the identification of the MUN domain. Arrows illustrate the proposed ligands of different domains/motifs of Munc13-1 and the notion that the MUN domain activity may be regulated by diverse agents through other sequences of Munc13-1.

Rab3D (Darchen and Goud, 2000).

Rab3s undergo a cycle of synaptic vesicle association and dissociation during synaptic vesicle exocytosis, which is coincident with their activation and inactivation (Fischer et al., 1991). Initially, Rab3s are associated with synaptic vesicles in the active GTP-bound form via their covalently linked geranylgeranyl moieties and interact with the Rab3 effectors. The interaction between Rab3s and their effectors can tether the synaptic vesicles to their appropriate target membrane and facilitate the engagement of v-SNAREs and t-SNAREs, resulting in the docking of the vesicles to the target membrane. Once synaptic vesicle exocytosis is achieved, GTP on Rab3s is hydrolyzed to GDP through catalysis by GTPase activating factors (GAPs) and the resulting inactive GDP-bound Rab3s are dissociated from synaptic vesicles by GDP dissociation inhibitors (GDIs) through the sequestration of the geranylgeranyl moieties of Rab3s (Araki et al., 1990). Besides maintaining the Rabs in the GDP-bound state, GDI also mediate the delivery of the cytosolic GDP-Rab3/GDI complex to the synaptic vesicles. The Rab3s are then released from GDIs and reassociate with synaptic vesicle membranes through GDP/GTP exchange catalyzed by Guanine nucleotide exchange factors (GEFs). The dependence of the GTP hydrolysis and subsequent dissociation from synaptic vesicles of Rab3s on the fulfillment of synaptic vesicle exocytosis suggests the Rab3 cycle might help to ensure directional interactions of Rab3s with their effector proteins during exocytosis.

1.5.7 RIMs

1.5.7.1 The RIM family

Two major types of Rab3 effectors that specifically interact with their GTP-bound state but not their GDP-bound state have been identified, rabphilins and α-RIMs (Shirataki et al., 1993; Li et al., 1994; Wang et al., 1997; Wang et al., 2000; Wang and Sudhof, 2003) . Rabphilin is a cytosolic protein that requires Rab3 for binding to synaptic vesicles and binds to Ca^{2+} via its C-terminal C_2 domains (Geppert et al., 1994a; Li et al., 1994; Ubach et al., 1999). RIMs, in contrast, are large, biochemically insoluble active zone proteins whose C-terminal C_2 domains lack the predicted Ca^{2+}-binding motif (Wang et al., 1997; Wang et al., 2000; Wang and Sudhof, 2003). Both rabphilins and RIMs interact with all four Rab3 isoforms through their N-terminal zinc finger domains.

RIMs are named as Rab3-interacting molecules since they were originally identified as Rab3 effectors. Six mammalian RIM isoforms have been identified, encoded by four genes RIM1, RIM2, RIM3γ and RIM4γ (Wang et al., 1997; Wang and Sudhof, 2003). The RIM1 gene encodes one of the longest RIM isoforms, RIM1α, which contains an N-terminal zinc finger domain, a central PDZ domain and two C-terminal C_2 domains (called the C_2A domain and the C_2B domain) (Figure 1.7). The RIM2 gene encodes three different isoforms, which results from the differential usage of transcriptional initiation sites. RIM2α, shares similar domain architecture with the RIM1α protein and contains one zinc finger, one PDZ and two C_2 domains. RIM2β is an isoform lacking the N-terminal zinc finger domain whereas RIM2γ only contains the C-terminal C_2B domain and adjacent sequences. As their

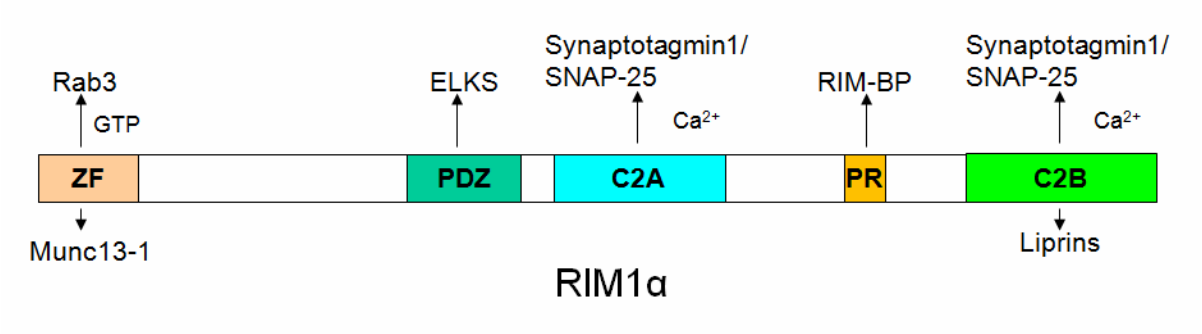

Figure 1.7 The domain structure of mammalian RIM1α

The mammalian RIM1α domains as well as their reported interacting molecules are illustrated.

names indicate, both RIM3γ and RIM4γ contain only the C_2B domain, similar to RIM2γ (Wang et al., 2000; Wang and Sudhof, 2003). In contrast, *C. elegans* possesses only a single RIM isoform, encoded by the unc10 gene (Brenner, 1974; Koushika et al., 2001).

RIMs have been suggested by extensive genetic and electrophysiological experiments to be essential for the synaptic vesicle priming as well as the modulation of both short-term and long-term synaptic plasticity. Knockout of the single RIM isoform encoded by unc10 in *C. elegans* and of RIM1α in mice resulted in impairment of neurotransmission without altering the synapse structure and morphology (Koushika et al., 2001). In *C. elegans*, deletion of unc10 caused a severe reduction of the primed synaptic vesicle population and a consequent reduction of synaptic transmission. In mice, deletion of RIM1α caused a significant decrease of the neurotransmitter release probability in response to Ca^{2+} influx and thus a consequent decrease in synaptic transmission. Moreover, RIM1α knockout mice also exhibit impairment and alteration of several forms of short-term synaptic plasticity and abolishment of a form of long-term synaptic plasticity known as mossy fiber long-term potentiation (LTP) (Schoch et al., 2002; Castillo et al., 2002; Calakos et al., 2004). These defects in synaptic transmission and plasticity lead to the phenotypic defects in learning and memory observed for the RIM1α knockout mice (Powell et al., 2004).

1.5.7.2 The different domains of RIMs

RIMs are large multiple-domain proteins, especially the α-RIM isoforms. It was

reported that their different domains can interact with many other proteins in a highly regulated fashion (Schoch et al., 2002). RIMs are localized at the presynaptic active zone, where most of their binding partners exist. Many of the binding partners of RIMs themselves are also multiple-domain proteins mediating various protein-protein interactions. Thus, in this way a complex protein-protein interaction network can be formed. These observations have lead to the proposed role of RIMs in organizing active zones and forming a protein scaffold for regulating neurotransmitter release at the active zone (Figure 1.7). The N-terminal zinc finger domain of RIMs has been found to interact with the small GTPase Rab3 as well as the C_2A domain of Munc13-1 to form either RIM/Rab3, RIM/Munc13 binary complex or RIM/Munc13/Rab3 tripartite complex (Betz et al., 2001; Wang et al., 2001; Dulubova et al., 2005). The tripartite complex formation potentially bridges Rab3 on the synaptic vesicles and Munc13s at the active zone into close proximity and facilitates their functional coupling (Dulubova et al., 2005). The central PDZ domain of RIMs binds to the C-terminal tail of ELKS with a unique high specificity (Wang et al., 2002; Lu et al., 2005). Together with the interaction between ELKS and other large active zone proteins, such as piccolo and bassoon, they form the cytoskeletal matrix at the active zone (Takao-Rikitsu et al., 2004). GST pulldown experiments have suggested that the RIM C_2A domain interacts with synaptotagmin 1 and SNAP-25 and the interactions are modulated in a Ca^{2+}-dependent manner (Coppola et al., 2001). The RIM C_2B domain has also been reported to interact with synaptotagmin 1 and SNAP-25 as well as liprins (Coppola et al., 2001; Schoch et al., 2002). These observations implicated an intimate connection between RIMs and the two key central players of neurotransmission, the central fusion machinery and the Ca^{2+} sensor. Additionally,

a proline-rich motif between the C_2A and the C_2B domain was found to interact with the SH3 domain of RIM-binding proteins (RIM-BPs), which also interact with voltage-gated Ca^{2+} channels (Hibino et al., 2002).

Unlike the C_2 domains of synaptotagmins, neither the C_2A domain nor the C_2B domain of RIMs harbor the consensus Ca^{2+}-binding motifs formed by the three top loops (Wang and Sudhof, 2003). Yet at the same time, both C_2 domains are functionally important. In *C. elegans*, removal of the C_2A domain of unc-10 caused the mislocalization of the RIM protein (Deken et al., 2005). Moreover, a single point mutation, R844H, in the human RIM1α C_2A domain has been shown to segregate with a severe visual disease called autosomal dominant cone-rod dystrophy (CORD7) (Hunt et al., 2002; Johnson et al., 2003). In *C. elegans*, construct lacking the C_2B domain could not rescue the unc10 null phenotype that can be efficiently restored by the introduction of full length unc10 construct (Koushika et al., 2001). Together with the fact that all six vertebrate RIM isoforms contain the C_2B domain with a high level of evolutionary sequence conservation, this suggested the critical role of the RIM C_2B domain (Wang and Sudhof, 2003).

The fact that neither C_2 domain of RIMs contains the consensus Ca^{2+}-binding motifs raises the interesting question of how they regulate Ca^{2+}-triggered neurotransmitter release at the active zone. Previous studies from our lab have shown that the RIM C_2A domain is indeed unable to bind Ca^{2+} and phospholipids, which is consistent with its lack of the consensus Ca^{2+}-binding motif (Dai et al., 2005). Moreover, no interaction between the RIM

C_2A domain and synaptotagmin 1 or SNAP-25 can be detected by ^{1}H-^{15}N HSQC NMR experiments (Dai et al., 2005). Instead, the crystal structure of the RIM C_2A domain revealed a strikingly dipolar electrostatic charge distribution as well as a potential target-binding site on the bottom 3_{10} helix, where a CORD7-related arginine-to-histidine mutation is located (Dai et al., 2005). However, the structure mechanism of action of the RIM C_2B domain in neurotransmission still needs to be elucidated.

Chapter 2 Structural Characterization of the Munc13 MUN Domain

2.1 Introduction

Neurotransmitter release is an exquisitely regulated process that involves synaptic vesicle docking at presynaptic active zones, a priming reaction that leaves the vesicles ready for release, and Ca^{2+}-evoked exocytosis (Jahn and Sudhof, 1999; Rizo et al., 2006). Many proteins are involved in this process, including the SNAREs, the Sec1/Munc18-1 homologs, and neuron specific proteins such as Munc13s, RIMs, *etc.* (Sudhof, 2004). The central fusion machinery includes the SNARE proteins, synaptobrevin, syntaxin-1 and SNAP-25, and likely Munc18-1 (Jahn and Scheller, 2006). The SNAREs form a highly stable four-helix bundle called the 'SNARE complex' (Sutton et al., 1998). It has been proposed that the formation of the core complex could overcome the repulsion between the two fusion membranes, bring them into close proximity, facilitating or executing fusion. Isolated neuronal syntaxin 1A forms a closed conformation through fold-back of the N-terminal three-helix bundle onto its SNARE motif, which binds Munc18-1 and is different from the open conformation of syntaxin 1A in the core complex (Dulubova et al., 1999). Therefore, syntaxin 1A must undergo a significant conformational change to switch between its complex with Munc18-1 and the core complex (Dulubova et al., 1999). Munc13 has been suggested to be one of the best candidates to facilitate this switch, based on the evidences that the introduction of the open-conformation syntaxin 1A LE mutant can rescue neurotransmitter release in Munc13 knock out *C. elegans* as well as that Munc13 interacts with syntaxin 1A in the GST pulldown

assay (Richmond et al., 2001).

Munc13s are active zone proteins that are essential for synaptic vesicle priming and mediate augmentation of neurotransmitter release by phorbol esters and diacylglycerol (DAG) (Betz et al., 1998). There are three Munc13 isoforms in mammalian brains. The most abundant isoform, Munc13-1, is specifically targeted to presynaptic active zones. Double knockout of Munc13-1 and Munc13-2 completely abolishes both spontaneous and evoked transmitter release (Varoqueaux et al., 2002). Munc13-1 is composed of an N-terminal C_2 domain (referred to as the C_2A domain), a C_1 domain, a central C_2 domain (referred to as the C_2B domain), a Munc13 homology region (referred to as the MUN domain) and a C-terminal C_2 domain (referred to as the C_2C domain) (Figure 2.1). The MUN domain constitutes a minimal domain responsible for Munc13 activity. The MUN domain can rescue efficiently the neurotransmitter release in the Munc13-1/2 double knockout neurons. 30% to 50% of neurotransmitter release is restored upon overexpression of the Munc13-1 MUN domain in the Munc13-1/2 double knockout neurons (Basu et al., 2005). In spite of the critical role of the Munc13 MUN domain, little is known about its three dimensional structure or the mechanism of its function in neurotransmitter release. In this chapter, I mainly focused on the structural characterization of the rat Munc13-1 MUN domain.

2.2 Materials and methods

2.2.1 Recombinant protein DNA construct preparation

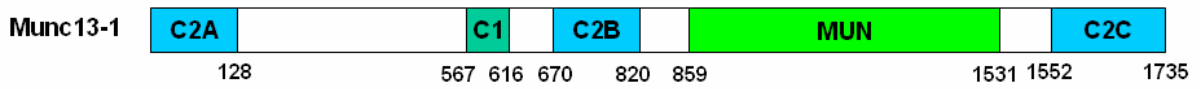

Figure 2.1 The domain structure of the rat Munc13-1

The schematic diagram of the domain structure of the rat Munc13-1 with domain boundaries marked.

DNA encoding glutathione-S-transferase (GST) fusion protein of rat Munc13-1 MUN domain (amino acids 859-1531) subcloned into the pGEX-KG expression vector was generated by a previous graduate student from our lab Nan Shen. DNA encoding GST fusion proteins of rat Munc13-1 C_{12}MUN construct (amino acids 529-1531, which contain the C_1 domain, the C_2B domain and the MUN domain) subcloned into the pGEX-KG expression vector was generated by a previous postdoc from our lab Oleg Guryev. DNA encoding GST fusion protein of rat Munc13-1 MUNC_2C region (amino acids 859-1735, which include the MUN domain and C_2C domain), rat Munc13-2 MUN domain constructs (amino acids 745-1443, amino acids 760-1443, amino acids 783-1423, amino acids 792-1391), rat Munc13-3 MUN domain (amino acids 1380-2024) and human Munc13-4 MUN domain (amino acids 283-906) were generated with standard PCR cloning techniques using synthetic oligonucleotide primers with designed restriction enzyme cleavage sites and ligated into the pGEX-KG expression vector after restriction enzyme digestion. DNA encoding His-tagged protein of the rat Munc13-3 MUN domain was subcloned into pET-28a vector from pGEX-KG expression vector. A construct encoding DNA encoding GST fusion protein of rat Munc13-1 MUN domain with a tobacco etch virus (TEV) protease cleavage site between GST and MUN domain was subcloned into pGEX-KG-TEV vector derived from pGEX-KG expression vector. This construct is referred to as TEV-MUN.

The rat Munc13-1 MUN domain (amino acids 859-1531) F1444Q or F1444A point mutant was generated by the Quickchange® site-directed mutagenesis kit (Stratagene), according to the manufacturer's protocol. Briefly, a pair of complementary oligonucleotide

primers was designed to cover the plasmid region containing the desired mutation with the nucleotide substitutions for mutagenesis. The wild type plasmid was subjected to a PCR thermo cycle using the designed oligonucleotide primers and pfu DNA polymerase. Dpn I treatment of the PCR product was used to selectively digest the parental wild-type plasmid template, which is derived from bacteria and thus hemi-methylated or methylated, whereas leaving the newly synthesized plasmid with desired mutation intact. The digestion product was transformed into high-efficiency supercompetent cells *Escherichia coli* XL1-Blue to ligate the nicks and amplify the mutated plasmids, followed by purification with Qiagen plasmid miniprep kit. The desired mutations were selected and confirmed by DNA sequencing. In some case, the mutation creates or destroys specific restriction enzyme cleavage sites so that the correct colony containing the desired mutations can be screened by restriction enzyme digestion.

Similarly, site-directed mutagenesis was also used to insert a TEV cleavage site (ENLYFQG) at the F1444 position of the construct TEV-MUN (referred to as TEV-MUN-TEV) or make various loop-shortening deletions around the F1444 position in the construct TEV-MUN (deletion of five amino acid 1440-1444, referred to as d5aa; deletion of ten amino acid 1440-1449, referred to as d10aa; deletion of nineteen amino acid 1440-1458, referred to as d19aa).

2.2.2 Expression of recombinant proteins

Plasmids derived from pGEX-KG expression vector with tac promoters were

transformed into *Escherichia coli* BL21 competent cells for GST-tagged protein expression and spread on a luria broth (LB) plate containing ampicillin.

Plasmids derived from pET-28 expression vector with T7 promoters were transformed into *Escherichia coli* BL21 (DE3) competent cells, which contain a DE3 lysogen encoding T7 RNA polymerase, for His-tagged protein expression. The transformed competent cells with pET-28 expression vector were spread on a luria broth (LB) plate containing kanamycin.

For a routine 1 liter bacteria culture, 50ml LB media was inoculated with a single colony and incubated in the shaker at 250 rpm (revolutions per minute) over night at 37ºC. All the media was added with proper antibiotics (ampicillin with a final concentration of 100 μg/ml or kanamycin with a final concentration of 50 μg/ml, depend on the antibiotic resistance of the plasmids) in order to maintain the presence of the transformed plasmids. The next day, the OD_{600} of the overnight culture was measured and diluted accordingly into 1 liter LB media to achieve a starting OD_{600} of about 0.1. The 1 liter cultures were incubated in the shaker at 37ºC and shaken at 250 rpm until the OD_{600} reached 0.6-0.8, which corresponds to the logarithmic growth phase of bacteria. Then, the incubation temperature was decreased to 16 ºC and 1 mM isopropyl β-D-thiogalactopyranoside (IPTG, from Sigma) was added to 1 liter culture to induce the protein expression for overnight (about 16 hours). The bacteria were harvested by centrifugation at 4,000 rpm for 20 minutes at 4°C in swing buckets with a rotor JS 4.2 (Model J6-MI centrifuge, Beckman

Instruments). The supernatant was discarded and the cell pellet was resuspended into 30 ml suspension buffer. For GST-tagged recombinant protein, the suspension buffer is phosphate buffered saline buffer (PBS, 10 mM phosphate, pH 7.4, 2.7 mM KCl, and 137 mM NaCl) containing 10 µl/ml sigma inhibitor cocktail (containing AEBSF, E-64, bestatin, leupeptin, aprotinin, and EDTA, from Sigma), 0.5 mM ABESF (water soluble substitution of PMSF, from RPI Corp.), 2 mM EDTA, 5 mM EGTA, and 5 mM DTT. For His-tagged protein, the suspension buffer is 20 mM Tris, pH8.0, 150 mM NaCl, 0.5 mM AEBSF. The harvested cell suspension was flash-frozen with liquid nitrogen and stored at -80 ºC for further protein purification.

2.2.3 Purification of recombinant proteins

The frozen cell suspensions were thawed in water bath and disrupted by passing twice through a high-pressure French press cell extruder at ~5,000 psi (Model EmulsiFlex-C5, Avestin Inc.). The cell lysate was clarified by centrifugation at 18,000 rpm for 30 minutes at 4°C in a JA-20 rotor with the Beckman centrifuge (model J2-21). The clarified supernatant was taken for purification following different procedures according to their affinity tags.

For GST-tagged recombinant protein, the clarified cell lysate was mixed with 1.33 ml 75% slurry of the pre-washed glutathione Sepharose 4B resins (GE healthcare life sciences) per liter of culture and was rotated in the cold room overnight at 4 °C. The next morning, the mixture was loaded into a gravity column to drain the unbound materials. The glutathione

resins selectively interact with the GST moiety of the GST fusion proteins, whereas leaving non-GST-tagged proteins unbound. The non-specifically bound proteins were removed by a series of washes with 25 ml PBS, 25 ml PBS containing 1% Triton X-100, 25 ml PBS containing 1 M NaCl, and 25 ml PBS. Afterwards, the GST fusion protein-bound resins were washed twice with 5ml benzonase cleavage buffer (50 mM Tris, pH 8.0, 2 mM $MgCl_2$) with freshly added 1 mM DTT. Benzonase nuclease was added to the resins at 0.25 units/µl concentration and rotated at room temperature for one hour, followed by extensively washing with PBS containing 1 M NaCl and PBS, to remove non-specifically bound nucleic acids. The resin was then washed twice with 5 bed volumes of thrombin cleavage buffer (50 mM Tris, pH 8.0, 200 mM NaCl and 2.5 mM $CaCl_2$) with freshly added 1 mM DTT. Then 5-7 units/ml thrombin (from bovine plasma, Sigma) was added to the resin with 7 ml thrombin cleavage buffer, and incubated for one hour at room temperature to remove the GST tag and release the recombinant proteins. The proteins were eluted with elution buffers (10 mM Tris, pH8.5, 250 mM NaCl, 1 mM DTT). 10 µl/ml sigma inhibitor cocktail, 0.5 mM ABESF and 5 mM DTT were added into the recombinant protein immediately after elution.

For His-tagged recombinant proteins, the clarified cell lysate was mixed with 1.33 ml 75% slurry of the pre-washed/equilibrated nickel-nitrilotriacetic acid (Ni-NTA) agarose resins (QIAGEN) per liter of culture and was rotated in the cold room for 2 hours at 4 °C. The mixture was loaded into a gravity column to drain the unbound materials. The Ni-NTA resins selectively interact with the hexahistidine-tagged proteins, whereas leaving non-tagged proteins unbound. The non-specifically bound proteins were removed by a series of washes

with 25 ml buffer (20 mM Tris, pH 8.0, 150 mM NaCl, 0.5 mM AEBSF), 25 ml buffer (20 mM Tris, pH 8.0, 1% Triton X-100, 0.5 mM AEBSF), 25 ml buffer (20 mM Tris, pH 8.0, 1M NaCl, 0.5 mM AEBSF), and 25 ml buffer (20 mM Tris +1 M NaCl + 0.5 mM AEBSF). Afterwards, the resins were washed twice with 5 bed volumes of thrombin cleavage buffer (50 mM Tris, pH 8.0, 200 mM NaCl and 2.5 mM $CaCl_2$). Then 5-7 units/ml thrombin (from bovine plasma, Sigma) was added to the resin with 7ml thrombin cleavage buffer, and incubated for one hour at room temperature to remove the N-terminal His tag and release the recombinant proteins with N-terminal extra linker residues from the construct. The proteins were eluted with elution buffer (10 mM Tris, pH8.5, 250 mM NaCl). 10 μl/ml sigma inhibitor cocktail, 0.5 mM ABESF and 5 mM DTT were added into the recombinant protein immediately after elution.

The protein eluted from resin was diluted to 5 fold volumes in order to obtain low ionic strength. Then the diluted protein was purified by anion exchange chromatography through a mono Q 5/50GL column (GE healthcare life sciences). The mono Q column was equilibrated with the low salt QA buffer [20 mM Tris, pH 8.0, 0.5 mM Tris(2-carboxyethyl) phosphine (TCEP)]. Protein was eluted with a linear gradient of the high salt QB buffer (20 mM Tris, pH 8.0, 1 M NaCl, 0.5 mM TCEP). The protein was eluted between 120 to 150 mM NaCl concentrations. The peak fraction was checked by SDS-PAGE and Coomassie blue staining. The peak corresponding to the Munc13-1 MUN domain was collected and further purified by gel filtration chromatography through a Superdex 200 Hiload 16/60 column (GE healthcare life sciences), which was equilibrated with the gel filtration buffer

(10mM Tris, pH8.5, 250mM NaCl, 0.5mM TCEP).

The purity of the protein purified by both the anion exchange chromatography and the gel filtration chromatography was assessed by SDS-PAGE and Coomassie blue staining. The purified protein was concentrated to 6mg/ml for crystallization using an Amicon Ultra centrifugal filter concentrator of 30 kDa molecular weight cutoff with low-binding Ultracel membranes (Millipore corporation).

UV-light absorption at 280nm was used for protein concentration measurements. Normally, the typical yield of purified protein was 4 to 6 mg per liter of culture after two-step FPLC purifications.

2.2.4 Dynamic light scattering (DLS) analysis of rat Munc13-1 MUN domain

Dynamic light scattering (DLS) analysis was performed on a DynaPro dynamic light scattering model 99D instrument equipped with a temperature controlled microsampler (Wyatt Technology) using 20 second acquisition time at 20 °C. The purified rat Munc13-1 MUN domain or rat Munc13-1 C_{12}MUN fragment was centrifuged at 13,000 rpm for 15 min in a microcentrifuge (Fisher Scientific) before DLS data acquisition. 20µl Munc13-1 MUN domain at the concentration of 1 mg/ml and 7 mg/ml as well as Munc13-1 C_{12}MUN fragment at the concentration of 2 mg/ml were analyzed by DLS. The results were then processed with the program Dynamics V6 (Wyatt Technology). The radii and the size distribution were

calculated with the regularization algorithm provided by Dynamics V6.

2.2.5 Crystallization of the Munc13 MUN domain

The rat Munc13-1 MUN domain dissolved in 10 mM Tris, pH 8.5, 250 mM NaCl and 10 mM TCEP was concentrated to 6 mg/ml and set up for crystallization screening. All the crystallization screening was performed using the hanging-drop vapor diffusion method at 20 °C and 4 °C. For the crystallization buffer, we used standard, commercially available crystallization solution kits (Hampton Research, Emerald BioStructures, Qiagen Protein Technologies), as well as home-made screen kits. For a typical 48-well plate, 200µl of crystallization solutions were first added to each well. 1µl of rat Munc13-1 MUN domain (or any other protein of interest) and 1µl of the crystallization solution from the bottom well were then mixed on a clean, silliconized coverslip. The drop-containing coverslip was inversely pressed onto the pre-greased well to seal the chamber. The protein/precipitant mixture drop is allowed to equilibrate in this sealed system against a much larger reservoir of the same precipitants. Because the precipitant concentration in the reservoir is higher than that in the hanging drop, water evaporates from the drop and causes a gradual increase of the protein concentration in the hanging drop, which potentially can lead to the formation of protein crystals in certain precipitant conditions.

Crystallization drops were monitored regularly under a light microscope equipped with a polarizer. For the first week after set up, observations were made once a day. In the

remaining time of the first month, observations were made once a week. After a month, observations were made once a month until the protein drop and the crystallization solutions dried out.

The rat Munc13-1 MUN domain was crystallized in 15% saturated potassium phosphate, 0.1 M sodium citrate pH 5.6, at 20 °C. This condition was repeated and also expanded for optimization by varying the pH and precipitant concentration to obtain crystals suitable for X-ray data collection. Small crystals appeared in 10 days and grew to a final size of 50 μm × 50 μm × 100 μm in one month. Prior to data collection, crystals were transferred into a solution containing 20% (v/v) ethylene glycol as cryoprotectant and flash cooled in liquid propane, then stored in liquid nitrogen until data collection. The type and optimal amount of cryoprotectant used were chosen by testing different cryoprotection solutions at different concentrations in the cryostream at 100K to ensure the lack of crystalline ice formation.

2.2.6 X-ray crystallographic data collection

The diffraction data were collected and processed with the help of Dr. Diana Tomchick in the Structural Biology Laboratory. The initial diffraction data of the rat Munc13-1 MUN domain crystals were collected at 100K using an Raxis IV imaging plate system (Molecular Structure Corporation, Houston, TX, USA) mounted on a Rigaku RU-200 rotating anode X ray generator (CuKα, wavelength 1.54Å) (Rigaku Corporation, Japan)

operated at 100 mA and 50 kV. The crystals only diffracted to a Bragg spacing (d_{min}) of ~6.5 Å. Subsequently, more diffraction data were collected at the Structural Biology Center (SBC) beamlines 19BM and 19ID of the Advanced Photon Source (APS) at 100 K. Unfortunately, the diffraction of the rat Munc13-1 MUN domain crystals didn't improve much at the synchrotron, as the crystal only diffracted to a Bragg spacing (d_{min}) of ~7 Å.

2.3 Results

2.3.1 The crystallization of the rat Munc13-1 MUN domain

The MUN domain of Munc13-1 is about 74 kD, containing 673 amino acid residues. Its large molecular weight makes it very difficult for us to determine its three-dimensional structure using NMR methods. Moreover, the ^{1}H-^{15}N HSQC spectrum of the Munc13-1 MUN domain shows that most of the amide cross-peaks are clustered at the center of the spectrum, which makes it more difficult to resolve the cross-peaks and determine the structure. Therefore, X-ray crystallography was mainly used for the determination of the Munc13-1 MUN structure. The results of purification and crystallization of various attempted constructs of Munc13-1 MUN domain are summarized in Table 2. 1.

Initially, I worked mainly on two constructs: construct encompassing the MUN domain and construct containing the MUN domain plus the C_2C domain, which is referred to as MUNC_2C in my study. The reason that I also worked on MUNC_2C is that studies from

Table 2.1 Summary of the purification and crystallization of Munc13 MUN domain

species	Constructs	purification	crystallization
Rat Munc13-1	$MUNC_2C$	Soluble, high yield	No hits
	MUN	Soluble, high yield	Crystal diffracted to 6-7 Å
	MUN(F1444A)	Soluble, high yield	Tiny crystal from oily drop
	MUN(F1444Q)	Soluble, high yield	Tiny crystal from oily drop
	TEV-MUN	Soluble, high yield	Similar crystal as wild-type
	TEV-MUN-TEV	Soluble, high yield	Tiny crystal, but not reproducible
	MUN(d5aa)	Soluble, high yield	No hits, only salt crystals
	MUN(d10aa)	Soluble, high yield	No hits
	MUN(d19aa)	Soluble, low yield	N/A
	$C_{12}MUN$	Soluble, low yield	Crystal diffracted to 7.5 Å
Rat Munc13-2	Munc13-2 (745-1443aa)	Stick on the resin, aggregation	N/A
	Munc13-2 (760-1443aa)	Stick on the resin, aggregation	N/A
	Munc13-2 (783-1423aa)	Stick on the resin, aggregation	N/A
	Munc13-2 (792-1391aa)	Stick on the resin, aggregation	N/A
Rat Munc13-3	GST-Munc13-3 (1380-2024aa)	Soluble, cannot be cleaved by thrombin	N/A
	His-Munc13-3 (1380-2024aa)	Soluble, high yield	crystal, but not reproducible
Human Munc13-4	GST-Munc13-4 (283-906aa)	insoluble	N/A

Nile Brose's group have suggested that the C-terminal C_2C domain is also involved in Munc13-syntaxin 1A interaction (Stevens et al., 2005). Both MUN and $MUNC_2C$ could be expressed and purified in high yield from bacteria. Approximately 4-6 mg soluble MUN or $MUNC_2C$ could be obtained from 1 L *E. coli* culture after ion exchange chromatographic and gel filtration chromatographic purification. Both proteins run larger than their nominal molecular weight on a gel filtration column, presumably because of their elongated shapes. Dynamic light scattering analyses of the purified MUN or $MUNC_2C$ suggested that both proteins are monomeric and monodispersed (Figure 2.2). However, the stability tests at either room temperature or 4 °C revealed that both MUN and $MUNC_2C$ would be hydrolyzed into two distinct fragments in a few days (Figure 2.3). This cleavage seems quite specific and the cleavage site was mapped to the 1444th amino acid phenylalanine of Munc13-1 based on mass spectrometry and N-terminal sequencing results. I will discuss about this specific cleavage later in more details.

Rat Munc13-1 MUN domain or $MUNC_2C$ was exchanged into the buffer of 10 mM Tris, pH 8.5, 250 mM NaCl and 10 mM TCEP and concentrated to 6 mg/ml before crystallization screening. Initial screenings were performed with both standard, commercially available crystallization solution kits (Hampton Research, Emerald BioStructures, Qiagen Protein Technologies) and home-made screen kits at either 20 °C or 4 °C. The first crystals of MUN came out in the condition of 15% saturated potassium phosphate, 0.1 M sodium citrate pH 5.6, at 20 °C after 10 days growth (Figure 2.4). The Munc13-1 MUN domain crystals are about 50 μm × 50 μm × 100 μm and exhibit a trigonal

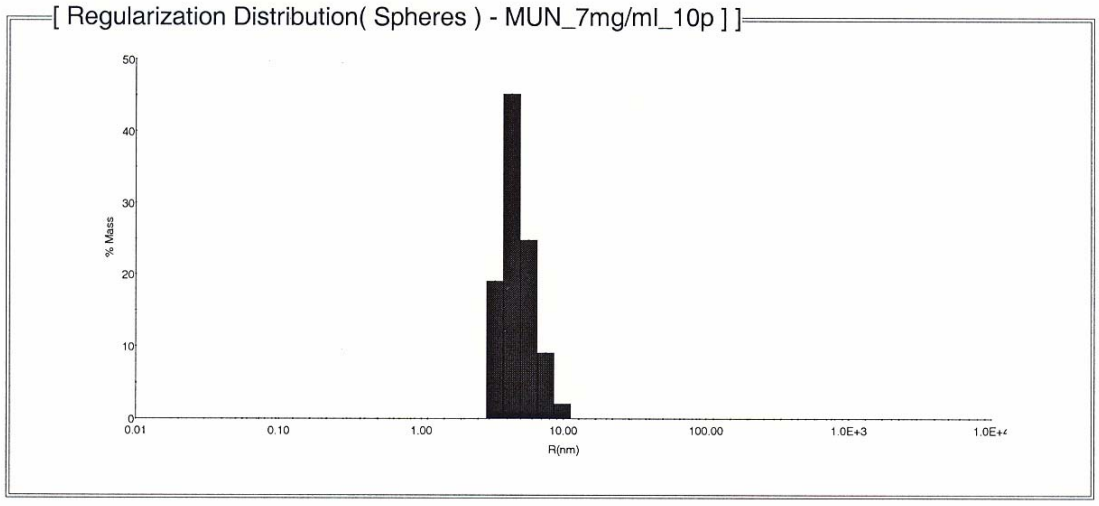

[Results Summary - MUN_7mg/ml_10p]

Item	R	%Pd	MW-R	%Int	%Mass
	(nm)		(kDa)		
Peak 1	0.1	11.6	0	----	----
» Peak 2	4.8	28.0	134	96.1	100.0
» Peak 3	320.3	9.2	2453740	3.9	0.0

Figure 2.2 Dynamic light scattering (DLS) analysis of the Munc13-1 MUN domain

The DLS analysis shows the size distribution of the Munc13-1 MUN domain with radii, polydispersity (Pd) and apparent molecular weights corresponding to globular molecules.

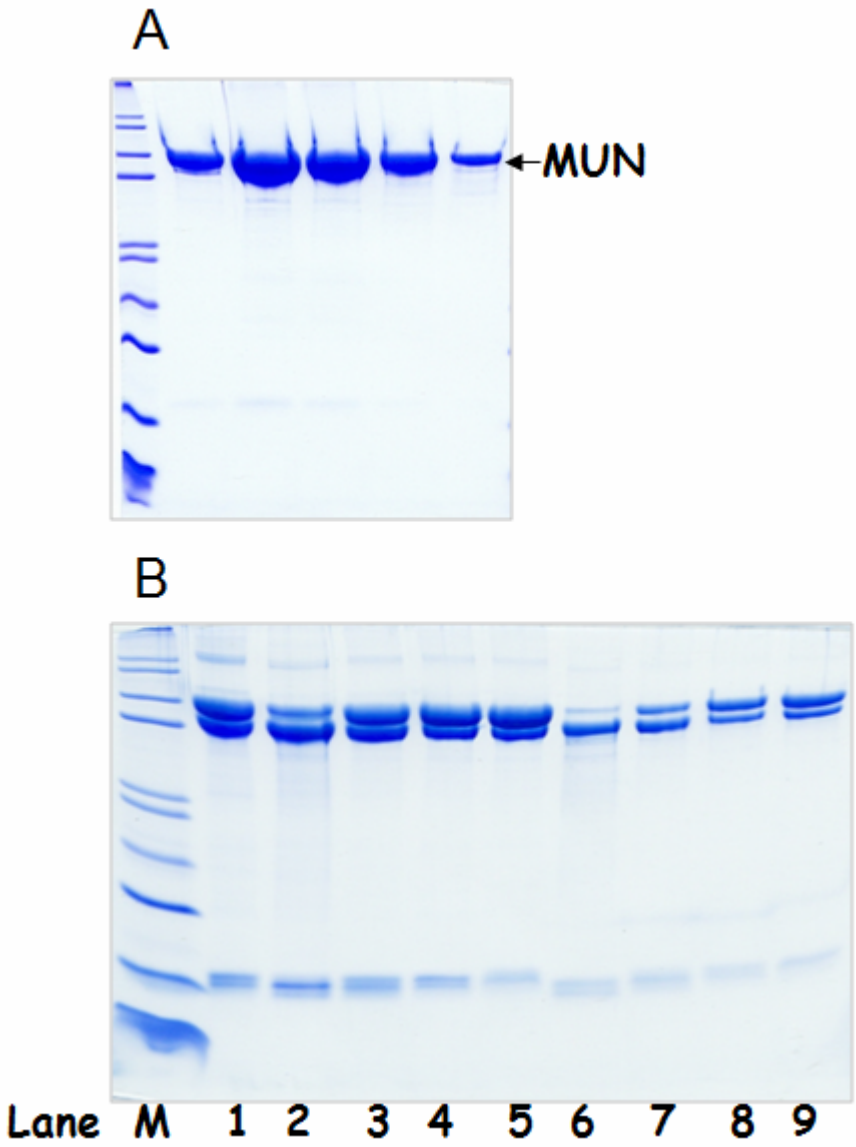
A
MUN
B
Lane M 1 2 3 4 5 6 7 8 9

Figure 2.3 Proteolysis of the Munc13-1 MUN domain

(A) The Munc13-1 MUN domain after Source Q anion exchange and S200 gel filtration chromatographic purification.

(B) Proteolysis of the Munc13-1 MUN domain after 4 days at room temperature. Lane 1-5 contain 1.3 mg/ml MUN domain and lane 6-9 contain 0.38 mg/ml MUN domain. Lane 1 is the sample after only Source Q purification. Lanes 2 and 6 are the samples in pH 8.0 Tris buffer. Lanes 3 and 7 are the samples in pH 8.5 Tris buffer. Lanes 4 and 8 are the samples containing 5% glycerol. Lanes 5 and 9 are the samples containing 0.5% β-OG.

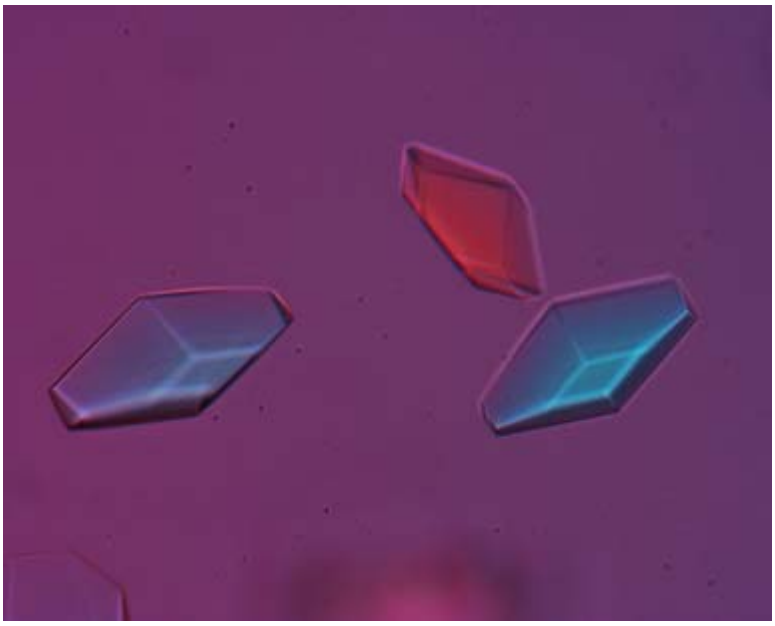

Figure 2.4 Crystals of the rat Munc13-1 MUN domain

Trigonal bipyramidal crystals of the Munc13-1 MUN domain were obtained in 15% saturated potassium phosphate, 0.1 M sodium citrate pH 5.6, at 20 °C with a final size of about 50 μm × 50 μm × 100 μm.

bipyramidal shape. However, these nice-looking crystals only diffract to about 6 to 7Å (Figure 2.5A). Based on the initial hit, I performed the fine-tuning optimization screening for the Munc13-1 MUN domain crystallization condition, with expanded the pH range covering from pH 4.5 to pH 6.6 and expanded the precipitant concentration range covering from 12% to 17%. The fine-tuning screening results suggested that the lower pH could accelerate the growth rate of the Munc13-1 MUN domain crystals. For example, crystals came out in about 7 days with 12% saturated potassium phosphate, 0.1 M sodium citrate pH 5.17, at 20 °C. I also tried the additive screening and various seeding methods to improve the diffraction quality of the crystals. The seeding procedure seems to help increase the size of Munc13-1 MUN domain crystal to 100 μm × 100 μm × 200 μm. A regular lattice pattern was observed in one of the diffraction patterns obtained from the crystal generated by seeding (Figure 2.5B). Unfortunately, all these efforts of extensive optimization failed to improve the diffraction limit. On the other hand, extensive screening failed to yield initial hits for crystallization of $MUNC_2C$.

Wild type Munc13-1 MUN domain failed to yield high quality crystals after comprehensive crystallization screening and optimization. The crystal growth might be hindered by various reasons, for example, inhomogeneity or a lack of tight packing, resulting from flexible loops and termini of the proteins of interest, inhomogeneity caused by proteolysis, etc. Bearing in mind the aforementioned observation of specific proteolysis at F1444 position of the Munc13-1 MUN domain, I made two site-directed mutants at the mapped proteolysis sites to try to get rid of the proteolysis. The phenylalanine at the position

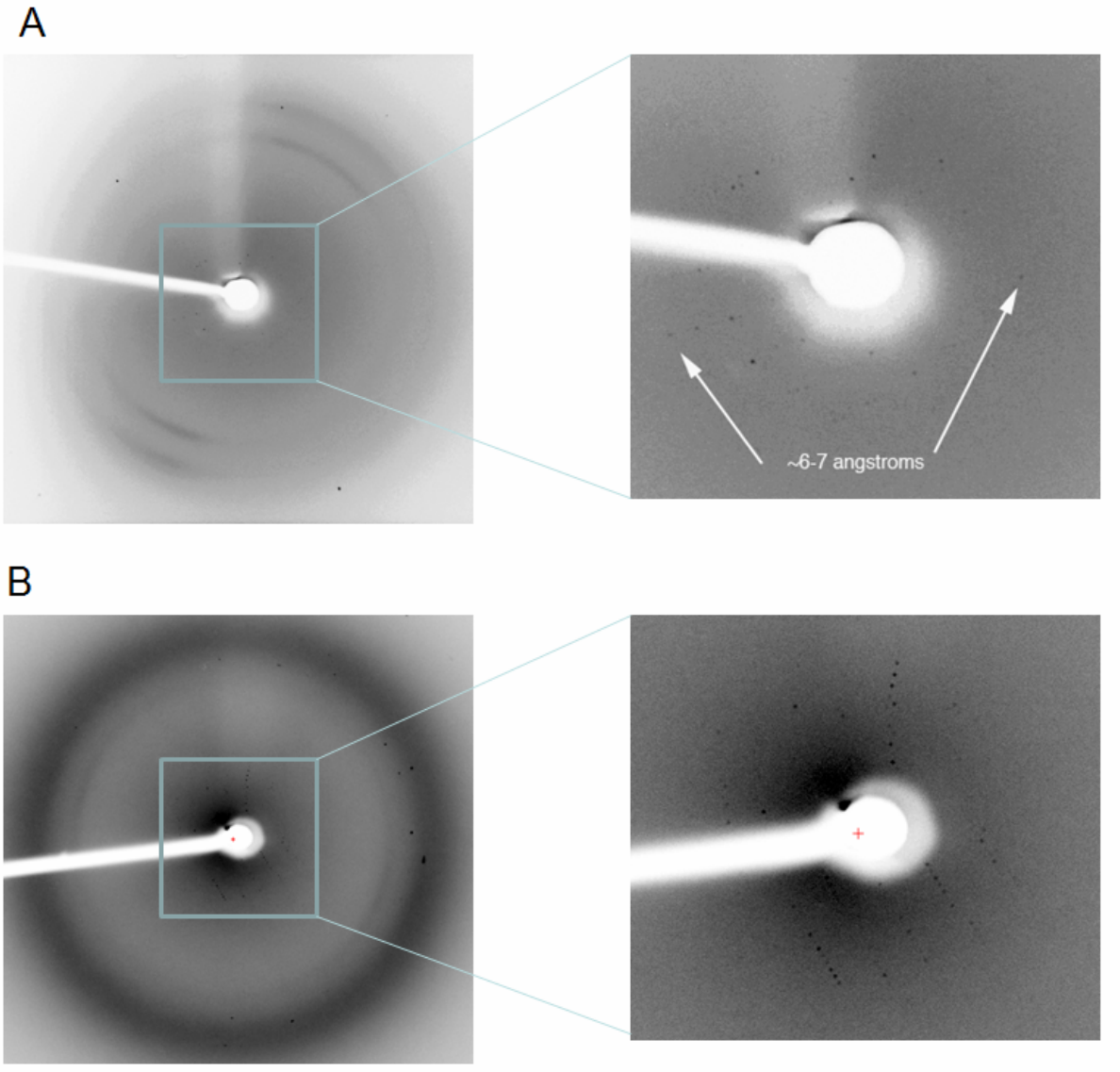

Figure 2.5 The diffraction patterns of the Munc13-1 MUN domain crystals

(A) The diffraction pattern of the initial Munc13-1 MUN domain crystals, which diffract only to about 6 to 7Å

(B) The diffraction pattern of the improved Munc13-1 MUN domain crystals, which shows the presence of regular lattice patterns.

of 1444 was mutated to either alanine or glutamine and the corresponding construct is referred to as MUN(F1444A) and MUN(F1444Q), respectively. These mutants were similarly well expressed as the wild type. However, the stability tests suggested that the two mutations only slow down the proteolysis, but could not completely get rid of the proteolysis problem (Figure 2.6). Interestingly, similar crystals of the mutants were observed under conditions similar to those of wild type with a longer delay of about two months. Moreover, based on the secondary structure prediction, the phenylalanine 1444 is potentially located in a long loop between two α-helices. Therefore, I also tried to alleviate the proteolysis problem by shortening the predicted loop containing the cleavage site. I made several loop-shortened constructs, with 5, 10 or 19 residues deleted within the F1444-containg loop, attempting to reduce the flexibility and protease susceptibility of the loop region to improve the crystals. These constructs were generally more stable compared to the wild type Munc13-1 MUN domain. However, none of the loop-shortened constructs yielded any promising hit in crystallization trials.

Another interesting observation during the fine-tuning screening for the wild type Munc13-1 MUN domain crystallization conditions is that the crystal seems to only contain the cleaved Munc13-1 MUN domain. In order to check the identity and proteolytic state of the proteins inside the crystal, the crystals were looped out from the drop, washed briefly, dissolved in SDS-PAGE loading buffer and subjected to SDS-PAGE and Coomassie blue staining. No full-length MUN domain was observed in the sample prepared from the crystals (Figure 2.7). In contrast, both the crystallization drop devoid of crystals and the proteineous

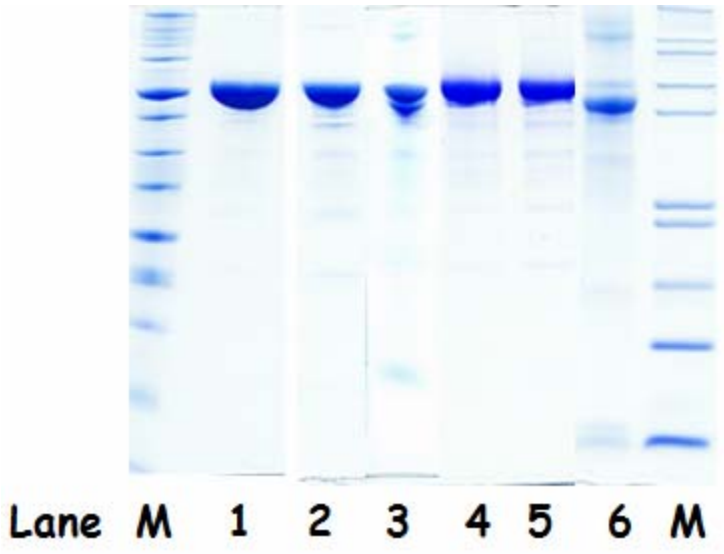

Figure 2.6 Proteolysis of the Munc13-1 MUN domain F1444A and F1444Q mutants

Lane 1-3 contain Munc13-1 MUN domain F1444A mutant and lane 4-6 contain Munc13-1 MUN domain F1444Q mutant. Lane 1 is the freshly purified F1444A mutant. Lanes 2 and 3 are the F1444A mutants after 3 days or 12 days at room temperature. Lane 4 is the freshly purified F1444Q mutant. Lane 5 is the F1444Q mutant after 2 days at 4 °C. Lane 6 is the F1444Q mutant after 30 days at room temperature.

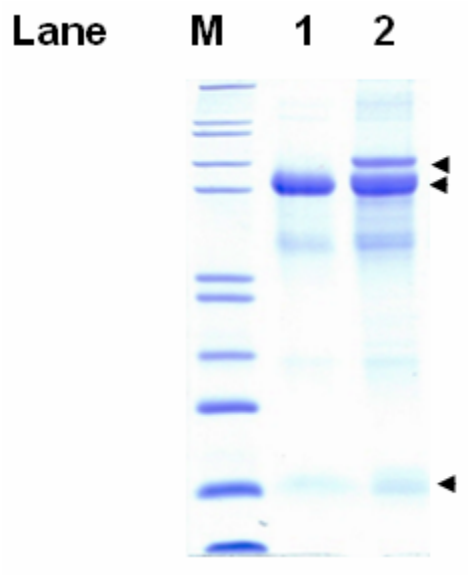

Figure 2.7 The MUN crystal contains only the proteolyzed fragments

Lane 1 is Munc13-1 MUN crystal devoid of drop solution. Lane 2 is the crystallization drop devoid of crystals and the proteineous skin covering the crystallization drop.

skin covering the crystallization drop contained the full-length MUN domains (Figure 2.7). The Munc13-1 MUN domain crystal contains two distinct fragments with molecular weight of 68 kD and 7 kD, which correspond to the aforementioned proteolysis fragments observed in the stability tests. Based on these results, I speculated that the cleavage at phenylalanine 1444 might be necessary for the crystallization of the MUN domain. This observation motivated me to initiate another strategy of construct modification to improve the crystallization through facilitation of proteolytic cleavage. This was achieved by introducing an artificial TEV cleavage site (ENLYFQG) before the phenylalanine 1444 (the corresponding construct is referred to as TEV-MUN-TEV), attempting to promote the proteolysis process via TEV cleavage to facilitate the crystallization process and improve the diffraction quality of the crystals. Interestingly, during the purification through ion-exchange column and gel filtration column, the N-terminal fragment and C-terminal fragment of TEV-MUN-TEV always elute together, suggesting they interact strongly with each other, which is consistent the fact that the crystal contains the complex of the two fragments.

Besides the MUN domain, we also tried to crystallize a longer fragment from Munc13-1, which includes the C_1 domain, C_2B domain as well as the MUN domain and is therefore named C_{12}MUN. We successfully expressed and purified the C_{12}MUN fragment from *E. Coli*. The C_{12}MUN fragment behaves very well even though the yield is not high when expressed in bacteria. The C_{12}MUN fragment runs as a monomer in gel filtration chromatography and is also highly monodispersed as evaluated by the dynamic light scattering analysis (Figure 2.8). The crystals of C_{12}MUN were grown in 0.2 M magnesium

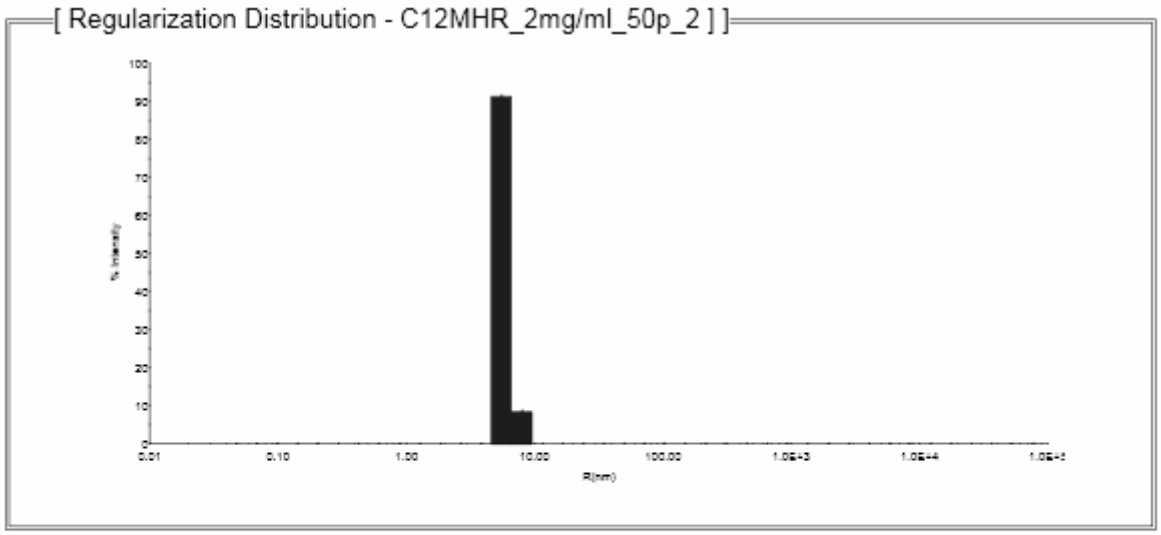

[Results Summary - C12MHR_2mg/ml_50p_2]

Item	R	Pd	%Pd	MW-R
	(nm)	(nm)		(kDa)
Peak 1	0.04732	0	0	0.00267331
» Peak 2	5.74947	0.685575	11.9242	201.63

Figure 2.8 Dynamic light scattering (DLS) analysis of the Munc13-1 C_{12}MUN fragment

The DLS analysis shows the size distribution of the Munc13-1 C_{12}MUN fragment with radii, polydispersity (Pd) and apparent molecular weights corresponding to globular molecules.

formate, but they only diffracted to about 7.5Å at the synchrotron. Preliminary analysis using HKL2000 suite (Otwinowski and Minor, 1997) suggested that the space group was I222 with unit cell parameters a=100Å, b=100Å, c=400Å and that each asymmetric unit (ASU) probably contains two to three molecules, corresponding to 65% and 45% solvent content, respectively (Matthews, 1968). Furthermore, I also obtained crystals of the C_{12}MUN fragment purified from sf9 insect cells in either 0.1 M Tricine, pH 8.0, 12% (w/v) PEG 2000 MME or 0.1 M Tricine, pH 8.0, 15% (v/v) PEG 400 (Figure 2.9). Unfortunately, these crystals failed to diffract to useful resolutions.

2.3.2 The crystallization of the MUN domain of other Munc13 isoforms

Since the construct optimization for crystallization of the Munc13-1 MUN domain hasn't been very successful, I started to try to express and crystallize the MUN domain of its closely related isoforms, Munc13-2 and Munc13-3. The sequence conservation among Munc13-1, Munc13-2, and Munc13-3 is relatively high (Figure 2.10). However, they also exhibit some variations, which might provide some natural tuning of the constructs for crystallization.

Several Munc13-2 MUN domain constructs were made, including Munc13-2 (745-1443aa), Munc13-2 (760-1443aa), Munc13-2 (783-1423aa), and Munc13-2 (792-1391aa). However, none of these constructs behaved very well and all of them have a high tendency to aggregate and result in very bad gel filtration chromatography profiles. Therefore, I

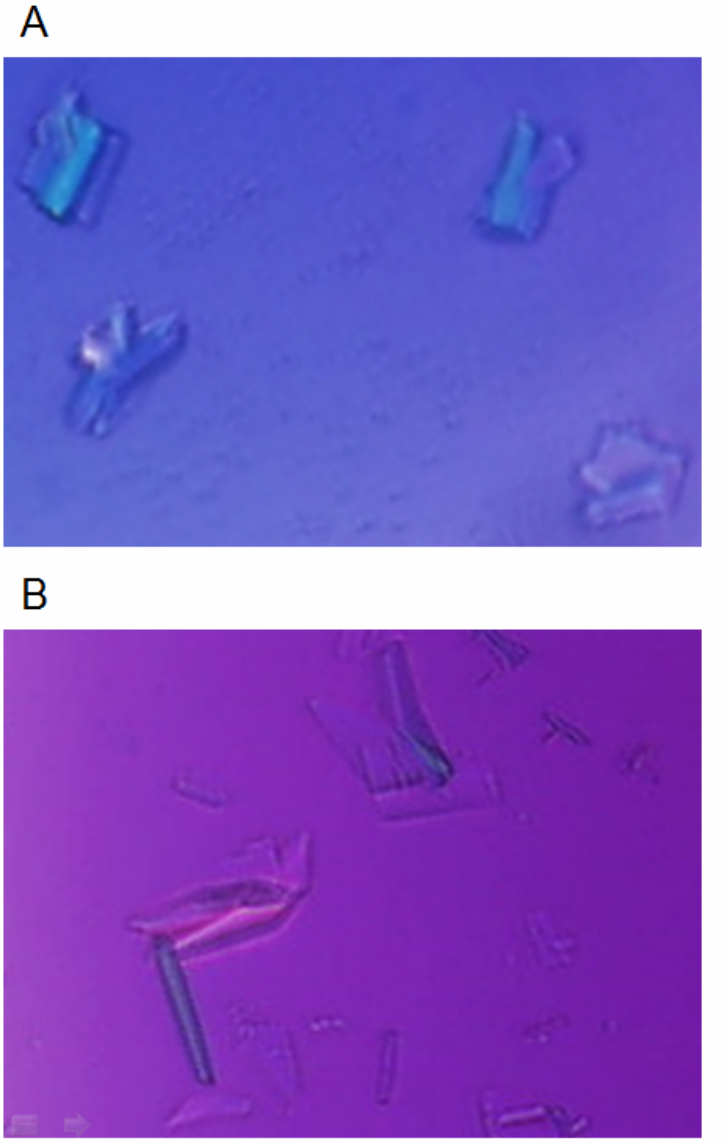

Figure 2.9 Crystals of the Munc13-1 C_{12}MUN fragment

(A) Crystals of the Munc13-1 C_{12}MUN fragment were obtained in 0.1 M Tricine, pH 8.0, 12% (w/v) PEG 2000 MME.

(B) Crystals of the Munc13-1 C_{12}MUN fragment were obtained in 0.1 M Tricine, pH 8.0, 15% (v/v) PEG 400.

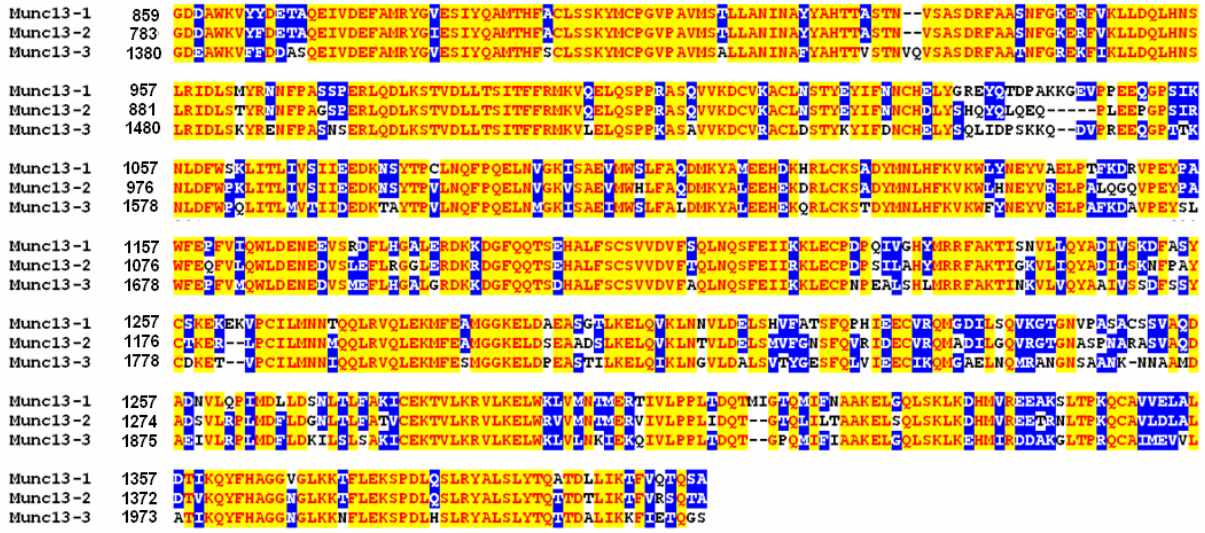

Figure 2.10 Sequence alignment of Munc13-1, 2, 3 isoforms

The identical residues in all three Munc13 isoforms are shown in red with yellow background. The identical residues in only two isoforms or the conservative substitutions among the three isoforms are shown in white with blue background.

continued to make two Munc13-3 constructs, GST-tagged Munc13-3 (1380-2024aa) and His-tagged Munc13-3 (1380-2024aa). The GST-tagged Munc13-3 MUN domain had problems with thrombin cleavage, which might be due to the very short linker between the thrombin cleavage site and the start residue of the Munc13-3 MUN domain. Due to the cleavage problem, we can only obtain the GST fusion protein of the Mun13-3 MUN domain by glutathione elution, which runs as a dimer in gel filtration chromatography. The difficulty of thrombin cleavage indicates that the GST moiety and the Mun13-3 MUN domain might be linked relatively rigidly. Together with the fact that the dimer of GST-Munc13-3 MUN domain has a molecular weight of ~200 kDa and probably an elongated shape, we suspect that the fusion protein might be marginally visible by electron microscopy (EM). Therefore, we decided to perform some preliminary EM imaging of the fusion protein by negative staining, hoping that we could obtain some overall shape information about the Munc13-3 MUN domain. However, the EM images taken were hard to interpret for picking particles unambiguously for analysis. In contrast, the His-tagged Munc13-3 MUN domain was expressed and purified without any problem and the protein behaves very well. Crystals of the Munc13-3 MUN domain purified in this way were grown in 0.5 M ammonia sulfate, 0.1 M HEPES, pH 7.5 and 30% (v/v) MPD in about a week, but could not be consistently reproduced. The results of purification and crystallization of the constructs of Munc13-2 and Munc13-3 are also summarized in Table 2.1.

I also tried to express and crystallize the MUN domain (283-906aa) of another far-related isoform of Munc13-1, Munc13-4, which has been suggested to be involved in the

regulation of the cytolytic granules secretion in the immunological synapse (Feldmann et al., 2003). But unfortunately, this construct failed to yield soluble proteins for crystallization trials (Table 2.1).

2.4 Future plan

The results of crystallizing the Munc13 MUN domain summarized in Table 2.1 indicate that the crystallization of several constructs is worth further optimization. We will focus on the Munc13-1 MUN domain and the Munc13-3 MUN domain expressed in bacteria as well as C12MUN expressed in sf9 insect cells. Once we get good-quality crystals and sufficient data, initial attempts for structure determination of the MUN domain will be performed via molecular replacement. Three-dimensional fold prediction suggests that the MUN domain might have similar structure to that of importin β. Therefore, importin β will be used as a search model in the molecular replacement. If this fails, the structure may be solved via single- or multiple-wavelength anomalous dispersion (SAD/MAD) experiments using the selenomethionyl variant of the protein. In addition, attempts will be made to solve structures via the traditional single isomorphous replacement (SIR) or multiple isomorphous replacement (MIR) method utilizing rapid heavy atom soaking.

Chapter 3 Biochemical Studies of the rat Munc13-1 MUN Domain

3.1 Introduction

As I have mentioned in Chapter 2, the Munc13-1 activity in neurotransmitter release is largely mediated by the MUN domain between the C_2B and C_2C domains (Basu et al., 2005). Multiple protein-protein and protein-ligand interactions such as the RIM/Rab binding of the C_2A domain, the calmodulin binding of its binding motif between C_2A and C_1 domains, the DAG/phorbol ester binding of the C_1 domain, and the Ca^{2+}-binding of the C_2B domain, presumably sense and integrate different signals, which converge on the MUN domain to regulate its activity (Wang et al., 2000; Dulubova et al., 2005; Junge et al., 2004; Rhee et al., 2002; Basu et al., 2005). However, the mechanism of the Munc13 MUN domain function is still poorly understood. In this chapter, I tried to unravel the function of the rat Munc13-1 MUN domain through biochemical and biophysical studies.

3.2 Materials and methods

3.2.1 Recombinant protein DNA construct preparation

DNA encoding His-tagged protein of rat Munc13-1 MUN domain was subcloned in pET-28c vector from pGEX-KG expression vector. Quickchange® site-directed mutagenesis kit (Stratagene) was used to insert single, double or triple T7 tag at the N-terminus of rat

Munc13-1 MUN domain subcloned in pET-28c vector. DNA encoding His-tagged protein of rat Munc18 was subcloned in pET-28a vector from pGEX-KG expression vector. Quickchange® site-directed mutagenesis kit (Stratagene) was used to insert single, double or triple T7 tag at the N-terminus of rat Munc18 subcloned in pET-28a vector.

3.2.2 Size exclusion chromatographic binding assay

Size exclusion chromatographic binding assay was performed with a Superdex S200 10/300 GL column (GE healthcare life sciences) on an ÄKTA FPLC™ protein purification system (GE healthcare life sciences). 500 μL sample was injected into a sample loop of 500 μL volume and eluted with binding assay buffer through the size exclusion column. The final concentrations of the injection samples were usually 5 to 10 μM. The typical binding assay buffer contains 20 mM Tris, pH 8.0, 150 mM NaCl, 1 mM freshly added DTT. Binding reactions were usually incubated for two hours at 4 ºC in the cold room before injection into the FPLC system. The fractions were concentrated by trichloroacetic acid (TCA) precipitation and analyzed by SDS-PAGE and Coomassie blue staining.

3.2.3 ^{15}N-edited and ^{13}C-edited 1D NMR experiments

The first increment of a gradient-enhanced ^{1}H-^{15}N HSQC spectrum or ^{1}H-^{13}C HSQC spectrum was acquired to obtain the 1D ^{15}N-edited or ^{13}C-edited ^{1}H NMR spectra with both ni or ni2 (number of t1 increments in the ^{15}N dimension or the ^{13}C dimension) and phase set

to 1. The 1D ^{15}N-edited or ^{13}C-edited ^{1}H NMR spectra were acquired at 27 °C on Varian INOVA500 with 3000 transients for total acquisition time of about an hour. A typical experiment was performed by acquiring the 1D ^{15}N-edited or ^{13}C-edited ^{1}H NMR spectra of 5 μM ^{15}N- or ^{13}C- labeled sample with or without the addition of 10 μM non-labeled binding partner of interest.

3.2.4 Kinase activity assay

The kinase activity was measured by the incorporation of radioactive ^{32}P-ATP into the generic kinase substrate, myelin basic protein (MBP), which can be phosphorylated by most kinases. The kinase assay reaction buffer contains 20 mM HEPES, pH 7.6, 10 mM $MgCl_2$, 10 mM phosphatase inhibitor β-glycerolphosphate, 1 mM freshly added DTT, and ^{32}P-ATP. The proteins and 2mg MBP were incubated in 20μL kinase assay buffer at 30 °C for 30 minutes. The reactions were stopped by addition of 4 x SDS loading buffer, followed by boiling at 95 °C for 5 minutes and subjected to SDS-PAGE. The gel was wrapped in plastic wrap and exposed to X-ray film with intensifying screens. MAP kinase ERK was used as a positive control in the kinase activity assay.

3.2.5 Isothermal titration calorimetry (ITC)

ITC experiments were performed using a VP-ITC system (MicroCal, Northampton, Massachusetts, United States) at 20 °C in a buffer composed of 20 mM HEPES, pH 8.0, 150

mM NaCl, and 0.5 mM TCEP. The proteins were extensively dialyzed against the ITC buffer, centrifuged, and degassed before the experiment. Typically, 190-200 μM Munc13-1 MUN domain was injected in 35 aliquots of 8 μl into a 1.8 ml sample cell containing 17-19 μM Munc18. The ITC data were fitted with a nonlinear least squares routine using a single-site binding model with the software MicroCal Origin^{TM} for ITC, varying the stoichiometry (n), the enthalpy of the reaction (ΔH) and the association constant (Ka), whose reciprocal is the dissociation constant (Kd).

3.2.6 Brain homogenate preparation

Ten frozen rat brains were thawed on ice and cut into small pieces with razors. Brain homogenization buffer A containing 20 mM HEPES, pH 7.4, 2 mM phenylmethylsulphonyl fluoride (PMSF) were added to the brain pieces. The mixture was dounced eight times with a variable speed electric motor drive homogenizer (Thomas Scientific). Equal volume of brain homogenization buffer B containing 20 mM HEPES, pH 7.4, 200 mM NaCl, 2 % (w/v) sodium cholate was added after the homogenization and the mixture was rotated at 4°C for 2 hours in the cold room to facilitate the release of proteins whereas to avoid bubble generation. The brain homogenate was clarified by ultracentrifugation at 37,500 rpm with a Ti-45 rotor for 60 minutes at 4°C.

3.2.7 Cross-linking experiment

Cross-linking experiments were performed to identify the potential binding partners of Munc13 MUN domain in the brain homogenate. In a typical cross-linking experiment, the T7-tagged Munc13-1 MUN domain or Munc18 was mixed with rat brain homogenate, followed by the addition of cross-linker and incubation at room temperature. For cross-linker 1-Ethyl-3-[3-dimethylaminopropyl] carbodiimide hydrochloride (EDC), the concentration used in the reaction was 0.625 mg/ml and the reaction was incubated at room temperature for 1 hour. For cross-linker Bis (Sulfosuccinimidyl) suberate (BS3), the concentration used in the reaction was 0.25 mg/ml and the reaction was incubated at room temperature for 30 minutes. The cross-linking reaction was stopped after incubation by adding 1 M Tris, pH8.0 to a final concentration at 25 mM. The cross-linking products were subjected to SDS-PAGE, followed by western blotting with anti-T7 antibody.

3.2.8 Protein kinase C (PKC) assay

The reaction was performed with a PKC assay kit from Upstate biotechnology. The reaction was set up by mixing PKC, Munc18, Mg^{2+}/ATP, lipid activator (which contains phosphatidylserine as well as diacylglycerol and needs to be sonicated before each use) and incubating at 30 °C for two hours. A control experiment was set up by omitting the PKC kinase.

3.2.9 Pro-Q Diamond phosphoprotein staining

The samples were subjected to SDS-PAGE. The gel was initially fixed twice for 30 minutes with gentle agitation (50 rpm on an orbital shaker) in 100 ml fix solution composed of 50% (v/v) methanol and 10% (v/v) acetic acid to completely remove the SDS from the gel. The fixed gel was washed three times for 10 minutes with gentle agitation in 100ml Milli-Q H_2O to completely remove the methanol and acetic acid from the gel since the residual methanol or acetic acid will interfere with Pro-Q® Diamond phosphoprotein staining. For staining, incubate the gel in 60 ml Pro-Q® Diamond phosphoprotein gel stain for one to one and half hour in a polypropylene container (to minimize the absorption of the dye to the plastics surface) with gentle agitation, protected from light in alumina foil to prevent photobleaching of the fluorescent dye. For destaining, the gel was incubated in 100ml destain solution composed of 20% (v/v) acetonitrile, 50 mM sodium acetate, (pH 4.0) three times for 30 minutes with gentle agitation to reduce the gel background signal. The destained gel was further washed twice for 5 minutes with gentle agitation in 100ml Milli-Q H_2O before imaging. The gel was imaged with FLA-5100 gel scanner (Fuji Photo Film Co, Ltd.) with 532 nm green laser excitation and 580 nm longpass emission filter set (LPG filter).

3.2.10 SYPRO® Ruby protein gel staining

SYPRO® Ruby protein gel staining stains the total proteins in the sample. After SDS-PAGE, the gel was initially fixed twice for 30 minutes with gentle agitation in 100 ml fix solution composed of 50% (v/v) methanol and 7% (v/v) acetic acid. The fixed gel was stained in 60 ml SYPRO® Ruby protein gel stain overnight with gentle agitation, protected

from light in aluminum foil. The stained gel was transferred to a clean container and washed in 100 ml wash solution composed of 10% (v/v) methanol and 7% (v/v) acetic acid for 30 minutes, followed by rinse with Milli-Q H_2O twice for 5 minutes. The gel was imaged with FLA-5100 gel scanner (Fuji Photo Film Co, Ltd.) with 473 nm blue laser excitation and 580 nm longpass emission filter set (LPG filter) or 515 nm longpass emission filter set (LPB filter).

SYPRO® Ruby protein gel staining can also be performed after the Pro-Q® Diamond phosphoprotein staining, which will yield the information of the relative phosphorylation level of a given protein. The gel stained with Pro-Q® Diamond phosphoprotein stain can be directly stained by SYPRO® Ruby protein gel stain overnight with gentle agitation, protected from light in aluminum foil, after a brief rinse with Milli-Q H_2O twice without further fixation. The stained gel was washed in 100 ml wash solution composed of 10% (v/v) methanol and 7% (v/v) acetic acid for 30 minutes, followed by rinse with Milli-Q H_2O twice for 5 minutes before imaging.

3.3 Results

3.3.1 Candidate strategy of testing the putative binding partner of Munc13-1 MUN domain

It has been shown that Munc13 C_2A, C_1 and C_2B domains interact with RIM zinc

finger domain, DAG/phorbol ester and Ca^{2+}, respectively. But the interactions of the MUN domain and the C_2C domain are still unclear. The observation that the introduction of "open" conformation syntaxin LE mutant can rescue the neurotransmitter release in Munc13 knockout *C. elegans* suggested an important functional interaction between Munc13 and syntaxin (Richmond et al., 2001). GST pull-down experiments suggested that syntaxin binds to the Munc13 through sequence within its MUN domain (Betz et al., 1997). Moreover, some results from Nile Brose's group have suggested that the Munc13-1 C_2C domain is also involved in syntaxin interaction (Stevens et al., 2005). Based on all these results, I initially started to study the interaction between syntaxin and a Munc13-1 fragment encompassing both the MUN domain and the C_2C domain, referred to as the $MUNC_2C$ fragment.

I first tested the interaction between $MUNC_2C$ and syntaxin cytoplasmic fragment spanning 2-253 residues using a size exclusion chromatographic binding assay. The mixture of $MUNC_2C$ and syntaxin runs as two separate peaks at the positions of $MUNC_2C$ or syntaxin alone on the S200 column (Figure 3.1A). The SDS-PAGE of TCA precipitated fractions shows no co-migration of $MUNC_2C$ and syntaxin (Figure 3.1B). These results suggested that there is no interaction between $MUNC_2C$ and syntaxin.

Next, I tested the interaction between $MUNC_2C$ and ^{15}N-labeled syntaxin SNARE motif spanning 191-253 residues using ^{15}N-edited 1D HSQC experiment. The rationale of this method is that the binding of unlabeled protein B to ^{15}N-labeled protein A will cause a decrease of the NMR signal of protein A due to the increase of molecular weight

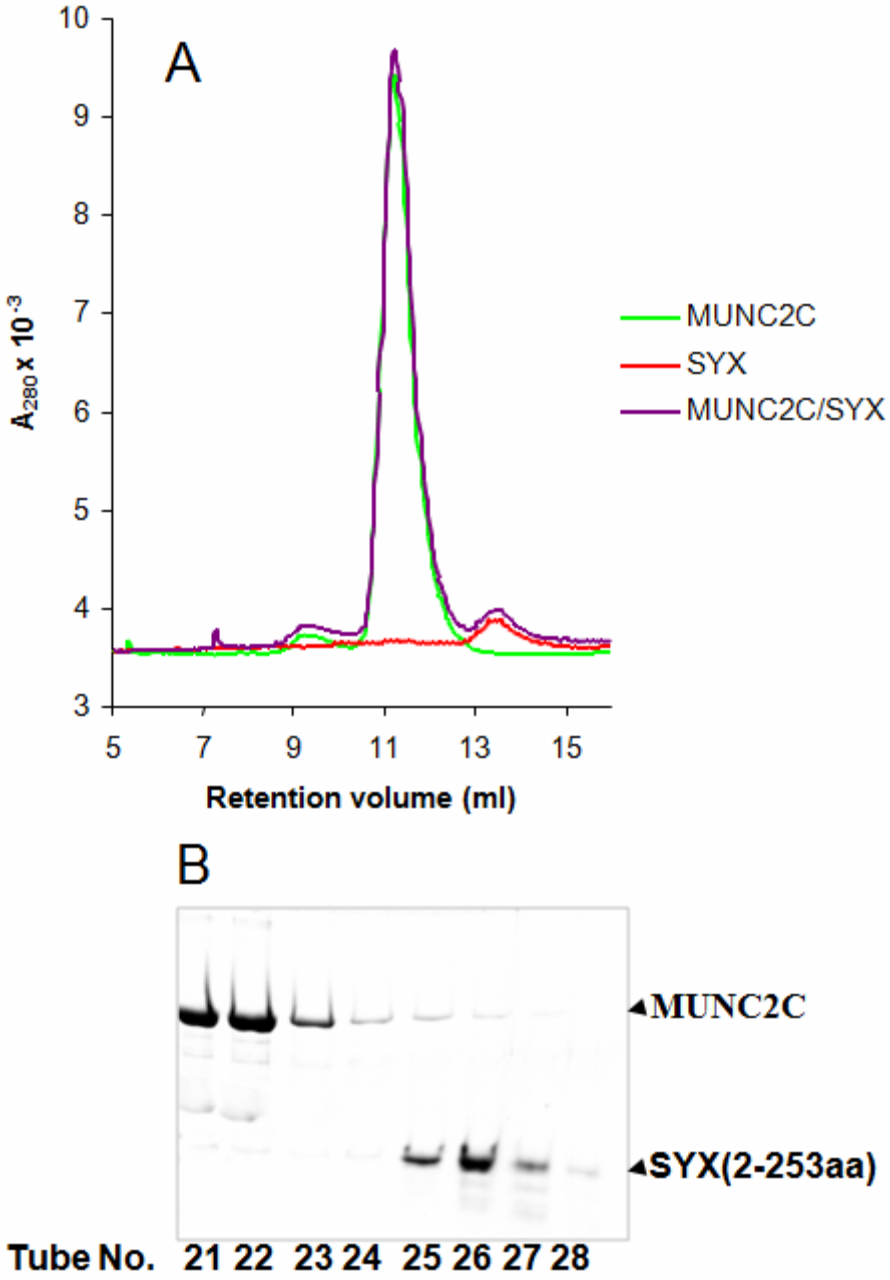
A
10
9
8
7
6
5
4
3
A_{280} x 10^{-3}
5
7
9
11
13
15
Retention volume (ml)
MUNC2C
SYX
MUNC2C/SYX
B
MUNC2C
SYX(2-253aa)
Tube No. 21 22 23 24 25 26 27 28

Figure 3.1 Interaction between $MUNC_2C$ and syntaxin (2-253) analyzed by size exclusion chromatographic binding assay

(A) Size exclusion chromatograms of $MUNC_2C$ alone (green), syntaxin (2-253) alone (red), and the mixture of equal molar $MUNC_2C$ and syntaxin (2-253) (magenta).

(B) The fractions from the size exclusion chromatographic elution of the mixture of equal molar $MUNC_2C$ and syntaxin (2-253), analyzed by TCA precipitation, SDS-PAGE and Coomassie blue staining.

(Arac et al., 2003). In contrast, no change of the signal will indicate a lack of interaction between protein A and protein B(Arac et al., 2003). Comparison of ^{15}N-edited 1D HSQC spectra of ^{15}N-labeled syntaxin (191-253) in the presence or absence of MUNC$_2$C revealed no significant change of the ^{15}N-edited 1D HSQC signal intensity, suggesting no interaction detected between MUNC$_2$C and syntaxin SNARE motif (Figure 3.2).

Another possibility is that MUNC$_2$C interacts with the syntaxin closed conformation stabilized by Munc18. Therefore, I also tested the interaction between MUNC$_2$C and syntaxin/Munc18 complex using a size exclusion chromatographic binding assay, which turned out to be negative. This binding assay also showed that MUN couldn't disrupt the interaction between Munc18 and syntaxin.

Besides syntaxin/MUNC$_2$C interaction, I also tested the interaction between the Munc13-1 MUN domain and GTPase dynamin using a size exclusion chromatographic binding assay. I speculated the existence of this potential interaction based on three lines of evidence. Firstly, previous GST pull-down studies in our lab suggested that GST-MUN fusion protein can pull down dynamin from the rat brain homogenate. Secondly, it has been reported that the ubiquitously expressed Munc13-4 isoform binds to GTPase Rab27 in a GTP-dependent manner and regulates the cytolytic granule secretion in the immunological synapse (Feldmann et al., 2003; Shirakawa et al., 2004). Thirdly, 3D fold prediction of MUN reveals a similarity to importin, which forms a superhelical structure and binds to GTPase Ran in a GTP-dependent manner (Chook and Blobel, 1999). However, this interaction also

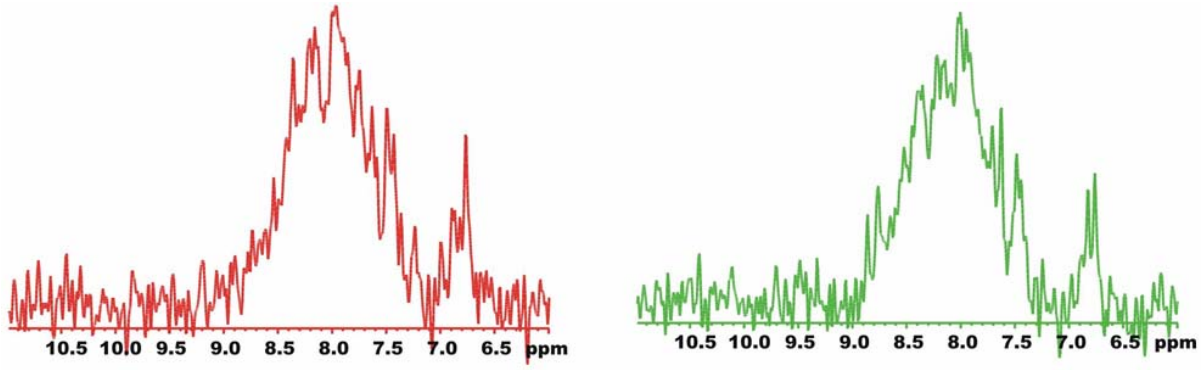

Figure 3.2 Interaction between $MUNC_2C$ and syntaxin (191-253) analyzed by ^{15}N-edited 1D NMR experiment

The ^{15}N-edited 1D HSQC of 5μM ^{15}N-labeled syntaxin (191-253) before (red) and after (green) addition of 10 μM unlabeled $MUNC_2C$.

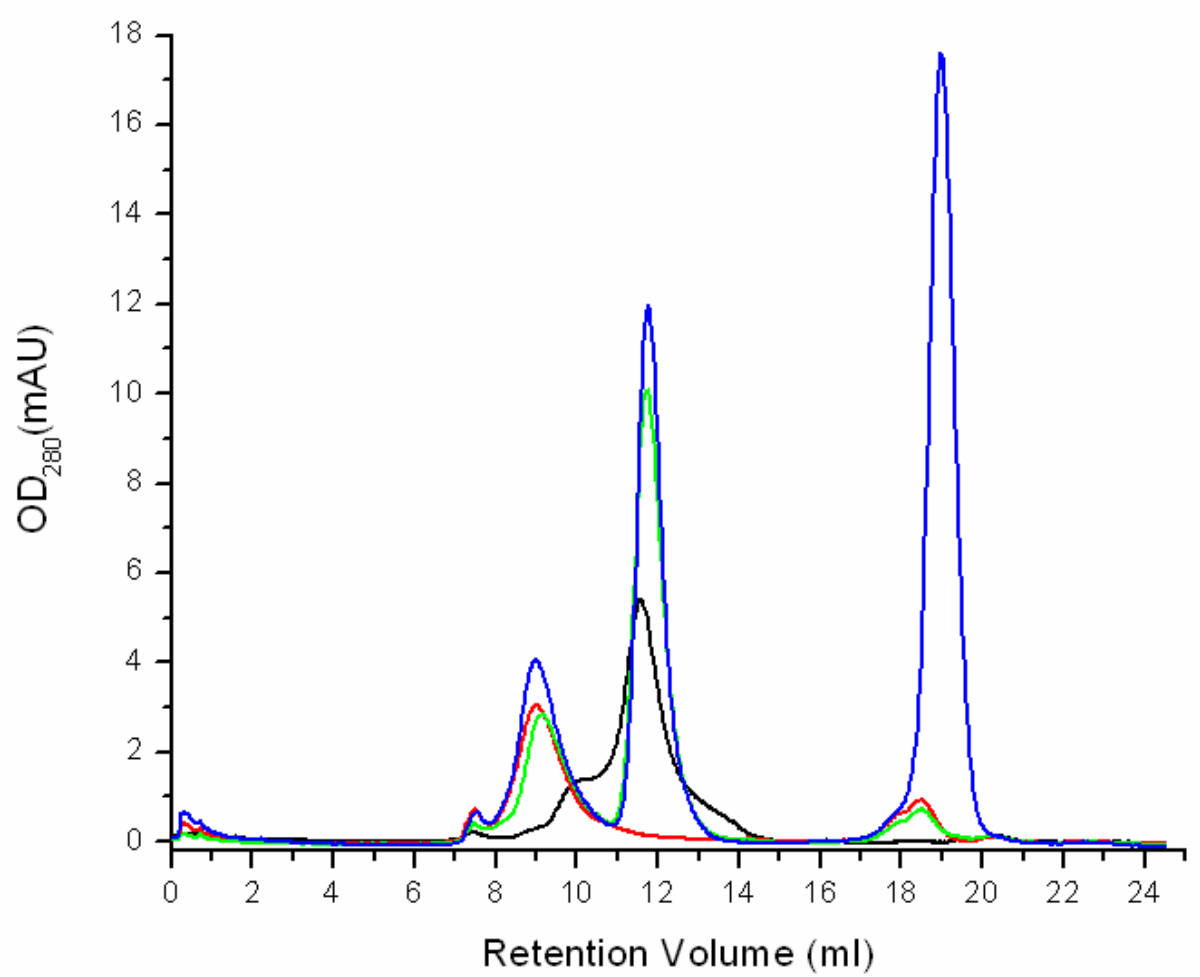

Figure 3.3 Interaction between MUN and dynamin analyzed by size exclusion chromatographic binding assays

Size exclusion chromatograms of MUN alone (black), dynamin alone (red), and the mixture of equal molar MUN and dynamin in the presence (blue) or absence (green) of GTPγS.

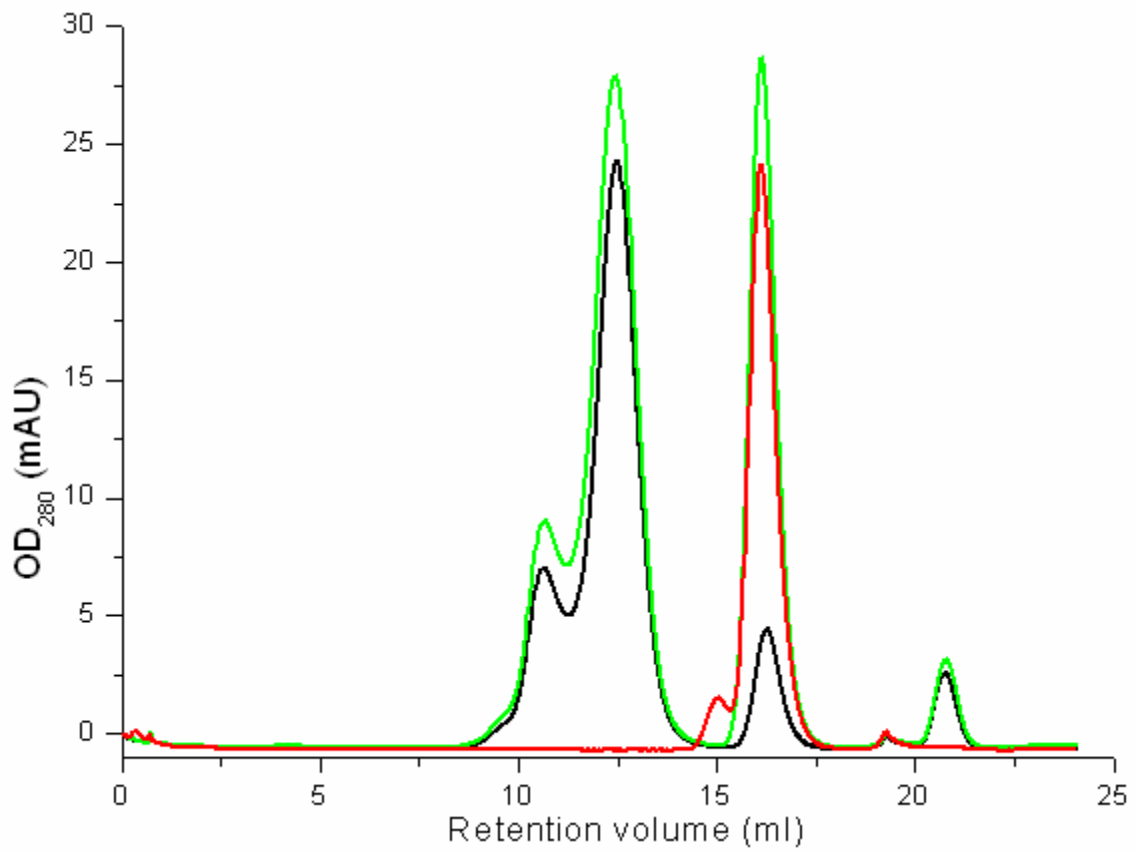

Figure 3.4 Interaction between MUN and Rab3A (Q81L) analyzed by size exclusion chromatographic binding assays

Size exclusion chromatograms of MUN alone (black), Rab3A (Q81L, a constitutively active mutant) alone (red), and the mixture of equimolar MUN and Rab3A (Q81L) (green).

turned out to be negative (Figure 3.3). I also tried another GTPase known to be involved in synaptic neurotransmission, Rab3A, which might be analogous to the Munc13-4/Rab27 interaction. Unfortunately, it still turned out to be negative (Figure 3.4).

3.3.2 Test the kinase activity of Munc13-1 MUN domain

Interestingly, the central Munc13-1 fragment shares a similar domain arrangement with protein kinase C (PKC). PKC contains two C_1 domains, followed by a C_2 domain and a kinase domain (Newton, 1995). The central fragment of Munc13-1 contains a C_1 domain, a C_2 domain and a MUN domain. This similar domain arrangement motivated us to try to determine whether the Munc13-1 MUN domain might possess kinase activity. I tested this hypothesis using a kinase activity assay with MBP as the kinase substrate. MBP was chosen as a substrate because it can be phosphorylated by most kinases. Syntaxin and Munc18 were also incorporated in the assay to test whether they might be phosporylated by the MUN domain or whether they might activate the kinase activity of the MUN domain. Recombinant MAP kinase ERK was used as a positive control in the kinase assay. The phosphorylation of MBP by ERK as well as the auto-phosphorylation of ERK could be observed clearly on the exposed film. However, no phosphorylation of MBP, syntaxin or Munc18 by the MUN domain was observed, indicating that the Munc13-1 MUN domain doesn't possess kinase activity (Figure 3.5).

3.3.3 Cross-linking experiments to identify binding partners of Munc13-1 MUN

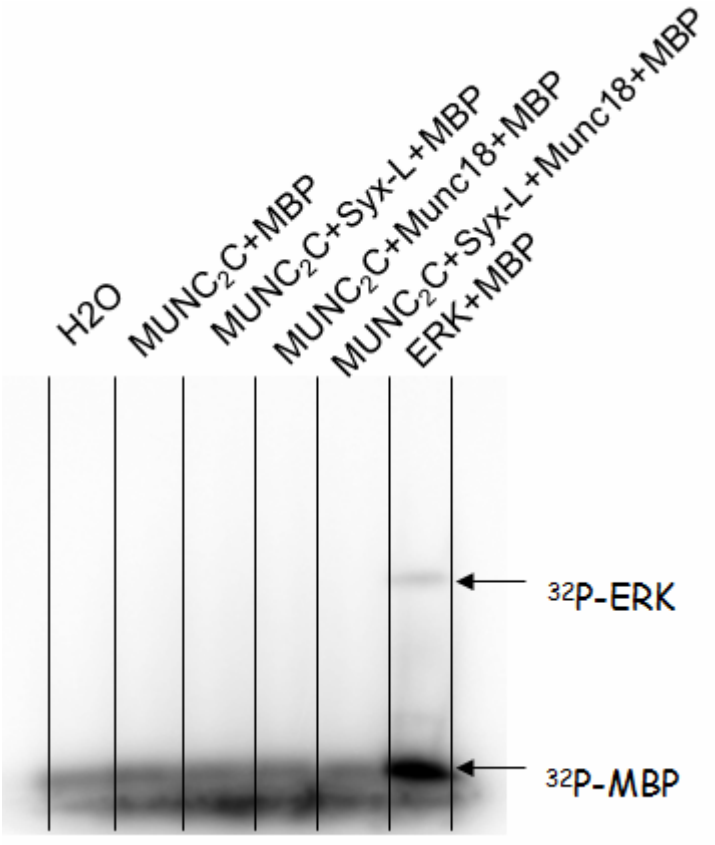

Figure 3.5 $MUNC_2C$ kinase activity assay

The $MUNC_2C$ kinase activity reactions were analyzed by SDS-PAGE, followed by autoradiography. The components of each reaction are labeled on the top of each lane. The phosphorylated MBP and auto-phosphorylated ERK are indicated by arrows.

domain from rat brain homogenate

All the previous experimental results turned out to be negative. The failure of candidate screening method motivated us to use a more unbiased method to fish out potential MUN-interacting molecules. Unfortunately, yeast-two-hybrid experiments performed in our collaborator Dr. Thomas Südhof's lab didn't yield any promising hits. Therefore, I performed cross-linking experiments between the Munc13-1 MUN domain and rat brain homogenate, trying to find potential interaction partner of the MUN domain. Since I don't have an antibody against the Munc13-1 MUN domain, I decided to add an N-terminal T7 tag to the MUN domain construct to facilitate the detection of MUN domain-containing cross-linking products by western blotting as well as the enrichment of the cross-linking product by immunoprecipitation.

In cross-linking experiments, firstly, T7 tagged MUN domain was mixed with rat brain homogenate, followed by cross-linking. The cross-linking product was analyzed with SDS-PAGE, followed by western blotting using anti-T7 antibody. Observation of anti-T7 antibody recognized bands with molecular weight higher than T7 tagged MUN indicated the formation of covalent adducts of MUN and its binding partners. I tried two types of cross-linking reagents, EDC and BS3. EDC is a carboxyl- and amine-reactive zero-length cross-linker. BS3 is a water-soluble homobifunctional cross-linker with a spacer arm of 11.4 Å. The N-hydroxysuccinimide ester (NHS ester) groups of BS3 react efficiently with primary amino groups (-NH2) to form stable amide bonds in solution of pH 7-9, therefore mainly

crosslinking proteins at the primary amines of lysine side chain. For both EDC and BS3, four similar and distinct bands (cross-linking products) were observed on the western blotting using anti-T7 antibody. Figure 3.6 showed the western blotting of the cross-linking products between the MUN domain and rat brain homogenate using EDC and BS3 cross-linker. Since BS3 seemed to work a little bit better than EDC, I kept using BS3 in the later cross-linking experiments.

Initially, immunoprecipitation experiments using anti-T7 antibody and protein A/G resins were performed to purify and enrich the cross-linking products of Munc13-1 MUN domain. However, the immunoprecipitation efficiency and purification efficiency were quite low. Therefore, chromatographic purifications using an FPLC system were applied to purify and enrich the cross-linking products of Munc13-1 MUN domain. The cross-linking products were purified sequentially through a Superdex 200 gel filtration column and a source Q anion exchange column. The gel filtration and ion exchange chromatographs are shown in Figure 3.7. After both gel filtration and anion exchange chromatographic purifications, about 70% of the bulk proteins were removed from the cross-linking product-containing pool. After FPLC purification, it was still difficult to pinpoint the cross-linking products unambiguously on the colloidal blue stained gel. Therefore, I continued the efforts to enrich the cross-linking products. On one hand, I tried to concentrate the cross-linking products using different types of high molecular weight cutoff concentrators. On the other hand, I tried to enrich the cross-linking products by changing the single T7 tag to a double or triple T7 tag, which might improve the immunoprecipitation efficiency to simplify and improve the purification. I

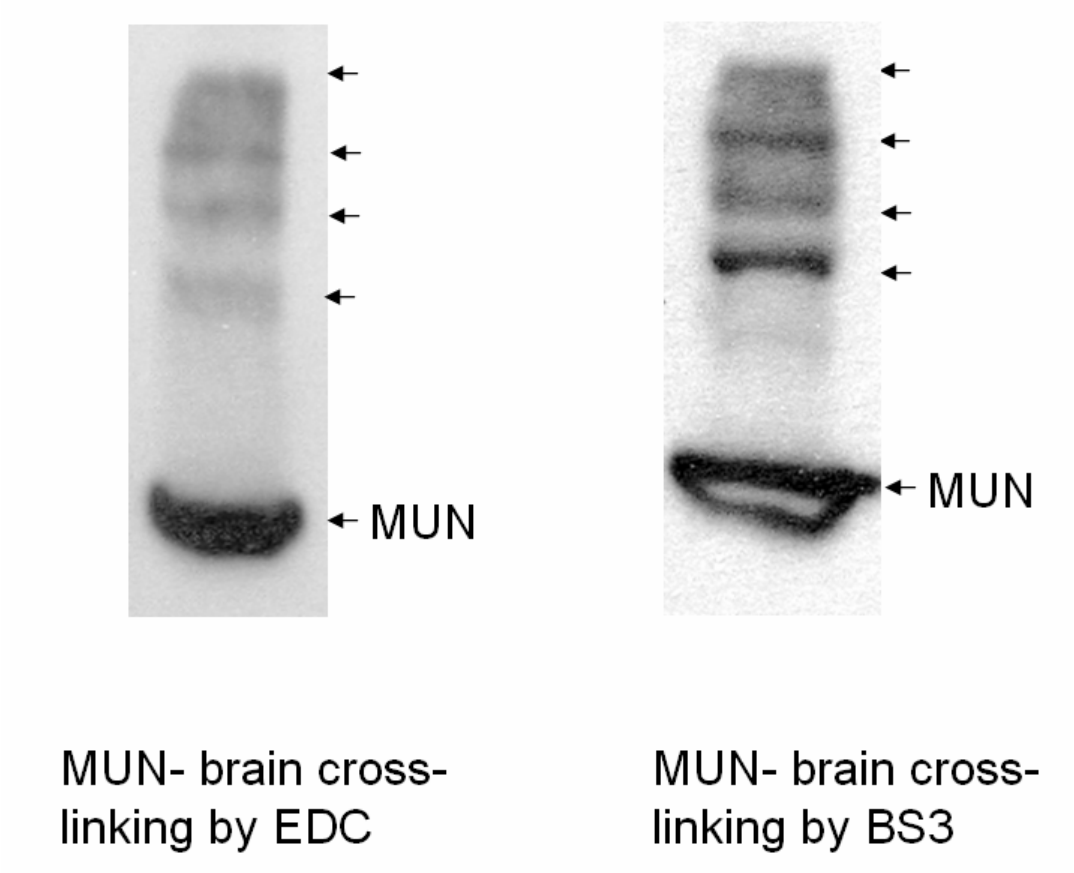

Figure 3.6 Western blotting analyses of Munc13-1 MUN domain cross-linking products

The cross-linking products of Munc13-1 MUN domain generated by EDC (left) or BS3 (right), analyzed by western blotting with anti-T7 antibody. The MUN domain and the four dominant cross-linking bands are indicated by arrows.

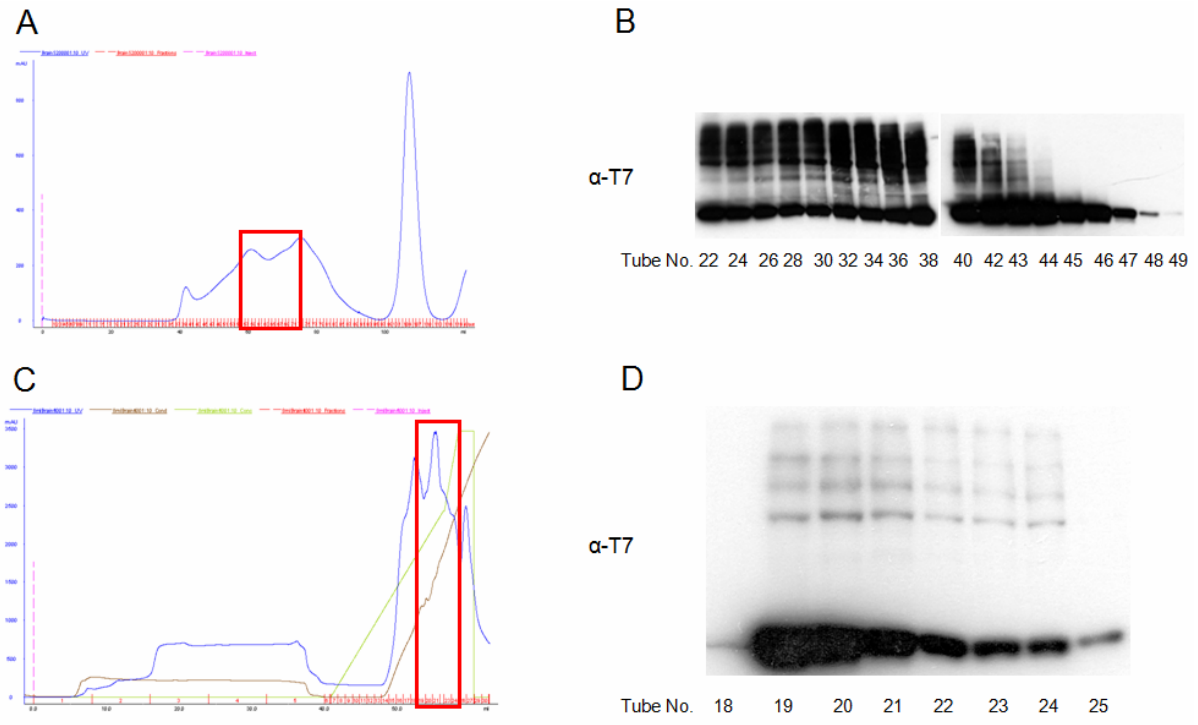

Figure 3.7 Chromatographic purification of Munc13-1 MUN domain cross-linking products

(A) Gel filtration chromatograph of Munc13-1 MUN domain cross-linking products purification.

(B) The fractions from the gel filtration chromatographic purification of Munc13-1 MUN domain cross-linking products, analyzed by western blotting with anti-T7 antibody.

(C) Anion exchange chromatograph of Munc13-1 MUN domain cross-linking products purification.

(D) The fractions from the anion exchange chromatographic purification of Munc13-1 MUN domain cross-linking products, analyzed by western blotting with anti-T7 antibody.

successfully made the MUN constructs with two or three T7 tags and immunoprecipitation experiments did show the enrichment of the T7 tagged proteins. However, enrichment by either concentration or multiple T7 tag immunoprecipitation promoted nonspecific aggregation, which complicated the cross-linking band identification.

Even though the four cross-linking product bands were not unambiguously clear in the colloidal blue stained gel, we decided to cut the regions corresponding to the molecular weight of cross-linking product bands in the western blots (130 kDa, 160 kDa, 200 kDa, and 250 kDa) and submit them to the campus mass spectrometry facility for protein identification. For each band, about 18-20 proteins were identified. A selected subset of the identified proteins is listed in Table 3.1. Interestingly, all four bands contain Munc18-1, part of the central fusion machinery, which was further studied in more details in 3.3.4.

I also performed cross-linking experiments between Munc18-1 and rat brain homogenate, initially as a positive control to check its cross-linking with syntaxin 1A. However, the higher molecular weight cross-linking products appeared as continuous smears and it was impossible to discern distinct bands, presumably due to the “sticky” properties of syntaxin (Jahn and Scheller, 2006). Interestingly, a prominent cross-linking product was observed at the molecular weight of about 75 kDa, 7 kDa larger than Munc18 (Figure 3.8). This band was also submitted to the mass spectrometry facility for protein identification. Mass spectrometry results suggested that this band contains several proteins, among which the most interesting one is ubiquitin with a molecular weight about 9 kDa, suggesting the

Table 3.1 A selected subset of the identified proteins in the Munc13-1 MUN domain cross-linking products

MW on Gel	Protein Name	Protein MW
130 (18 proteins IDed)	Munc13	196.2
	Munc18	67.5
160 (19 proteins IDed)	Munc13	196.2
	Neural cell adhesion molecule 1	94.6
	Neurochondrin	78.8
	Munc18	67.5
200 (18 proteins IDed)	Munc13	196.2
	CAPS	146.2
	Ankyrin binding cell adhesion molecule neurofascin	135.4
	ATPase, Ca^{2+} transporting, plasma membrane 2	132.5
	Na, K ATPase alpha-1 subunit	113.2
	Munc18	67.5
250 (20 proteins IDed)	Munc13	196.2
	Leucine rich protein 157 precursor	156.6
	Munc18	67.5

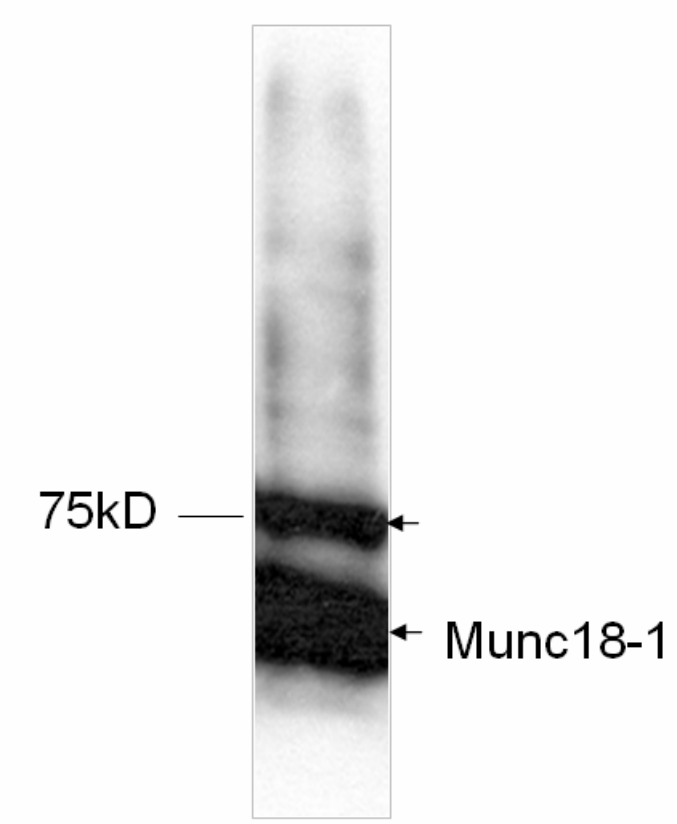

Figure 3.8 Western blotting analyses of Munc18-1 cross-linking products

The cross-linking products of Munc18-1, analyzed by western blotting with anti-T7 antibody. Munc18-1 and the dominant 75kD cross-linking band are indicated by arrows.

possibility that the cross-linking band at 75 kDa might correspond to mono-ubiquitinated Munc18 or the complex of Munc18-1 and ubiquitin. I tested the direct interaction between Munc18 and ubiquitin using a size exclusion chromatographic binding assay, which turned out to be negative (Data not shown).

3.3.4 Studies of the interaction between recombinant Munc13-1 MUN domain and Munc18-1

Cross-linking experiments suggested that recombinant Munc13-1 MUN domain interacts with Munc18 from the rat brain homogenate. Therefore, I tried to use isothermal titration calorimety (ITC) to determine the binding stoichiometry and affinity of the Munc18/MUN interaction, which will be helpful to understand whether it is a specific and meaningful interaction. However, the ITC isotherm of titrating 190 μM MUN domain into 18.7 μM Munc18 did not yield a reasonable fit and suggested no binding between recombinant Munc18 and MUN domain (Figure 3.9A). To address the possibility that the binding heat was masked by the dilution heat of the highly concentrated MUN domain, I performed a control experiment where the MUN domain was titrated into buffer alone to obtain the dilution heat, shown in Figure 3.9B. Figure 3.9C shows the isotherm after the subtraction of the dilution heat from the raw data, which still failed to generate a trustable fit for the binding, suggesting again no binding between recombinant Munc18 and MUN domain.

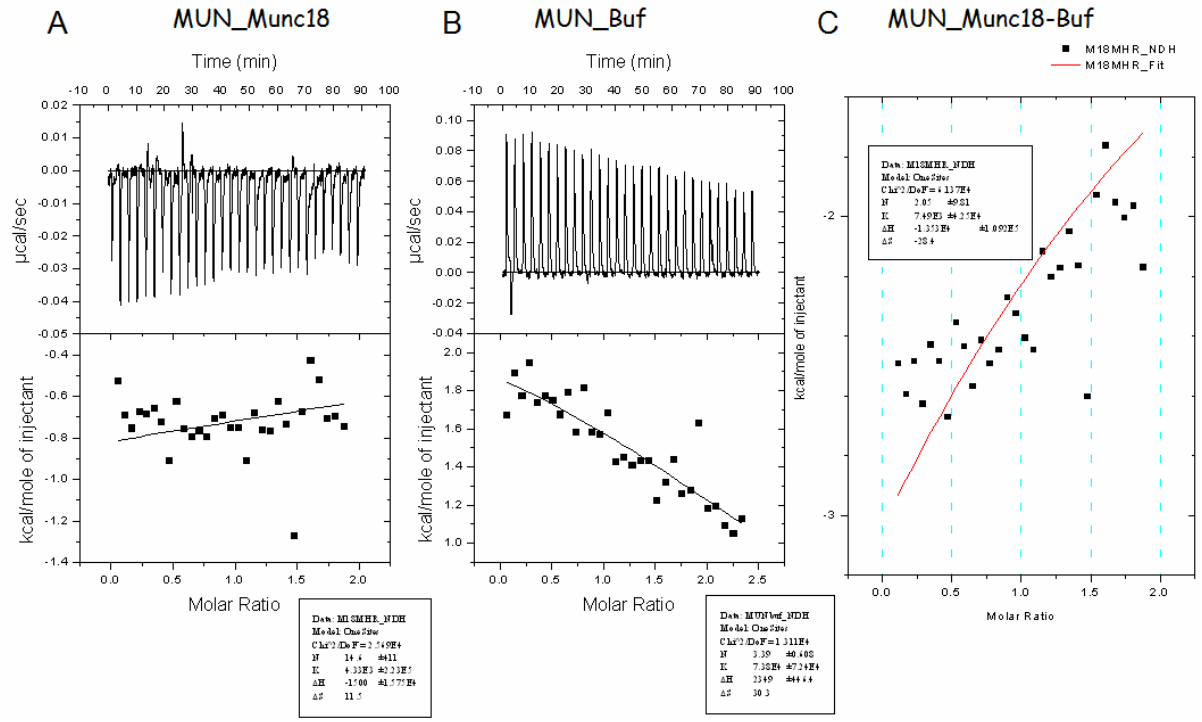

Figure 3.9 Isothermal titration calorimetry (ITC) analysis of the interaction between recombinant Munc18-1 and Munc13-1 MUN domain

(A) ITC isotherm of Munc13-1 MUN domain titrated into Munc18-1, which failed to generate a reasonable binding isotherm fit.

(B) ITC isotherm of the control experiment where Munc13-1 MUN domain was titrated into ITC buffer.

(C) ITC isotherm after the subtraction of the dilution heat (B) from the raw data (A), which failed to generate a reasonable binding isotherm fit.

Then I carried out ^{13}C-edited 1D NMR binding experiments to test the interaction between ^{13}C-labeled Munc18 and the unlabeled MUN domain. The rationale of this method is similar to that of ^{15}N-edited 1D NMR binding experiments (Arac et al., 2003). Essentially, the binding of unlabeled protein B to ^{13}C-labeled protein A will cause a decrease of the NMR signal of protein A due to the increase of molecular weight. In contrast, no change of the signal will indicate lack of interaction between protein A and protein B. The interaction between Munc18 and SNARE complex was used as a positive control (Dulubova et al., 2007). The ^{13}C-edited 1D NMR signal intensity of ^{13}C-labeled Munc18 decreased dramatically upon addition of unlabeled SNARE complex, confirming that Munc18 interacts with the SNARE complex. However, comparison of ^{13}C-edited 1D NMR spectra of ^{13}C-labeled Munc18 in the presence or absence of unlabelled MUN domain revealed no significant change of the ^{13}C-edited 1D NMR signal intensity, suggesting no interaction detected between Munc18 and the MUN domain (Figure 3.10).

3.3.5 Phosphorylation of Munc18-1

The interaction between Munc18-1 and the Munc13-1 MUN domain tested by the ITC experiments and the ^{13}C-edited 1D NMR binding experiments turned out to be negative. Because our data were obtained in solution with well-folded proteins using ITC that is highly quantitative and the ^{13}C-edited 1D NMR experiment that provides a very sensitive tool to detect protein-protein interactions, our results conclusively showed that at least this recombinant Munc18-1 and the MUN domain expressed in bacteria do not form binary

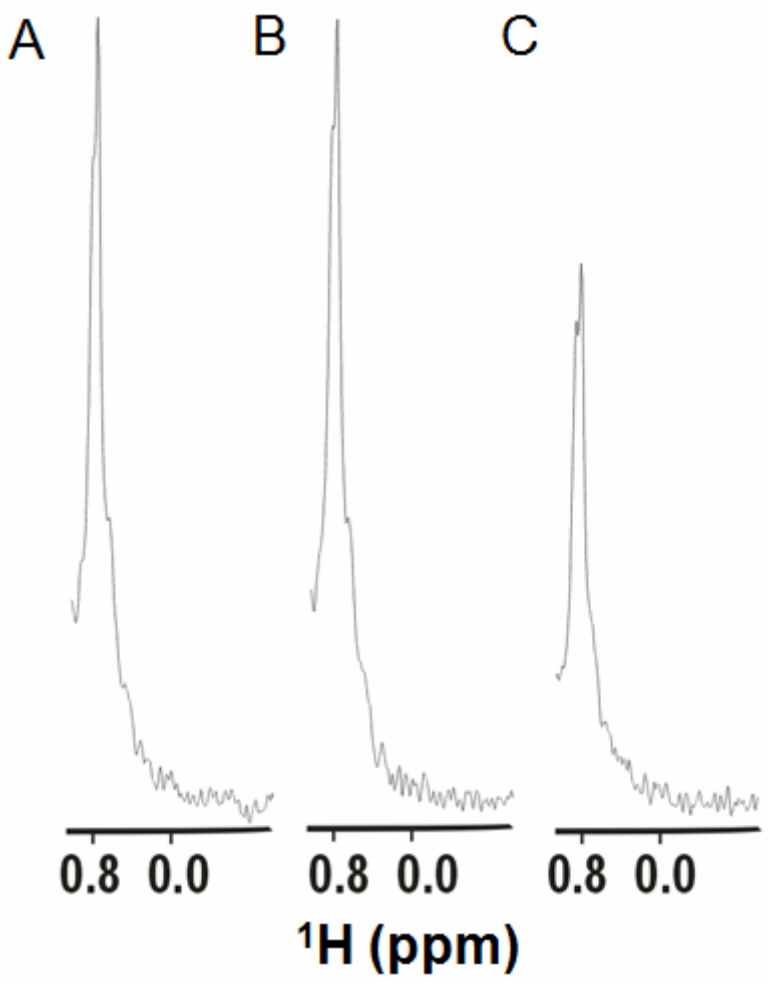

Figure 3.10 Interaction between Munc18-1 and Munc13-1 MUN domain analyzed by ^{13}C-edited 1D NMR experiment.

(A) The ^{13}C-edited 1D NMR spectra of 2 μM ^{13}C-labeled Munc18-1.

(B) The ^{13}C-edited 1D NMR spectra of 2 μM ^{13}C-labeled Munc18-1 in the presence of 2.5 μM unlabeled Munc13-1 MUN domain .

(C) The ^{13}C-edited 1D NMR spectra of 2 μM ^{13}C-labeled Munc18-1 in the presence of 2.5 μM unlabeled SNARE complex.

complexes in solutions. However, how can we explain the observation that the MUN domain cross-linked with Munc18-1 from the brain homogenate? I speculated that the failure to detect the interaction between recombinant Munc18-1 and MUN domain might result from something different between the recombinant system and the endogenous brain homogenate, for example, the posttranslational modification of Munc18-1 or the existence of some X factor to mediate the indirect interaction between Munc18-1 and MUN domain. To address these possibilities, I firstly performed a GST pull-down from brain homogenate using GST-MUN fusion protein immobilized on glutathione resin in the presence or absence of phosphatase inhibitor. I found that, interestingly, more Munc18-1 from the brain homogenate could be pulled down by GST-MUN after 500 mM NaCl wash compared to the GST pull-down results without phosphatase inhibitor. This immediately suggested that phosphorylation of Munc18-1 might be essential for its interaction with the Munc13-1 MUN domain.

To test whether the Munc18-1 pull-downed from the brain homogenate is phosphorylated, I performed a dephosphorylation assay on the pull-downed endogenous Munc18-1 in the 1 M NaCl eluate using calf intestine phosphatase (CIP) treatment. CIP treatment caused a faster apparent gel mobility of Munc18-1 compared to the non-treated sample, strongly suggesting that the pull-downed endogenous Munc18-1 in the 1 M NaCl eluate by GST-MUN was phosphorylated (Figure 3.11). In contrast, CIP treatment of Munc18-1 pull-downed from brain homogenate by GST-syntaxin didn't result in an obvious gel mobility shift, suggesting that the regulation of Munc18-1 interaction by phosphorylation

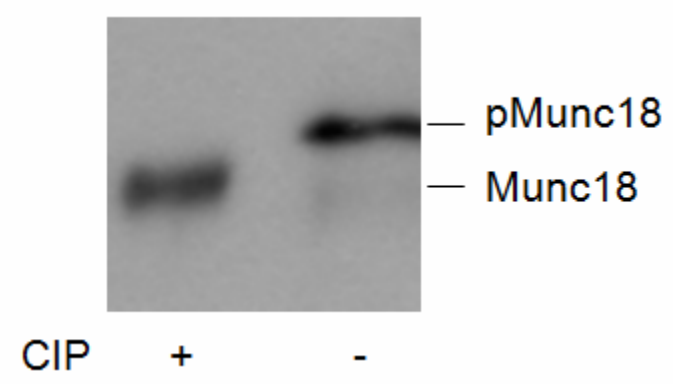

Figure 3.11 Dephosphorylation assay on the endogenous Munc18-1 pull-downed from brain homogenate

The endogenous Munc18-1 pull-downed from brain homogenate with (left) or without (right) the CIP treatment, analyzed by western blotting with anti-T7 antibody.

might be specific to the MUN domain.

To characterize the interaction between phosphorylated Munc18-1 and the MUN domain, I tried to identify the phosphorylation sites essential for modulating the interaction. To this end, I tried two approaches. Firstly, I tried to repeat the pull-down experiment with larger amounts of brain homogenates or with synaptosomes to increase the amount of pull-downed phosphorylated Munc18-1. After I pulled down enough phosphorylated Munc18-1 to see a clear band with sufficient intensity on the colloidal blue stained gel, the band was cut out and submitted to the mass spectrometry facility for phosphorylation site(s) identification. The first mass spectrometry attempt resulted in about 20% coverage of Munc18-1 sequence in the peptide fragments identified, which was not enough to lead to a successful phosphorylation site(s) identification. Moreover, it was possible that the phosphorylation could be lost during sample preparation and processing stages of the mass spectrometry. Therefore, I also tried a candidate approach to address the phosphoryaltion site(s) identification. I performed a phosphorylation site(s) analysis of the rat Munc18-1 sequence using NetPhosK 1.0 server (http://www.cbs.dtu.dk/services/NetPhosK) as well as NetPhos 2.0 server (http://www.cbs.dtu.dk/services/NetPhos). The predicted phosphorylation sites for common kinases are listed in Table 3.2. It has been reported that Munc18-1 could be efficiently phosphorylated *in vitro* by PKC at serine 306 and serine 313, and by Cdk5 at threonine 574, which in both cases decreases syntaxin 1 binding and alters the efficiency of release (Fujita et al., 1996; Shuang et al., 1998; Fletcher et al., 1999). The Ser313 site is particularly interesting because phosphorylation at this site is rapidly increased upon

Table 3.2 Munc18-1 phosphorylation sites prediction

Site	S-42	S-42	S-43	T-56	T-78	S-80	S-86	S-89	T-96
Kinase	RSK	PKA	PKC	CKII	cdc2	PKC	CKI	PKC	PKC
Score	0.54	0.61	0.83	0.56	0.53	0.61	0.54	0.69	0.62
Site	T-107	S-142	S-142	S-155	S-158	T-182	T-218	T-218	S-228
Kinase	cdc2	DNAPK	ATM	PKC	p38MAPK	PKC	CKII	PKG	ATM
Score	0.53	0.55	0.57	0.58	0.53	0.83	0.54	0.51	0.56
Site	S-241	S-253	S-253	Y-264	Y-264	Y-266	S-300	S-306	S-312
Kinase	cdk5	CKII	PKA	SRC	INSR	INSR	DNAPK	PKC	PKC
Score	0.54	0.5	0.58	0.54	0.58	0.51	0.61	0.71	0.8
Site	S-313	S-313	S-328	S-328	T-361	T-376	T-455	S-460	S-460
Kinase	PKC	cdc2	DNAPK	ATM	PKC	CKII	PKC	PKA	PKG
Score	0.88	0.53	0.62	0.61	0.83	0.7	0.89	0.84	0.7
Site	S-469	T-489	T-504	T-504	S-506	S-507	S-507	S-509	S-511
Kinase	PKA	CKII	PKC	cdc2	PKC	PKC	PKA	cdc2	PKC
Score	0.7	0.52	0.65	0.53	0.7	0.52	0.68	0.53	0.63
Site	S-546	Y-554	T-557	T-574	T-574	T-581	T-588	S-593	S-594
Kinase	CKII	INSR	DNAPK	p38MAPK	cdk5	PKC	CKII	CKII	CKII
Score	0.53	0.5	0.56	0.61	0.66	0.74	0.58	0.56	0.56

stimulation of synaptosomes with high KCl (Barclay et al., 2003; Craig et al., 2003).

Therefore, I first tried the phosphorylation of Munc18-1 by PKC *in vitro* using PKC assay kits. The phosphorylation of Munc18-1 was confirmed by Pro-Q Diamond phosphoprotein gel staining, which used a specialized fluorescent dye to selectively stain phosphoproteins in acrylamide gels that could be detected and recorded by a laser scanner such as Fuji FLA 5100. The same gel after Pro-Q Diamond staining was subjected to the SYPRO® Ruby protein gel staining, which quantitatively stains the total proteins. Indeed, PKC could phosphorylate Munc18-1 *in vitro*. The phosphorylation reaction product showed a strongly stained band of Munc18-1 by Pro-Q compared to the control, whereas the quantitative total protein staining actually showed less amount of Munc18-1 compared to the control (Figure 3.12). The Munc18-1 phosphorylated by PKC migrated similarly as the non-phosphorylated ones, suggesting the Munc18-1 pull-downed from brain homogenate might be hyper-phosphorylated.

To test whether the phosphorylation of Munc18-1 is essential for its interaction with the MUN domain, I tried to compare the pull-down efficiency of Munc18-1 phosphorylated by PKC and non-phosphorylated Munc18-1 by GST-MUN. The phosphorylation reaction product or Munc18-1 alone were subjected to identical GST pull-down procedures. The bound and unbound fractions were blotted with anti-Munc18-1 antibody to check the pull-down efficiency. I found that almost all the Munc18-1 in the phosphorylation reaction was bound to GST-MUN immobilized on the glutathione resins with very little in the flow-

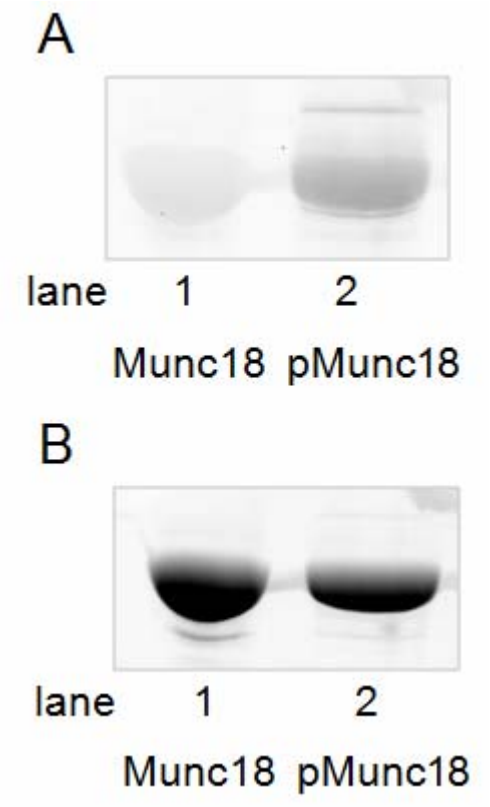

Figure 3.12 Phosphorylation of Munc18-1 by PKC

(A) ProQ-Diamond phosphoprotein staining of Munc18-1 with (Lane 2) or without (Lane 1) PKC phosphorylation.

(B) SYPRO Ruby total protein staining of the same gel as (A).

through whereas only a fraction of non-phosphorylated Munc18-1 was bound, suggesting that phosphorylation by PKC did increase the apparent affinity of Munc18-1 for MUN.

At the same time, I managed to increase the amount of phosphorylated Munc18-1 pull-downed from the brain homogenate and started the second attempt for phosphorylation site(s) identification by mass spectrometry. This time, the sequence coverage was improved significantly to about 80%. However, none of the predicted PKC phosphorylation sites was found to be phosphorylated. Actually, the only site found to be phosphorylated was serine 593, which corresponds to a predicted CKII phosphorylation site. But the physiological relevance of this observation still needs to be tested.

Chapter 4 Influence of the Membrane on Protein-protein Interactions among Proteins Involved in Neurotransmitter Release

4.1 Introduction

Membrane fusion is a very important and universal event involved in a variety of cellular activities (Rothman, 1994; Bennett and Scheller, 1993; Schekman and Orci, 1996). The SNARE proteins synaptobrevin, syntaxin 1A and SNAP-25, as well as Munc18-1 form the core of the membrane fusion machinery (Sollner et al., 1993; Chen and Scheller, 2001; Rizo and Sudhof, 2002). Many other neuronal-specific proteins such as Munc13s, RIMs and complexions, are required for the regulation of a specialized membrane fusion event occurring in neurons, neurotransmitter release (Richmond et al., 1999; Varoqueaux et al., 2002; Koushika et al., 2001; Schoch et al., 2002; Castillo et al., 2002; Reim et al., 2001). In most previous studies, the interactions among these proteins were analyzed in aqueous solution. However, native SNARE proteins are embedded in the membrane environment, which might change their biochemical behavior, sometimes dramatically (Dai et al., 2007). In this chapter, SNARE proteins were reconstituted into liposomes and the interactions among the reconstituted SNAREs, complexin I, Munc18-1, and the Munc13-1 MUN domain were studied by different methods.

4. 2 Materials and methods

4.2.1 Recombinant protein DNA construct preparation

Plasmid encoding tag-free rat full length syntaxin 1A (amino acids 2-288) as well as his-tagged rat full length SNAP-25 (amino acids 1-206) in a polycistronic vector was made using custom-designed primers and standard PCR cloning techniques and subcloned into the pETDuet co-expression vector. The syntaxin 1A construct was designed to be tag-free because previous studies from our lab have shown that the N-terminal sequence of syntaxin 1A is critical for the interaction between Munc18-1 and syntaxin 1A as well as Munc18-1/ SNARE complex interaction (Khvotchev et al., 2007).

4.2.2 Expression of recombinant proteins

4.2.2.1 Expression of his-tagged SNAP-25/syntaxin 1A complex

The plasmid encoding tandem His-tagged SNAP-25 and non-tagged syntaxin 1A, with separate individual T7 promoters, was transformed into *Escherichia coli* Rosetta (DE3) competent cells for protein expression and spread on a luria broth (LB) plate containing ampicillin.

The expression procedures of his-tagged SNAP-25/syntaxin 1A complex were similar to those for the Munc13-1 MUN domain described in chapter 2. The only differences were that the fusion proteins were expressed at 25 ºC in *Escherichia coli* Rosetta (DE3) and

induced by 0.4 mM IPTG. The harvested cell pellects were resuspended into 30 ml suspension buffer containing 50 mM Tris, pH 8.0, 300 mM KCl, 10% (v/v) glycerol, 1% (v/v) Triton X-100, 20 mM Imidazole, 0.5 mM ABESF. The harvested cell suspension was flash-frozen with liquid nitrogen and stored at -80 ºC for further protein purification.

4.2.2.2 Expression of synaptobrevin, complexin and Munc18-1

The pGEX-KG vector plasmid encoding synaptobrevin cytoplasmic fragment (amino acids 1-96) was transformed into *Escherichia coli* BL21 competent cells for protein expression and spread on a luria broth (LB) plate containing ampicillin.

The expression procedures of GST-tagged synaptobrevin were similar to those for the Munc13-1 MUN domain described in chapter 2. The only differences were that the fusion proteins were expressed at 23 ºC in *Escherichia coli* BL21 and induced by 0.4 mM IPTG. The harvested cell pellets were resuspended into 30 ml PBS buffer with freshly added protease inhibitors and DTT. The harvested cell suspension was flash-frozen with liquid nitrogen and stored at -80 ºC for further protein purification.

Complexin I and Munc18-1 were expressed using the same procedures as the synaptobrevin cytoplasmic fragment.

4.2.3 Purification of recombinant proteins

4.2.3.1 Purification of His-tagged SNAP-25/syntaxin 1A complex

The frozen cell suspensions were thawed in water bath and disrupted by passing twice through a high-pressure French press cell extruder at ~7,500 psi (Model EmulsiFlex-C5, Avestin Inc.). The cell lysate was clarified by centrifugation at 18,000 rpm for 30 minutes at 4°C in a JA-20 rotor with the Beckman centrifuge (model J2-21).

The clarified cell lysate was mixed with 1.33 ml 75% slurry of the pre-washed Ni-NTA agarose resins (QIAGEN) per liter of culture and was rotated in the cold room for 2 hours at 4 °C. The mixture was loaded into a gravity column to drain the unbound materials. The non-specifically bound proteins were removed by a series of washes with 25 ml suspension buffer. Afterwards, the resins were switched to buffer containing 1% (w/v) β-OG by washing twice with 5 bed volumes of 50 mM Tris, pH 8.0, 300 mM KCl, 1% (w/v) β-OG, 0.5 mM ABESF. The recombinant proteins were released by washing with 1 ml Ni-NTA elution buffer (50 mM Tris, pH 8.0, 300 mM KCl, 1% (w/v) β-OG, 250 mM Imidazole) 14 times. 10 µl/ml sigma inhibitor cocktail, 0.5 mM ABESF and 1 mM DTT were added into the recombinant protein immediately after elution.

The syntaxin 1A/SNAP-25 complex eluted from resin was diluted to 5 fold volumes in order to obtain low ionic strength. Then the diluted protein was purified by anion exchange chromatography through a mono Q 5/50GL column (GE healthcare life sciences). The mono

Q column was equilibrated with the low salt QA buffer (20 mM Tris, pH 8.0, 1% (w/v) β-OG, 0.5 mM TCEP). The syntaxin 1A/SNAP-25 complex was eluted with a linear gradient of the high salt QB buffer (20 mM Tris, pH8.0, 1 M NaCl, 1% (w/v) β-OG, 0.5 mM TCEP). The protein was eluted between 300 to 350 mM NaCl concentrations. The purity of the syntaxin 1A/SNAP-25 complex purified by the anion exchange column was assessed by SDS-PAGE and Coomassie blue staining. The fractions containing the pure protein were used for the reconstitution of SNARE proteins into liposomes.

4.2.3.2 Purification of synaptobrevin, complexin I and Munc18-1

The purification procedures of synaptobrevin, complexin I or Munc18-1 were similar to that of GST-tagged Munc13-1 MUN domain.

4.2.4 Assembly of SNARE complexes

SNARE complexes were assembled by mixing His-SNAP-25/Syntaxin with synaptobrevin cytoplasmic fragment and incubating the mixture at room temperature for 2 hours to overnight. The formation of SNARE complex could be checked easily on SDS-PAGE because the SNARE complexes are SDS-resistant and only disassembled upon boiling (Hayashi et al., 1994). The SNARE complex assembly is shown in Figure 4.1.

4.2.5 Preparation of liposomes by extrusion

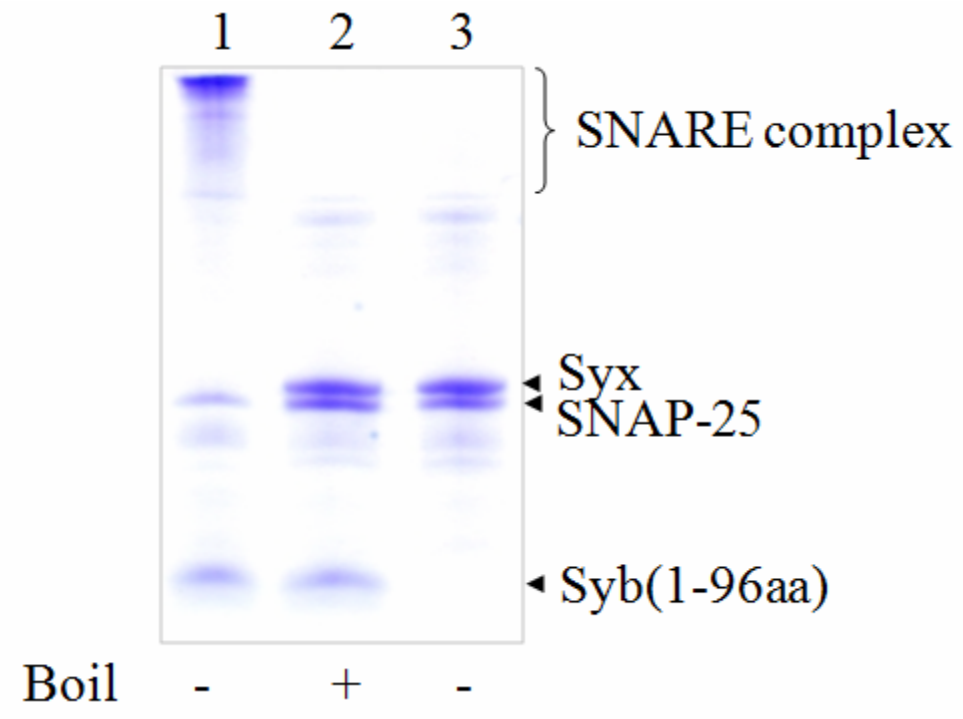

Figure 4.1 SNARE complex assembly

SDS-PAGE and Coomassie blue staining of the assembled SNARE complex. Lane 1 shows the assembled ternary SNARE complex composed of full length syntaxin 1A, full length SNAP-25 and synaptobrevin cytoplasmic fragment before boiling. Lane 2 shows the assembled ternary SNARE complex after boiling. Lane 3 shows the assembled t-SNARE complex composed of full length syntaxin 1A and SNAP-25. The SNARE proteins are indicated by arrows.

15% (w/w) 1, 2-dioleoyl phosphatidylserine (DOPS) (Avanti Polar Lipids, Alabaster, AL, USA) and 85% (w/w) 1-palmitoyl, 2-oleoyl phosphatidylcholine (POPC) (Avanti Polar Lipids, Alabaster, AL, USA) were mixed in chloroform in a glass tube. The chloroform in the lipid mixture was evaporated under a nitrogen gas stream in the hood to allow the formation of a thin lipid film on the bottom of the glass tube, which was then thoroughly dried with a vacuum pump for overnight to completely remove residual chloroform. The dried lipid film was then hydrated by adding proper amount of reconstitution buffer (25 mM HEPES, pH 7.4, 100 mM KCl, 0.1 mM EGTA, 1 mM freshly added DTT) to give a final lipid concentration of 15 mM. The hydrated lipid was vigorously vortexed for at least five minutes to form large multilamellar vesicles (LMV). To prevent the membranes from fouling and improve the homogeneity of the size distribution of the final liposome suspension, the LMV suspension was disrupted by five times freeze/thaw cycles in liquid nitrogen. Mini-extruder (Avanti Polar Lipids, Alabaster, AL, USA) was used to homogenize the lipids. The mini-extruder is a system of two gas-tight syringes with a polycarbonate filter in the middle and assembled according to the procedures recommended by the manufacturer. After the initial pass through the polycarbonate filter, the particle size distribution will tend towards a bimodal distribution. Finally, after sufficient passes through the polycarbonate filter, a unimodal, normal distribution will be obtained. The lipid suspension was forced through a polycarbonate filter with 80 nm pore size for at least twenty-one times. This procedure typically yields large unilamellar vesicles (LUV) of homogeneous size with a mean diameter of 100 nm as measured by dynamic light scattering (DLS). The liposomes were stored at 4 ºC and used within 1-3 days.

4.2.6 Reconstitution of the SNARE complex into the preformed liposomes

Two major detergent mediated reconstitution methods are commonly used in the literature, the direct method and the comicellization method. The direct method is based on manipulation of pre-formed liposomes (Rigaud et al., 1995; Rigaud and Levy, 2003). The pre-formed liposomes were saturated, but not solublized with detergents by controlling the amount of detergents used. The liposomes are then mixed with membrane proteins in detergents to allow their insertion into the liposomes. Removal of detergent by dilution to a concentration below its critical micelle concentration (CMC), dialysis and absorption of polystyrene beads will lead to the formation of reconstituted proteolipsome. In contrast, the comicellization method involves the mixing of dried lipids and membrane proteins in detergents and subsequent removal of detergents by dilution, dialysis and absorption of polystyrene beads, without the involvement of pre-formed liposomes (Weber et al., 1998). The proteoliposomes generated with the direct method usually exhibit more homogeneous size distribution and protein insertion compared to those with the comicellization method (Chen et al., 2006). In my studies, the direct reconstitution method was used due to the aforementioned advantages.

In a typical reconstitution experiment, 100 μl of the preformed liposomes at 15mM lipid concentration were mixed with 200 μl of the preassembled SNARE complex with syntaxin 1A transmembrane region in 1% (w/v) β-OG at room temperature. In this way, the

final concentrations of lipid and β-OG in the mixture were 5 mM and 0.66% (w/v), respectively. Such reconstitution conditions were chosen based on previous systematic studies of β-OG mediated membrane protein reconstitution (Rigaud et al., 1995). For preparation of the SNARE-incorporated proteoliposomes, the typical protein to lipid molar ratio used was 1:500. The mixture was kept at room temperature for 30 minutes under gentle stirring to allow the SNARE complex to insert into the liposomes via syntaxin 1A transmembrane region. Then the detergent β-OG was removed by a three-step extensive dialysis against reconstitution buffer (25 mM HEPES, pH 7.4, 100 mM KCl, 0.1 mM EGTA, and 1 mM freshly added DTT). First, the mixture was dialyzed against 1 liter reconstitution buffer containing 1 g Biobeads SM2 polystyrene beads (Bio-Rad Laboratories) at room temperature for one hour. Next, the dialysis was continued against 1 liter fresh reconstitution buffer containing 1 g Biobeads at room temperature for two more hours. Finally, the sample was transferred to 2 liter fresh reconstitution buffer containing 2 g Biobeads and dialyzed at 4 ºC overnight.

4.2.7 Cofloatation assays

The mixture of recombinant proteins and 75μL reconstituted proteoliposomes was diluted to 180μL and incubated at 4 °C for 1 hour. The samples were then mixed with equal volume of 80% (w/v) Nycodenz (Sigma) and placed on the bottom of 5 x 41 mm ultracentrifuge tubes. The proteoliposomes were overlaid with 150 μL 35% (w/v) Nycodenz and 150 μL 30% (w/v) Nycodenz. A 15 μL reconstitution buffer was placed on the top of the

density gradient. The samples were centrifuged at 48,000 rpm using a SW55 rotor (Beckman) for 4 hours at 4 °C. After the ultracentrifugation, the top 150μL samples were analyzed by SDS-PAGE.

4.2.8 ^{13}C-edited 1D NMR experiments

The first increment of a gradient-enhanced ^{1}H-^{13}C HSQC spectrum was acquired to obtain the 1D ^{13}C-edited ^{1}H NMR spectra with both ni2 (number of t1 increments in the ^{13}C dimension) and phase set to 1. The 1D ^{13}C-edited ^{1}H NMR spectra were acquired at 27 °C on Varian INOVA500 or INOVA600 spectrometers (Varian, Palo Alto, California, USA) with Munc13-1 MUN domain and SNARE liposome samples dissolved in 20 mM Tris, pH 8.0, 150 mM NaCl, using H_2O/D_2O 95:5 (v/v) as the solvent. The 5% (v/v) D_2O was included to provide the lock signal for the control of the long-term stability of the magnetic field.

4.2.9 Size exclusion chromatographic binding assay

Size exclusion chromatographic binding assay was performed with a Superdex S200 10/300 GL column (GE healthcare life sciences) on an ÄKTA FPLC^{TM} protein purification system (GE healthcare life sciences). 500 μL sample was injected into a sample loop of 500 μL volume and eluted with binding assay buffer through the size exclusion column. The final concentrations of the injection samples were usually 5 to 10 μM. The typical binding assay buffer contains 20 mM Tris, pH 8.0, 150 mM NaCl, and 1 mM freshly added DTT. Binding

reactions were usually incubated for two hours at 4 ºC in the cold room before injection into the FPLC system.

4.3 Results

4.3.1 Binding studies of the Munc13-1 MUN domain, Munc18-1, and soluble SNARE complex in aqueous solution by size exclusion chromatographic binding assays

More and more evidence has supported the notion that SNAREs and Munc18-1 might form the minimal fusion machinery (Rizo et al., 2006; Dulubova et al., 2007; Shen et al., 2007). Interestingly, previous studies from our laboratory have suggested that Munc18-1 can bind to the assembled SNARE complex containing the syntaxin 1A N-terminal H_{abc} domain besides to the closed conformation of syntaxin 1A (Dulubova et al., 2007; Dulubova et al., 1999). Together with the fact that the Munc13-1 MUN domain has been suggested to be intimately connected to syntaxin 1A and Munc18-1 by various genetic and biochemical studies, this observation motivated us to test the possibility of the Munc18-1/SNARE complex as the target of the Munc13-1 MUN domain. On one hand, the MUN domain might bind to the Munc18-1/SNARE complex. On the other hand, the MUN domain might disrupt the interaction between Munc18-1 and SNARE complex. To test these possibilities, I performed a size exclusion chromatographic binding assay to study the interactions among the MUN domain, Munc18-1 and soluble SNARE complex in solution. Munc18-1 and the SNARE complex reproducibly form a binary complex in the size exclusion chromatographic

binding assay, which can be observed as the significantly decreased intensity of Munc18-1 peak as well as a left-shift of the retention volume corresponding to the complex formation (Figure 4.2A). Consistent with the ^{13}C-edited 1D NMR experiments and ITC data in chapter 3, I could not detect any interaction between the MUN domain and Munc18-1 in the size exclusion chromatographic binding assay (Figure 4.2B). Similarly, no interaction between the MUN domain and the SNARE complex could be detected (Figure 4.2C). When equimolar amounts of Munc18-1, MUN domain and SNARE complex were mixed together and loaded onto a Superdex S200 10/300 GL size exclusion column, the size exclusion chromatogram of the Munc18-1/MUN/SNARE complex mixture is equivalent to the computational summation of the chromatogram of the MUN domain alone and that of Munc18-1/SNARE complex alone, indicating that the MUN domain neither interacts with the Munc18-1/SNARE complex nor disrupts the interaction between Munc18-1 and the SNARE complex (Figure 4.2D).

4.3.2 Binding studies of the Munc13-1 MUN domain, Munc18-1, and reconstituted SNAREs by size exclusion chromatographic binding assays

Since native SNARE proteins are embedded in the membrane and the lipid environment can change their biochemical behavior to some extent, sometimes dramatically (Dai et al., 2007), I decided to study the interaction between the Munc13-1 MUN domain, Munc18-1 and reconstituted SNAREs (SNARE proteins or SNARE complex) in the membrane environment. To this end, I first prepared SNARE reconstituted proteoliposomes.

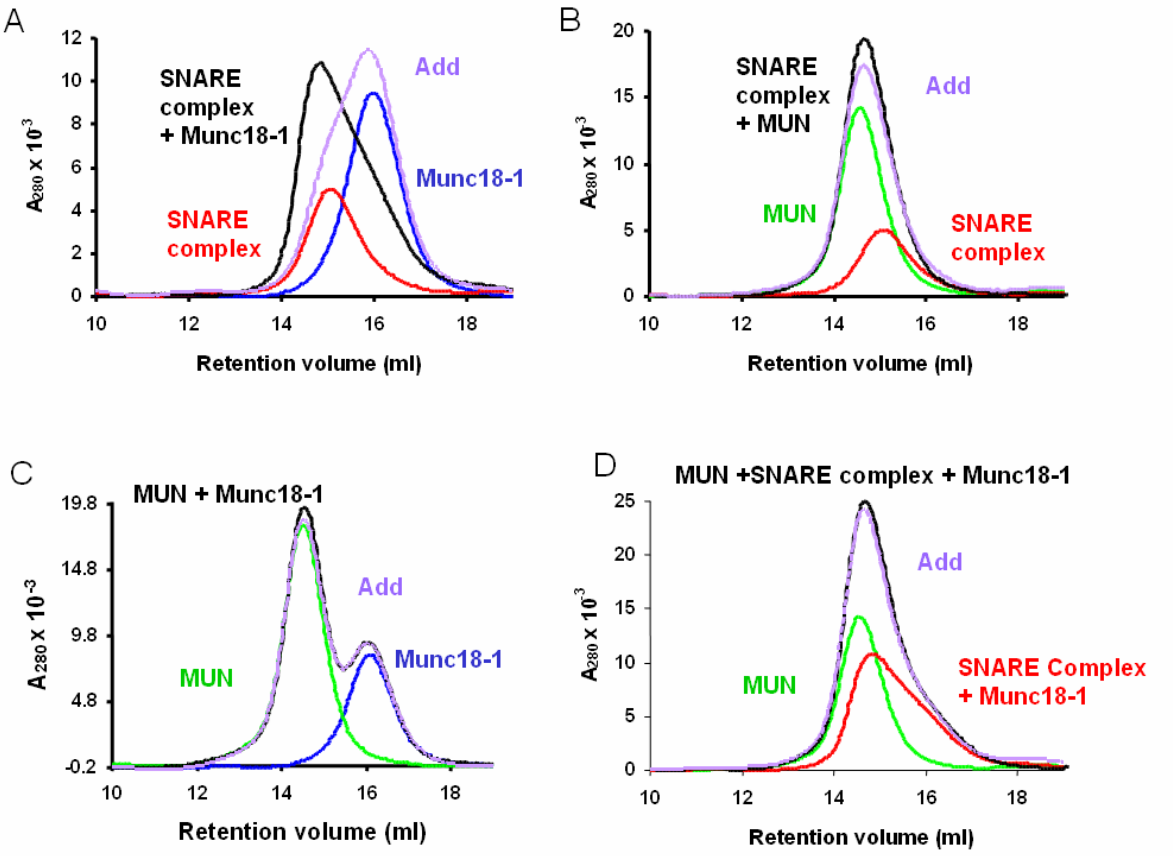
A
SNARE complex + Munc18-1
Add
Munc18-1
SNARE complex
A280 X 10-3
Retention volume (ml)
B
SNARE complex + MUN
Add
MUN
SNARE complex
A280 X 10-3
Retention volume (ml)
C
MUN + Munc18-1
Add
Munc18-1
MUN
A280 X 10-3
Retention volume (ml)
D
MUN +SNARE complex + Munc18-1
Add
MUN
SNARE Complex + Munc18-1
A280 X 10-3
Retention volume (ml)

Figure 4.2 Interaction among the MUN domain, Munc18-1, and soluble SNARE complex analyzed by size exclusion chromatographic binding assays

(A) Size exclusion chromatograms of the SNARE complex alone (red), Munc18-1 alone (blue), and the mixture of Munc18-1 and SNARE complex (black). The gray curve is the computational summation of red curve and blue curve.

(B) Size exclusion chromatograms of the MUN domain alone (green), Munc18-1 alone (blue), and the mixture of Munc18-1 and MUN domain (black). The gray curve is the computational summation of green curve and blue curve.

(C) Size exclusion chromatograms of the SNARE complex alone (red), the MUN domain alone (green), and the mixture of MUN domain and SNARE complex (black). The gray curve is the computational summation of red curve and green curve.

(D) Size exclusion chromatograms of the Munc18-1/SNARE complex alone (red), the MUN domain alone (blue), and the mixture of Munc18-1/SNARE complex and MUN domain (black). The gray curve is the computational summation of red curve and blue curve.

The ternary SNARE complex was assembled with the synaptobrevin cytoplasmic fragment (amino acids 1-96) and full length syntaxin 1A (amino acids 2-288) containing the transmembrane region coexpressed with full length SNAP-25 (Figure 4.1). Interestingly, the coexpressed full length syntaxin 1A and SNAP-25 form a 1:1 molar ratio t-SNARE complex, which is different from the previously observed 2:1 t-SNARE complex assembled from separately expressed syntaxin 1A and SNAP-25 (Xiao et al., 2001). This helped to increase the assembly efficiency of the ternary SNARE complex since it is not necessary for synaptobrevin to displace one of the syntaxin 1A molecules in the t-SNARE complex. The assembled SNARE complexes were reconstituted into preformed liposomes, which are large unilamellar vesicles (LUV) made by the extrusion method with a mean diameter of 100 nm, to form proteoliposomes using the direct method (Rigaud et al., 1995) (Figure 4.3). Briefly, preformed liposomes were softened by detergents and mixed with preassembled SNARE complex with syntaxin 1A transmembrane region in detergents. Upon incubation, the SNARE complexes were inserted into the liposomes via the syntaxin 1A transmembrane region. Extensive dialysis with Biobeads was used to remove the detergent, leading to the formation of SNARE complex proteoliposomes.

Initially, a size exclusion chromatographic binding assay was used to study the interactions between reconstituted SNARE complex in liposomes and Munc18-1 or the MUN domain, which turned out to be negative (Figure 4.4A, 4.4B). I also tested the interaction between reconstituted full length syntaxin 1A in liposomes and Munc18-1 or the MUN domain to see whether the membrane has any effects on the interactions. Both attempts

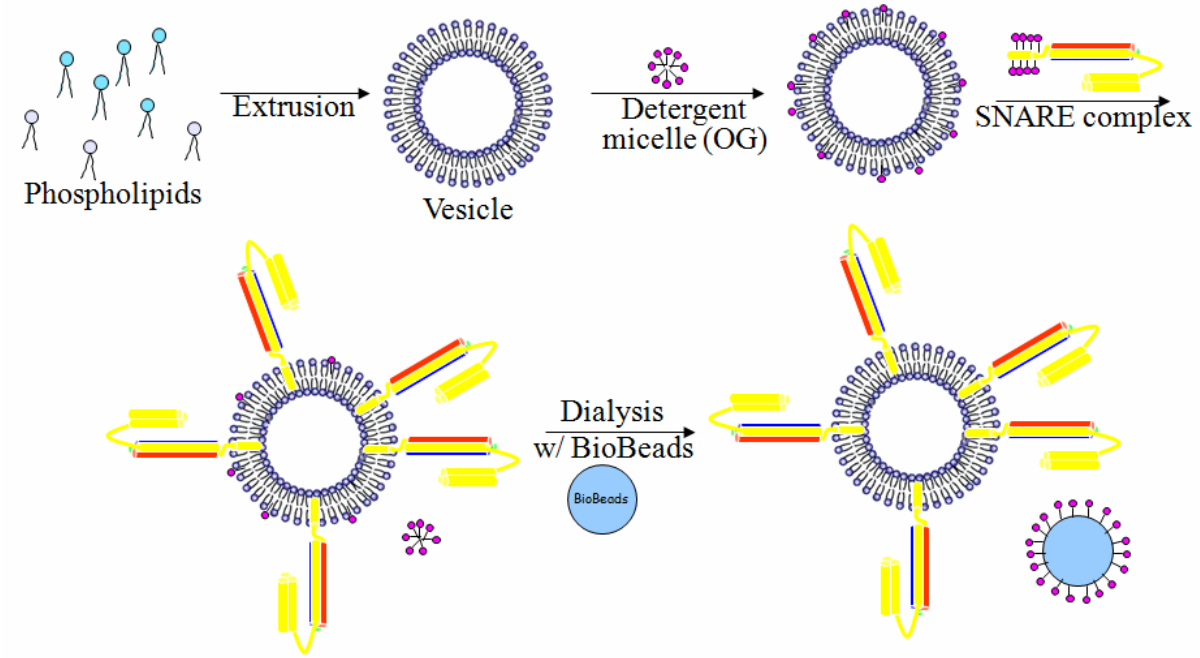

Figure 4.3 Schematic diagram of reconstitution of the SNARE complex into liposomes

The SNARE motifs of syntaxin 1A, synaptobrevin, and SNAP-25 as well as the helices of syntaxin 1A N-terminal H_{abc} domain are shown are represented as cylinders. Syntaxin and synaptobrevin are colored yellow and red, respectively. The N- and C-terminal SNARE motif of SNAP-25 are colored blue and green, respectively.

revealed no interaction (Figure 4.4C, 4.4D). Interestingly, the size exclusion chromatographic binding assay could not detect the interaction between Munc18-1 and reconstituted syntaxin 1A. In solution, Munc18-1 bind to the syntaxin 1A cytoplasmic region with an extremely high affinity in the low nanomolar range (Khvotchev et al., 2007). This result suggested that the membrane environment strongly weakened the syntaxin 1A/Munc18-1 interaction. Actually, previous studies from our laboratory have suggested that the binding affinity of complexin I to the SNARE complex is also significantly weakened when the SNARE complex is reconstituted into liposomes (Han Dai, personal communication). The potential explanation for these unexpected observations might be that the membrane embedment of the SNARE complex or syntaxin 1A alone creates some spatial restraints to prevent the easy access and efficient interaction between complexin/the SNARE complex or Munc18-1/syntaxin 1A.

4.3.3 Binding studies of the Munc13-1 MUN domain and reconstituted SNARE complex by ^{13}C-edited 1D NMR experiments

Besides the size exclusion chromatographic binding assay, I also used the ^{13}C-edited 1D NMR experiments to test the interaction between^{13}C-labeled Munc13-1 MUN domain and reconstituted SNARE complex in liposomes (Arac et al., 2003). A significant decrease in the ^{13}C-edited 1D NMR signal intensity will be observed if the MUN domain binds to the SNARE liposomes due to the large size of lipsomes. Otherwise, no significant intensity change will be observed. Similar to the size exclusion chromatographic binding assay, no

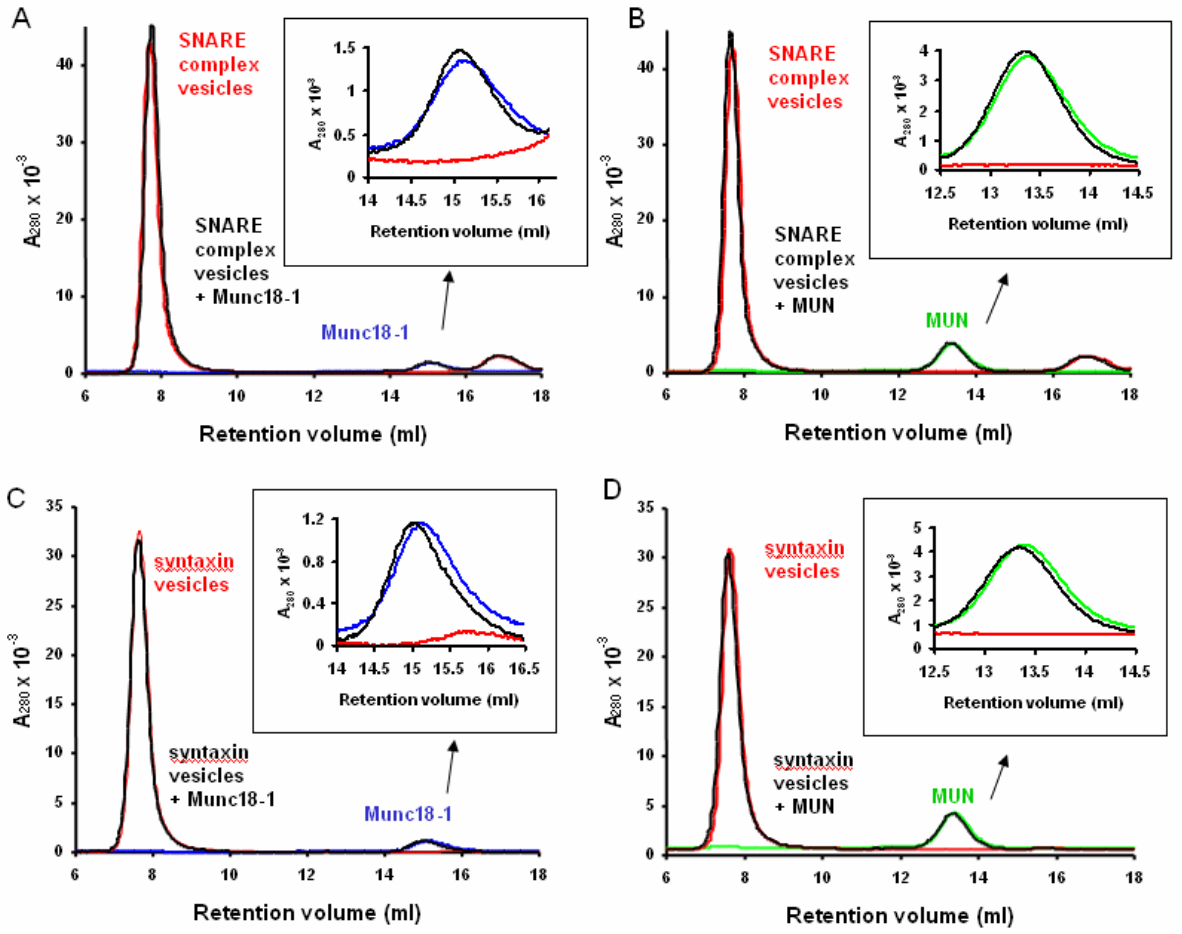
A
SNARE complex vesicles
SNARE complex vesicles + Munc18-1
Munc18-1
A280 X 10-3
Retention volume (ml)
B
SNARE complex vesicles
SNARE complex vesicles + MUN
MUN
A280 X 10-3
Retention volume (ml)
C
syntaxin vesicles
syntaxin vesicles + Munc18-1
Munc18-1
A280 X 10-3
Retention volume (ml)
D
syntaxin vesicles
syntaxin vesicles + MUN
MUN
A280 X 10-3
Retention volume (ml)

Figure 4.4 Interaction between the reconstituted SNARE complex and the MUN domain or Munc18-1 analyzed by size exclusion chromatographic binding assay

(A) Size exclusion chromatograms of the reconstituted SNARE complex alone (red), Munc18-1 alone (blue), and the mixture of Munc18-1 and reconstituted SNARE complex (black). The Munc18-1 peak region was enlarged for clarity in the inset.

(B) Size exclusion chromatograms of the reconstituted SNARE complex alone (red), the MUN domain alone (green), and the mixture of MUN domain and reconstituted SNARE complex (black). The MUN domain peak region was enlarged for clarity in the inset.

(C) Size exclusion chromatograms of the reconstituted syntaxin 1A alone (red), Munc18-1 alone (blue), and the mixture of Munc18-1 and reconstituted syntaxin 1A (black). The Munc18-1 peak region was enlarged for clarity in the inset.

(D) Size exclusion chromatograms of the reconstituted syntaxin 1A alone (red), the MUN domain alone (green), and the mixture of MUN domain and reconstituted syntaxin 1A (black). The MUN domain peak region was enlarged for clarity in the inset.

binding was detected (data not shown).

4.3.4 Binding studies of the Munc13-1 MUN domain, Munc18-1, complexin I and reconstituted SNARE complex by cofloatation assay

Since the size exclusion chromatographic binding assay causes a dilution of the samples, the relatively weak interaction might be difficult to be detected. Therefore, I also used another method to test these interactions, a cofloatation assay. The schematic diagram of the cofloatation assay was shown in Figure 4.5. Recombinant proteins were mixed with the reconstituted SNARE complex in liposomes. The mixture was placed on the bottom of a Nycodenz density gradient. Upon centrifugation, the liposomes will float up due to their low density. Proteins associated with the reconstituted SNARE complex in liposomes will thus enter the top fraction whereas non-interacting proteins will sink to the bottom fraction due to their high density. The Nycodenz density gradient was fractionated after centrifugation and the top fraction was examined by SDS-PAGE and ProtoBlue Safe colloidal Coomassie staining.

Firstly, equimolar amounts of Munc18-1, the MUN domain, complexin I and the reconstituted SNARE complex in liposomes were mixed together and subjected to Nycodenz density gradient centrifugation. The blank liposomes without reconstituted SNARE complex were used as a negative control in the cofloatation assay. Only Munc18-1 seems to exhibit a little weak association with the blank liposome (Figure 4.6). In contrast, Munc18-1, the

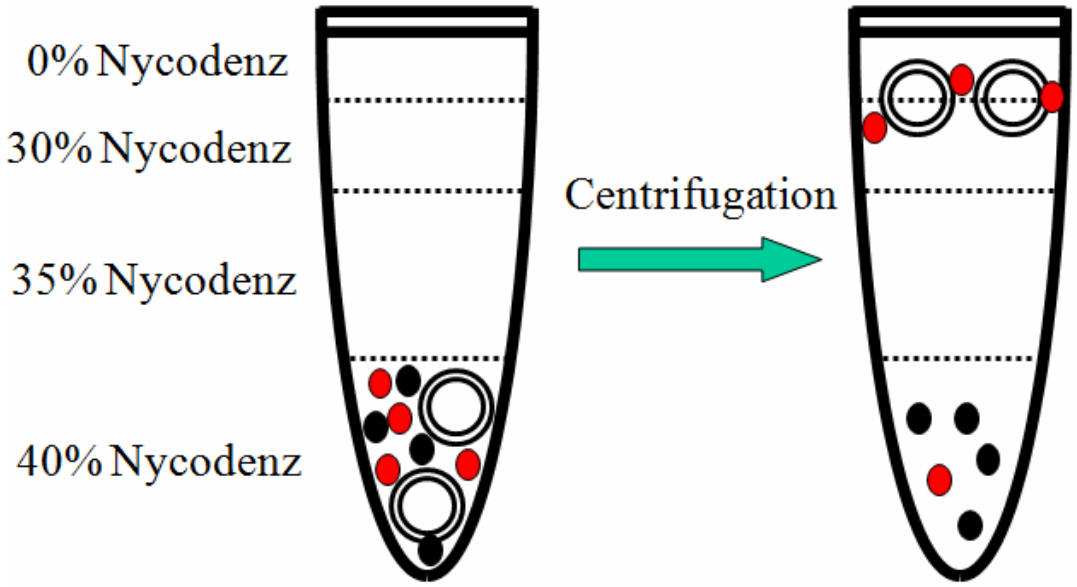

Figure 4.5 Schematic diagram of the cofloatation assay

The SNARE reconstituted liposomes are represented as the concentric spheres. The interacting and non-interacting proteins are represented as red and black ovals, respectively. The interfaces between pre-laid Nycodenz density gradient are indicated by the dotted lines.

MUN domain and complexin I are all capable of binding to the reconstituted SNARE complex in liposomes and enter the top fraction in the Nycodenz density gradient (Figure 4.6).

Although both Munc18-1 and the MUN domain can bind to the reconstituted SNARE complex, a higher amount of Munc18-1 is bound to the reconstituted SNARE complex than the MUN domain when equimolar amounts of Munc18-1 or MUN domain are incubated with reconstituted SNARE complex separately. This cannot be solely accounted for by the background binding of Munc18-1 to the blank liposome. Therefore, it seems that the affinity between Munc18-1 and the reconstituted SNARE complex is stronger than that between the MUN domain and the reconstituted SNARE complex (Figure 4.7A). Moreover, the binding of the MUN domain to the reconstituted SNARE complex is even weaker in the presence of Munc18-1, which suggested that the MUN domain and Munc18-1 might compete with each other for SNARE binding (Figure 4.7A). To better differentiate the binding of the MUN domain and Munc18-1 to the reconstituted SNARE complex, I decided to use the GST-MUN fusion protein and Munc18-1 to study the compatibility of their interactions with the reconstituted SNARE complex since the molecular weight of the MUN domain and Munc18-1 are very close. It can be clearly observed that the amount of Munc18-1 bound to the reconstituted SNARE complex gradually decreases in the presence of increasing amount of GST-MUN, which suggested that the MUN domain can compete with Munc18-1 for SNARE binding (Figure 4.7B).

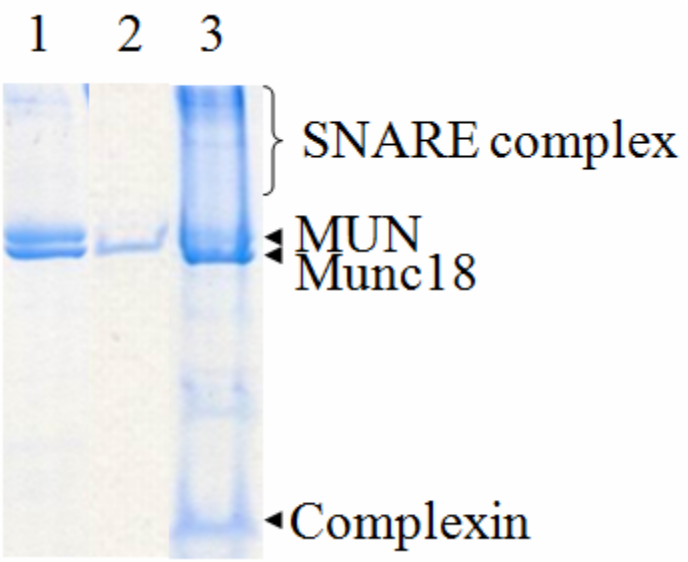

Figure 4.6 Interaction between the reconstituted SNARE complex and the MUN domain, Munc18-1 or complexin I analyzed by cofloatation assay

SDS-PAGE and ProtoBlue Safe colloidal Coomassie staining of the top fraction of the cofloatation assay. Lane 1 shows one tenth of the input. Lane 2 shows the top fraction of a mixture of Munc18-1, the MUN domain, complexin I and blank liposome. Lane 3 shows the top fraction of a mixture of Munc18-1, the MUN domain, complexin I and the reconstituted SNARE complex. Munc18-1, the MUN domain, and complexin I are indicated by arrows.

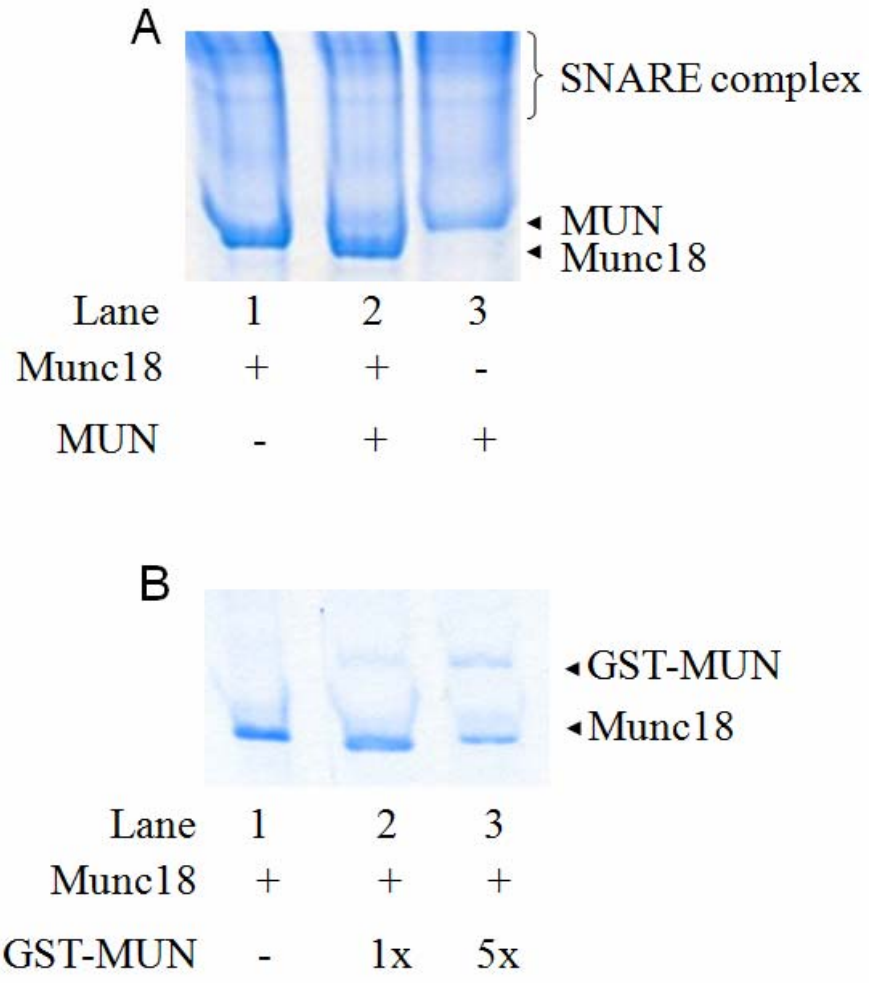

Figure 4.7 Compatibility of interaction between the reconstituted SNARE complex in liposomes and the MUN domain or Munc18-1 analyzed by cofloatation assay

(A) SDS-PAGE and ProtoBlue Safe colloidal Coomassie staining of the top fraction of a mixture of reconstituted SNARE complex with Munc18-1 or MUN domain or both. Munc18-1 and the MUN domain are indicated by arrows.

(B) SDS-PAGE and ProtoBlue Safe colloidal Coomassie staining of the top fraction of a mixture of reconstituted SNARE complex and Munc18-1 in the presence of increasing amount of GST-MUN. Munc18-1 and GST-MUN are indicated by arrows.

I also tested the SNARE-binding compatibility of Munc18-1 or the MUN domain with complexin I, a small soluble protein known to associate tightly with the SNAREcomplex in solution, using the cofloatation assay. The amount of Munc18-1 bound to the reconstituted SNARE complex gradually decreases in the presence of increasing amounts of complexin I, suggesting that complexin I can compete with Munc18-1 for SNARE binding (Figure 4.8). In contrast, no significant change of the amount of the MUN domain bound to reconstituted SNARE complex was observed when increasing amounts of complexin I is bound, suggesting that the binding of complexin I and the MUN domain to the reconstituted SNARE complex are compatible (Figure 4.9).

Besides the ternary SNARE complex, I also studied the binding of Munc18-1, the MUN domain, and complexin I to the 1:1 molar ratio syntaxin 1A/SNAP-25 t-SNARE complex reconstituted in liposomes. It seems that Munc18-1, the MUN domain, and complexin I all bind to the reconstititued t-SNARE complex and no clear competition for t-SNARE binding among them was observed (Figure 4.10).

4.4 Discussion

As expected, Munc18-1 interacts with syntaxin 1A or the soluble SNARE complex in solution. In contrast, the size exclusion chromatographic binding assay cannot detect the interaction between Munc18-1 and syntaxin 1A reconstituted in the membrane environment or the interaction between Munc18-1 and SNARE complex reconstituted in the membrane

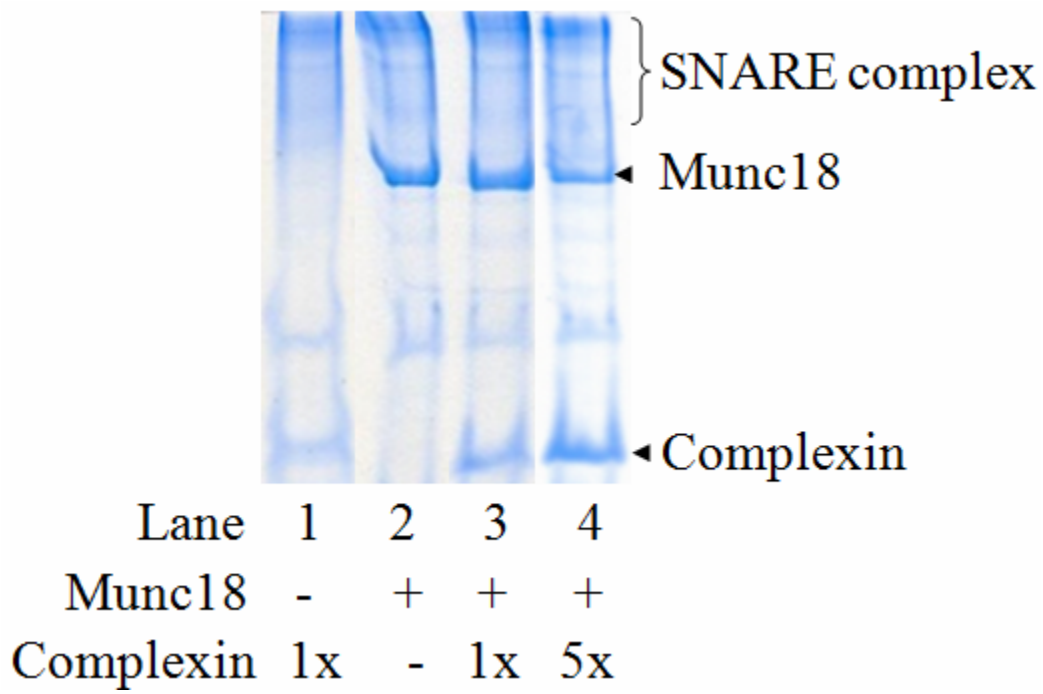

Figure 4.8 Compatibility of interaction between the reconstituted SNARE complex in liposomes and Munc18-1 or complexin I analyzed by cofloatation assay

SDS-PAGE and ProtoBlue Safe colloidal Coomassie staining of the top fraction of a mixture of reconstituted SNARE complex and Munc18-1 in the presence of increasing amount of complexin I. Munc18-1 and complexin I are indicated by arrows.

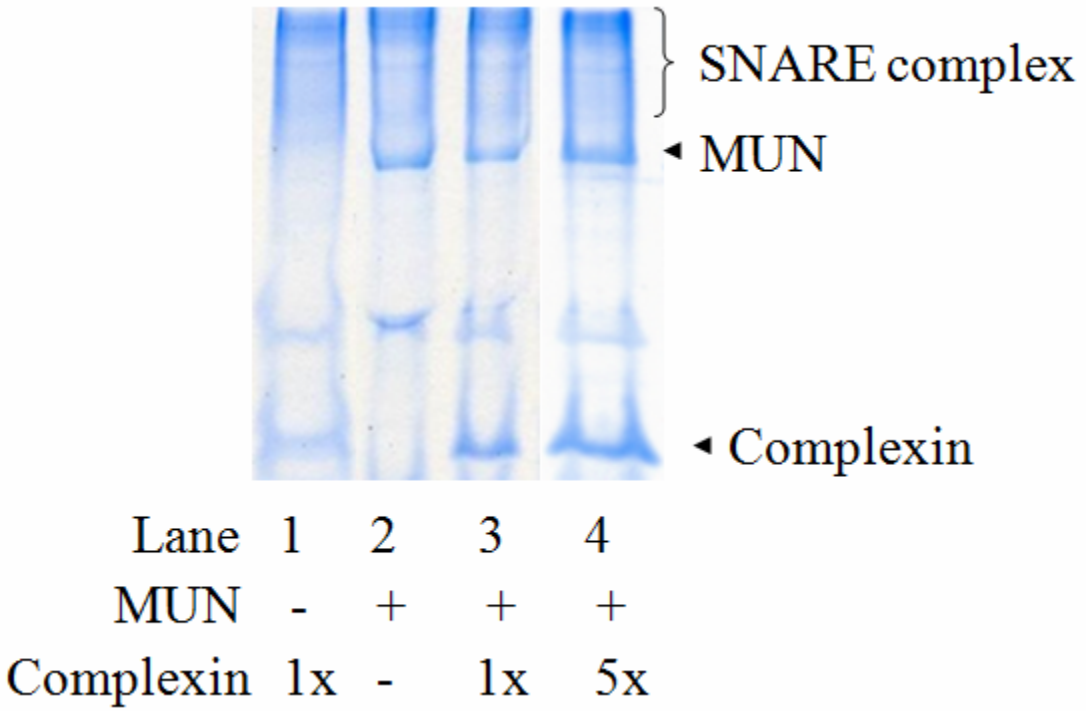

Figure 4.9 Compatibility of interaction between the reconstituted SNARE complex in liposomes and the MUN domain or complexin I analyzed by cofloatation assay

SDS-PAGE and ProtoBlue Safe colloidal Coomassie staining of the top fraction of a mixture of reconstituted SNARE complex and MUN domain in the presence of increasing amount of complexin I. The MUN domain and complexin I are indicated by arrows.

A

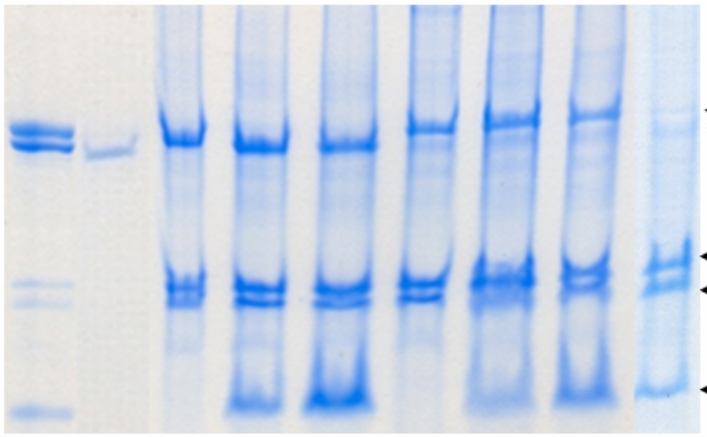

Lane	1	2	3	4	5	6	7	8	9
Munc18	+	+	+	+	+	-	-	-	-
MUN	+	+	-	-	-	+	+	+	-
Complexin	1x	1x	-	1x	5x	-	1x	5x	1x

B

Lane	1	2	3
Munc18	+	+	+
GST-MUN	-	1x	5x

Figure 4.10 Interaction between the reconstituted t-SNARE complex in liposomes and the MUN domain, Munc18-1 or complexin I analyzed by cofloatation assay

(A) SDS-PAGE and ProtoBlue Safe colloidal Coomassie staining of the top fraction of the cofloatation assay. Lane 1 shows one tenth of the input. Lane 2 shows the top fraction of a mixture of Munc18-1, the MUN domain, complexin I and blank liposome. Lane 3-5 show the top fractions of a mixture of reconstituted t-SNARE complex and Munc18-1 in the presence of increasing amount of complexin I. Lane 6-8 show the top fractions of a mixture of reconstituted t-SNARE complex and MUN domain in the presence of increasing amount of complexin I. Lane 9 shows the top fractions of a mixture of reconstituted t-SNARE complex and complexin I. Syntaxin, SNAP-25, Munc18-1, the MUN domain, and complexin I are indicated by arrows.

(B) SDS-PAGE and ProtoBlue Safe colloidal Coomassie staining of the top fraction of a mixture of reconstituted t-SNARE complex and Munc18-1 in the presence of increasing amount of GST-MUN. Syntaxin, SNAP-25, Munc18-1 and GST-MUN are indicated by arrows.

environment. However, the interaction between Munc18-1 and the reconstituted SNARE complex can be detected using a more sensitive cofloatation method. Likewise, the size exclusion chromatographic binding assay cannot detect the interaction between the MUN domain and SNARE complex, both in solution and in the membrane environment. However, cofloatation assays can detect the interaction between the MUN domain and reconstituted SNARE complex in liposomes as well as the interaction between the MUN domain and reconstituted t-SNARE complex in liposomes. As far as complexin I is concerned, the interaction between complexin I and SNARE complex can be detected both in solution and in the membrane environment. Intriguingly, both complexin I and the MUN domain can compete with Munc18-1 for SNARE complex binding whereas the binding of complexin I and the MUN domain are compatible. Our results suggest the potential existence of a ternary MUN/complexin/SNARE complex in the membrane environment, which might play a critical role in the regulation of neurotransmitter release. Interestingly, the competition and comparability of interactions with reconstituted SNARE complex among Munc18-1, MUN and complexin share a similar scheme with the previously reported Ca^{2+}-induced switch of synaptotagmin/complexin binding to reconstituted SNARE complex (Tang et al., 2006; Dai et al., 2007), suggesting that a series of exquisitely regulated sequential association and dissociation events underlie the precise temporal and spatial regulation of Ca^{2+}-triggered neurotransmitter release. Our studies also suggest that the membrane environment can modulate the strength of protein-protein interactions remarkably, which emphasize the importance to include membranes in the studies of protein-protein interactions among proteins involved in neurotransmitter release.

Chapter 5 Crystal Structure of the rat RIM1 C_2B Domain at 1.7 Å

5.1 Introduction

Neurotransmitter release is a central event for interneuronal communication. This process is achieved through exocytosis of synaptic vesicles at the presynaptic plasma membrane and involves several steps that include docking of synaptic vesicles at specialized sites of the plasma membrane called active zones, one or more priming reactions that leave the vesicles ready for release, and the actual release of neurotransmitters triggered by Ca^{2+} influx when an action potential reaches the presynaptic axon terminal (Sudhof, 2004). These different steps are governed by a complex protein machinery that shares several components with most other types of intracellular membrane trafficking. These components include, among others, the SNARE proteins synaptobrevin, syntaxin and SNAP-25, which are critical for membrane fusion, and Rab3s, which are small GTPases from the Rab family that regulate neurotransmitter release (Jahn and Scheller, 2006; Rizo et al., 2006; Sudhof, 2004). In addition, neurotransmitter release is controlled by proteins with specialized roles such as the Ca^{2+} sensor synaptotagmin 1 and the components of the active zone such as the key priming factors RIMs, Munc13s and so on (Rizo et al., 2006; Bai and Chapman, 2004).

Presynaptic active zones are composed of a network of large proteins that include RIMs, Munc13s, liprins, Bassoon, piccolo/aczonin, and ELKS and integrate presynaptic signals that regulate neurotransmitter release (Garner et al., 2000; Rosenmund et al., 2003).

Among these proteins, RIMs are particularly interesting because they exhibit multiple interactions that are believed to organize the active zone, and because they play multiple roles in regulating neurotransmitter release and presynaptic plasticity processes that mediate some forms of information processing in the brain (Kaeser and Sudhof, 2005). RIM1α was initially identified as a large Rab3 effector that contains an N-terminal zinc finger (ZF) domain, a central PDZ domain, and two C-terminal C_2 domains (referred to as the C_2A and C_2B domains) (Wang et al., 1997) (Figure 5.1A). Three additional RIM genes were later identified in mammals (*RIM2*, *RIM3γ* and *RIM4γ*) (Wang et al., 2000; Wang and Sudhof, 2003), and one RIM homologue was found in *C. elegans*, which is encoded by *unc10*, a gene first identified in the classic uncoordination mutant screen (Koushika et al., 2001; Brenner, 1974). *RIM2* specifies a full-length transcript, RIM2α, with an analogous domain structure to that of RIM1α, a slightly shorter transcript that lacks the N-terminal ZF domain (RIM2β), and a much shorter transcript (RIM2γ) that only contains the C_2B domain and adjacent sequences, similarly to RIM3γ and RIM4γ (Figure 5.1A). Genetic ablation of *unc10* in *C. elegans* (Koushika et al., 2001) or of RIM1α and RIM2α in mice (Schoch et al., 2006) led to a severe impairment in neurotransmitter release associated with a defect in synaptic vesicle priming. A milder phenotype was observed in RIM1α knockout mice (Schoch et al., 2002), indicating a partial functional redundancy of RIM1α and RIM2α. However, defects in short- and long-term presynaptic plasticity, as well as in memory and learning, are observed in the absence of RIM1α (Schoch et al., 2002; Castillo et al., 2002; Lonart et al., 2003; Calakos et al., 2004; Powell et al., 2004), demonstrating the critical importance of this protein for brain function.

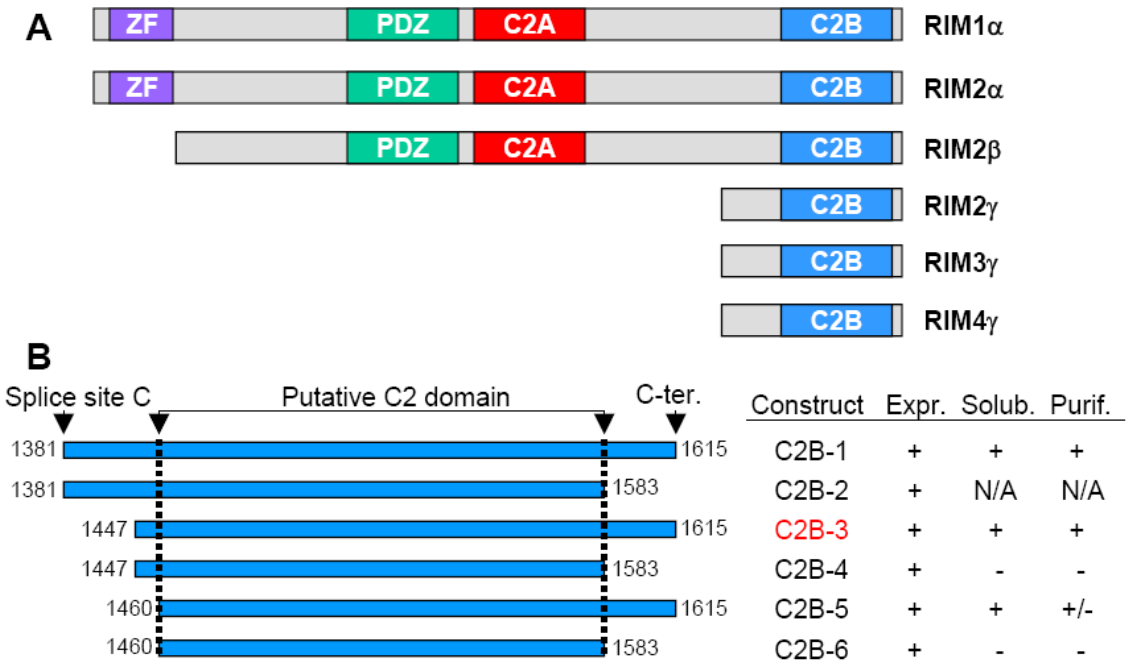

Figure 5.1 Definition of the RIM1α C_2B domain boundaries

(A) Domain diagrams of the different RIM proteins identified in mammals.

(B) Summary of the RIM1α fragments prepared to identify the boundaries of the RIM1α C_2B domain. On the left, bar diagrams illustrate the lengths of the different fragments, and the residue numbers of their N- and C-termini are indicated. Residues 1381 and 1615 correspond to the boundary of a splice site [splice site C] and to the C-terminus of RIM1α, respectively. The name assigned to the fragments, as well as their expression level, solubility and feasibility of purification, are qualitatively indicated on the right (N/A = not attempted).

The proposed role of RIMs in organizing active zones emerged from the observation of diverse interactions involving their different domains (Schoch et al., 2002). The N-terminal region of α-RIMs including the ZF domain and adjacent sequences binds to Rab3 (Wang et al., 1997) and to Munc13-1 (Betz et al., 2001), a large active zone protein with a critical role in synaptic vesicle priming (Augustin et al., 1999; Varoqueaux et al., 2002) that is executed by its MUN domain (Basu et al., 2005). Munc13-1 forms a homodimer through its N-terminal C_2A domain (Lu et al., 2006), which is also involved in binding to the α-RIM N-terminus (Betz et al., 2001) to yield a tripartite complex with Rab3 (Dulubova et al., 2005). Based on these results, it has been suggested that a Munc13-1 homodimer to Munc13-1/α-RIM heterodimer switch may regulate synaptic vesicle priming and couple priming to some forms of presynaptic plasticity (Dulubova et al., 2005; Lu et al., 2006). Additional protein-protein interactions of α-RIMs include those of a proline-rich sequence between the two C_2 domains with the SH3 domain of RIM-binding proteins (RIM-BPs) (Wang et al., 2000), and of its PDZ domain with the C-terminal tail of ELKS (Wang et al., 2002), which provides an indirect link to the active zone proteins Piccolo and Bassoon (Takao-Rikitsu et al., 2004). The RIM C_2A domain was suggested to bind to SNAP-25 and synaptotagmin 1 (Coppola et al., 2001), although these interactions could not be confirmed in separate studies (Schoch et al., 2002; Dai et al., 2005). Finally, the RIM C_2B domain has been reported to bind to liprins, which also form part of the active zone, and also to synaptotagmin 1 (Coppola et al., 2001; Schoch et al., 2002).

While until recently there was little information on the structure and interactions of RIM and Munc13 domains, NMR and X-ray studies have uncovered in the last two years the structures of the RIM ZF domain (Dulubova et al., 2005) and C_2A domain (Dai et al., 2005), the Munc13-1 C_2A domain homodimer (Lu et al., 2006) and C_1 domain (Shen et al., 2005), the RIM ZF/Munc13-1 C_2A domain heterodimer (Lu et al., 2006), and the RIM PDZ domain bound to an ELKS peptide (Lu et al., 2005). However, no detailed information is available on the structure and interactions of the RIM C_2B domain. Both the high evolutionary sequence conservation of the C_2B domain (Wang and Sudhof, 2003) and its presence in all RIM isoforms (Figure 5.1) suggest that this domain is critical for RIM function, which was supported by the finding that an Unc10 mutant lacking the C_2B domain is unable to rescue unc10 function in *C. elegans* (Koushika et al., 2001). C_2 domains are widespread protein modules whose most common properties are Ca^{2+} and phospholipid binding (Rizo and Sudhof, 1998). These properties have been extensively studied in archetypical C_2 domains such as those of synaptotagmin 1, which bind multiple Ca^{2+} ions through five conserved aspartate residues (Shao et al., 1996; Ubach et al., 1998; Fernandez et al., 2001). However, the RIM C_2B domain is only distantly related to these C_2 domains (Dai et al., 2005) and does not contain a full complement of aspartate Ca^{2+} ligands. Hence, the RIM C_2B domain is unlikely to bind Ca^{2+}, although this prediction has not been tested, and it is unclear whether this domain contains unusual structural features that may underlie a unique mechanism of action.

To shed light on these questions and provide a structural basis to understand the

function of the RIM1α C_2B domain, we have analyzed its three-dimensional structure and interactions by NMR spectroscopy and X-ray crystallography. We find that N- and C-terminal extensions beyond the canonical C_2 domain sequence are required to form the complete, folded C_2B domain of RIM1α. We also find that the RIM1α C_2B domain does not bind Ca^{2+} and is not sufficient to bind to the synaptotagmin 1 C_2 domains or to liprins, but forms a dimer in solution. The crystal structure of the RIM1α C_2B domain using diffraction data to 1.7 Å reveals a β-sandwich structure that is similar to those of other C_2 domains but includes in addition a subdomain formed by the N- and C-terminal extensions, which pack against one side of the β-sandwich and mediate dimerization. Our results suggest a model whereby one of the functions of the RIM C_2B domain may entail dimerization to facilitate the Munc13-1 C_2A domain homodimer to Munc13-1/α-RIM heterodimer switch that likely regulates synaptic vesicle priming.

5.2 Materials and methods

5.2.1 Recombinant protein preparation

DNA plasmids encoding GST fusion proteins of diverse fragments of rat RIM1α spanning the C_2B domain (Figure 5.1B) were made using custom-designed primers and standard PCR cloning techniques, and subcloned into the pGEX-KT expression vector (Hakes and Dixon, 1992). The fusion proteins were expressed at 23°C in *Escherichia coli* BL21, isolated by affinity chromatography on glutathione-sepharose followed by on-resin

cleavage with thrombin. The eluted proteins were further purified by gel filtration chromatography on a Superdex 75 Hiload 16/60 column (GE healthcare life sciences). The purity of the preparation was assessed by SDS-PAGE and Coomassie blue staining. The typical yield according to the UV measurement at 280 nm was 5-7 mg per liter of culture. Uniform ^{15}N- labeling was achieved by growing the bacteria in $^{15}NH_4Cl$ as the sole nitrogen sources. The seleno-methionine derivative of rat RIM1α C_2B domain was purified similarly.

Fragments corresponding to the rat synaptotagmin 1 C_2A domain (residues 140-267), C_2B domain (residues 271-421), and C_2AB domains (residues 140-421) as well as a rat α-liprin3 fragment spanning the minimal RIM-binding region (residues 183-470) were expressed and purified as described previously. The expression and purification procedures of rat RIM2 C2A domain wild type and R805H mutant were similar to those for synaptotagmin C2 domains described in chapter 2.

5.2.2 NMR spectroscopy

All 2D ^{1}H-^{15}N HSQC spectra were acquired at 27 °C on Varian INOVA500 or INOVA600 spectrometers (Varian, Palo Alto, California, USA) with 80-100 μM C_2 domain samples dissolved in 20 mM MES (pH 6.0), 150 mM NaCl, 1 mM EDTA and 0.5 mM TCEP, using H_2O/D_2O 95:5 (v/v) as the solvent. The 5% (v/v) D_2O was included to provide the lock signal for the feedback control of the long-term stability of the magnetic field. All

the NMR protein-protein interaction experiments were carried out at 27 ºC on Varian INOVA500 or INOVA600 spectrometers with samples containing 60 μM ^{15}N-labeled proteins and 80 μM nonlabeled proteins dissolved in 20 mM MES (pH 6.0), 150 mM NaCl, 1 mM EDTA and 0.5 mM TCEP, in the presence or absence of 10 mM $CaCl_2$, using H_2O/D_2O 95:5 (v/v) as the solvent. All NMR data were processed with the program NMRPipe (Delaglio et al., 1995) and analyzed with the program NMRView (Johnson and Blevins, 1994).

The 1D ^{1}H NMR spectra were acquired at variable RIM1α C_2B domain concentrations (12 μM to 1.22 mM) using water presaturation. The 1D ^{15}N-edited ^{1}H NMR experiments to test for lipid binding were performed with 5 μM RIM1α C_2B domain by acquiring the first trace of a ^{1}H-^{15}N HSQC spectrum.

Ca^{2+} titrations monitored by ^{1}H-^{15}N HSQC spectra were performed as described (Ubach et al., 1998). Briefly, the zero Ca^{2+} sample was assured by the addition of 1 mM EDTA. The titration was done by adding to the sample a series of certain volume of high concentration $CaCl_2$ stock. The high concentration $CaCl_2$ stock was added on the top or the side of the eppendorf tube containing the sample and then mixed quickly and thoroughly. This strategy instead of directly adding $CaCl_2$ to protein sample was used to avoid the protein precipitation caused by the very high local Ca^{2+} concentration at the spot of Ca^{2+} addition. Since upon chelating Ca^{2+}, proton will be released from EDTA, the pH value of each titration sample was measured and adjusted to maintain the pH value constant. Appropriate

concentrations for the further titration were estimated based on the already accomplished part of the titration. For rat RIM1α C_2B domain, the following calcium concentrations were used: 0 mM, 0.2 mM, 1 mM, 5 mM, 10 mM, 20 mM, 40 mM, and 80 mM Ca^{2+}.

5.2.3 X-ray crystallography

Rat RIM1α C_2B domain dissolved in 20 mM MES (pH 6.0), 150 mM NaCl, 1 mM EDTA and 0.5 mM TCEP was concentrated to 19 mg/mL for crystallization using the hanging drop vapor diffusion method. Drops in a ratio of 1 µl protein to 1 µl well solution were equilibrated versus 0.1 M sodium citrate (pH 4.1), 1.55 M $(NH_4)_2SO_4$ at 20°C. Crystals appeared overnight and grew to a final size of 0.05 x 0.05 x 0.05 mm within two days. Prior to data collection, crystals were transferred into a solution of 0.1 M sodium citrate (pH 4.1), 0.15 M NaCl, 1.7 M $(NH_4)_2SO_4$, and 20% (v/v) ethylene glycol, and then flash cooled in liquid propane. Selenomethionine-derivatized (SeMet) crystals were grown and cryoprotected via a similar procedure to wild type, and equilibrated versus 0.1 M Sodium Citrate (pH 3.5), 1.75 M $(NH_4)_2SO_4$ and cryoprotected in a solution of 0.1 M Sodium Citrate (pH 3.5), 0.15 M NaCl, 1.9 M $(NH_4)_2SO_4$, and 20% ethylene glycol. Diffraction data were collected at the Structural Biology Center beamline 19BM of the Advanced Photon Source (Argonne National Laboratory, Argonne, Illinois, USA) at 100K to a Bragg spacing (d_{min}) of 1.73 Å. The crystals exhibited the symmetry of space group $P3_121$ with unit cell parameters of a = b = 62.0 Å, c = 145.2 Å, and contained two molecules per asymmetric unit. Data were processed and scaled in the HKL2000 program suite (Otwinowski and Minor, 1997).

Initially, molecular replacement was attempted using modified rat synaptotagmin 1 C_2B domain, RIM2 C_2A domain, etc as the search model, but failed to generate a reasonable solution. The rat RIM1α C_2B domain structure was determined with experimental phases obtained from a single-wavelength anomalous dispersion (SAD) using X-rays with energy near the selenium K absorption edge. Using data to 1.73 Å, 9 of 10 possible selenium sites were located using the program *SHELXD* (Schneider and Sheldrick, 2002) and refined with the program *MLPHARE* (Otwinowski, 1991), resulting in a figure of merit of 0.348. Phases were improved by density modification in the program *DM* (Cowtan and Main, 1998), resulting in a final overall figure of merit of 0.828 in the last resolution shell (1.78-1.73 Å). Refinement of the model was carried out with the program Refmac5 (Murshudov et al., 1997) of the CCP4 package (Bailey, 1994). Manual adjustments to the model were carried out with the programs O (Jones et al., 1991) and Coot (Emsley and Cowtan, 2004). The electron density map clearly showed the presence of seven sulfate ions. After refinement of the protein part was complete, solvent molecules were added where stereochemically reasonable. The model has good stereochemistry, with 88.0% of residues in the most favored region of the Ramachandran plot and none in disallowed regions. Data collection and refinement statistics are listed in Table 5.1.

5.2.4 Analytical ultracentrifugation

Sedimentation equilibrium experiments were performed with a Beckman Optima XL-I analytical ultracentrifuge using a 4-position An60Ti rotor and an absorbance optical system

(Beckman Instruments, Fullerton, California, USA). Each cell has a six-channel carbon-Epon centerpiece with two quartz windows giving an optical path length of 1.2 cm. The sample channels and reference channels were filled with 100 µl protein solutions and 110 µl buffer solutions, respectively. Absorbance was monitored for each cell in 0.002 cm steps at a wavelength of 280 nm. Samples were centrifuged at 20,000 rpm, 25,000 rpm, 29,000 rpm, and 35,000 rpm at 4 °C until equilibrium was reached, followed by overspeed runs at 42,000 rpm to obtain baseline values of absorbance that were used in subsequent fits. The loading concentration of RIM1α C_2B domain was 22µM in 20 mM MES (pH 6.0), 150 mM NaCl, 1 mM EDTA and 0.5mM TCEP. The partial specific volumes of RIM1α C_2B domain at 4 °C was calculated from its amino acid composition to be 0.7362 $cm^3 \cdot g^{-1}$, and the monomeric molecular mass was calculated to be 18,758.9 Da. The solvent density was calculated to be 1.007 $g \cdot ml^{-1}$ at 4 °C. Data sets were fitted to either the single ideal species model or the self-association model using Beckman Optima XL-A/XL-I data analysis software (Origin 6.03). Global analysis was applied to data sets obtained at the different rotor speeds.

5.2.5 Phospholipid binding by fluorescence resonance energy transfer (FRET) assay

Emission fluorescence spectra were acquired on a PTI spectrometer with excitation at 285 nm with samples containing 1 M RIM1 C_2B domain and/or 0.01 mg/mL phospholipid vesicles composed of 65% phosphatidylcholine (PC), 25% phosphatidylserine (PS), and 10% dansyl-phosphatidylethanolamine (dansyl-PE), dissolved in standard buffer containing 1 mM EDTA or 1 mM $CaCl_2$.

FRET experiments were performed on a Perkin Elmer LS50B spectrofluorometer (Perkin Elmer, Uberlingen, Germany) with a 450 µl Quartz fluorometer cuvette (Nova Biotech), exciting at 280 nm and recording the emission spectra from 300 to 550 nm with 5nm excitation slit width and 5nm emission slit width. The experiments were performed at 25 ºC in 20 mM Tris, pH 7.2, 100 mM NaCl, with 0.1 mg/ml lipid (65% (w/w) POPC, 30% (w/w) DOPS, 5% (w/w) Dansyl-DOPE) concentration and 1 µM protein in the presence of either 1mM EDTA or 1mM Ca^{2+}. The fluorescence emission spectra of protein alone or liposome alone were acquired under identical conditions as references.

5.3 Results

5.3.1 Definition of domain boundaries and biochemical analysis

All C_2 domains whose three-dimensional structure has been determined are formed largely by sequences that adopt a β-sandwich with loops and sometimes α-helices emerging at the top and the bottom of the sandwich. Some C_2 domains contain extensions in their termini that provide additional structural elements [e.g. the C_2B domain of synaptotagmin 1 (Fernandez et al., 2001) or the Munc13-1 C_2A domain (Lu et al., 2006)]. To investigate the minimal sequence of RIM1α required to form a folded C_2B domain, we prepared six constructs to express RIM1α fragments spanning the predicted C_2B domain signature with or without N- and/or C-terminal extensions (C2B-1 to C2B-6; see Figure 5.1B). All these

fragments could be expressed in bacteria, but only those containing an extension to the very C-terminus of RIM1α were soluble. The presence of N-terminal extensions of different lengths did not appear to affect the solubility of these fragments, but complete deletion of the N-terminal sequence extensions led to instability and low yields during purification (C2B-5 fragment; Figure 5.1B).

Previous studies from our lab have shown that ^{1}H-^{15}N heteronuclear single quantum coherence (HSQC) spectra provide a useful tool to examine the behavior and proper folding of protein fragments, which can guide crystallization trials (Chen et al., 2002; Dai et al., 2004; Dai et al., 2005; Lu et al., 2006). Hence, we acquired ^{1}H-^{15}N HSQC spectra of the two RIM1α fragments that were soluble and could be purified in high yields (C2B-1 and C2B-3; Figure 5.1B). The ^{1}H-^{15}N HSQC spectrum of the C2B-1 fragment exhibited abundant cross-peaks in the center of the spectrum and only a few very broad cross-peaks in well-resolved regions (Figure 5.2A), which likely arise from aggregation. However, the ^{1}H-^{15}N HSQC spectrum of the C2B-3 fragment exhibited much narrower cross-peaks and excellent dispersion (Figure 5.2B), showing that this fragment is properly folded and well-behaved. These results show that the C2B-3 fragment spans the minimal sequence for proper folding, and hereafter we will refer to this fragment as the RIM1α C_2B domain.

5.3.2 Analysis of RIM1α C_2B domain interactions

^{1}H-^{15}N HSQC spectra also provide a powerful tool to analyze binding of ions to

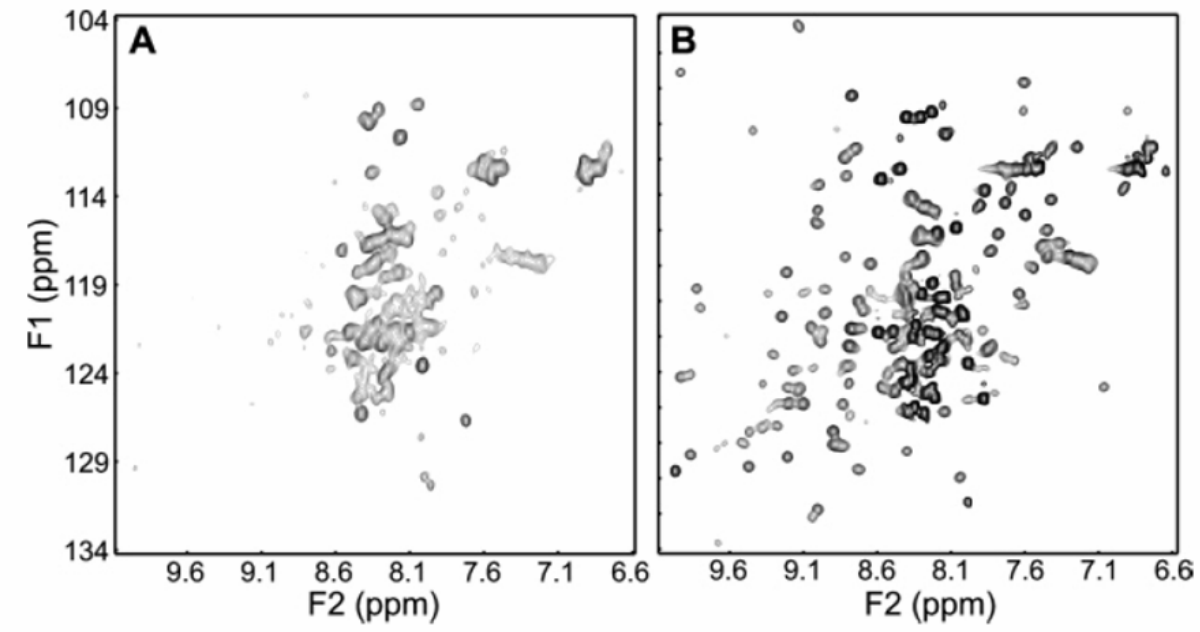

Figure 5.2 ^{1}H-^{15}N HSQC spectra of the RIM1α C2B-1 and C2B-3 fragments acquired at 600 MHz

(A) ^{1}H-^{15}N HSQC spectra of the RIM1α C2B-1 fragment.

(B) ^{1}H-^{15}N HSQC spectra of the RIM1α C2B-3 fragment.

proteins, as well as protein-protein interactions. Thus, we tested whether the RIM1α C_2B domain binds Ca^{2+} by acquiring ^{1}H-^{15}N HSQC spectra of ^{15}N-labeled RIM1α C_2B domain in the absence and presence of Ca^{2+}. Even Ca^{2+} concentrations as high as 10 mM caused practically no perturbation in the ^{1}H-^{15}N HSQC spectrum of ^{15}N-labeled RIM1α C_2B domain (Figure 5.3A), showing that, as predicted, this domain is unable to bind Ca^{2+}. We also used a fluorescence resonance energy transfer assay (Fernandez et al., 2001) to test for Ca^{2+}-dependent phospholipid binding to the RIM1α C_2B domain but no binding was observed (Figure 5.4A), in correlation with its inability to bind Ca^{2+}. These FRET assays commonly detect phospholipid binding to Ca^{2+}-dependent C_2 domains because at least one tryptophan is close to the membrane in their usual Ca^{2+}-induced phospholipid bound orientation. Because the RIM1α C_2B domain could potentially bind to phospholipids in a different orientation that could yield minimal FRET, we also tested for phospholipid binding using ^{15}N-edited 1D ^{1}H NMR spectra of 5 μM ^{15}N-labeled RIM1α C_2B domain. In these spectra, a strong reduction of the signal intensities is expected upon binding to a large unlabeled target such as phospholipid vesicles (Arac et al., 2003). However, no significant perturbations were observed upon the addition of phospholipids in the absence or presence of Ca^{2+} (Figure 5.4B), confirming the FRET results.

The RIM1α C_2B domain was reported to bind to synaptotagmin 1 (Coppola et al., 2001; Schoch et al., 2002), an interaction that could be critical for RIM function given the demonstrated role of synaptotagmin 1 as a Ca^{2+} sensor in the Ca^{2+}-triggered neurotransmitter release (Fernandez-Chacon et al., 2001; Rhee et al., 2005). Hence, we attempted to analyze

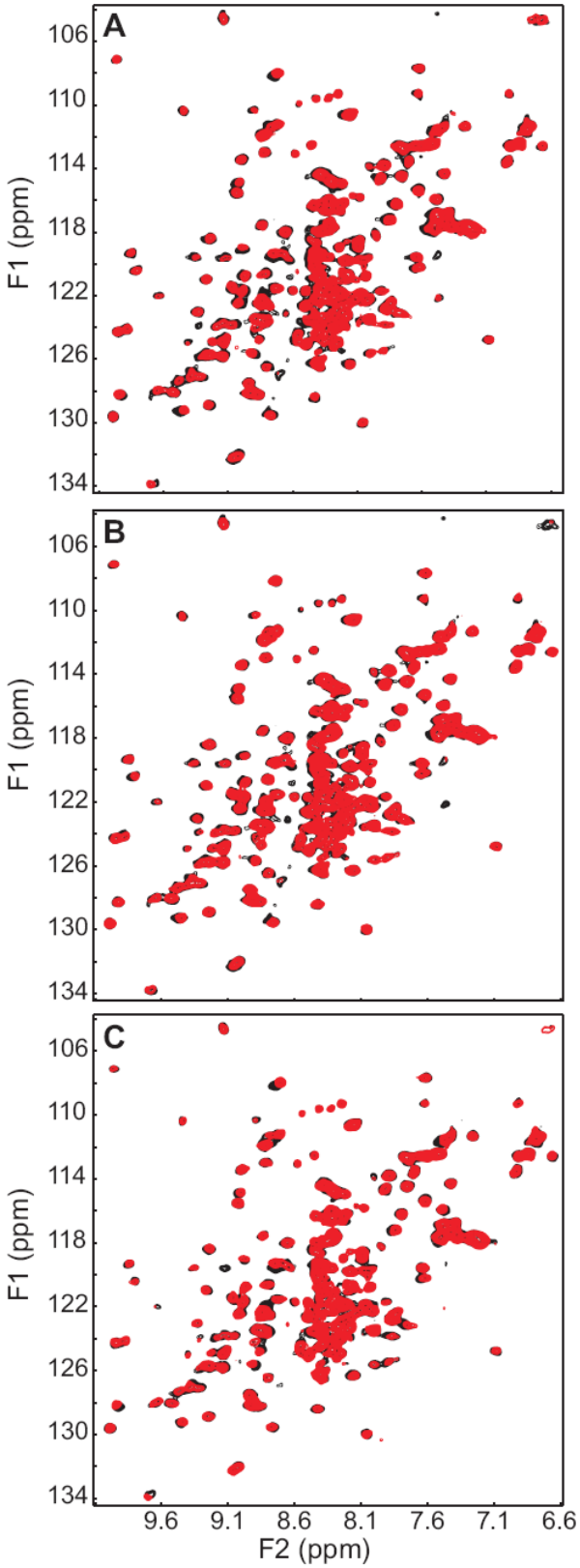
A
B
C
F1 (ppm)
106
110
114
118
122
126
130
134
9.6
9.1
8.6
8.1
7.6
7.1
6.6
F2 (ppm)

Figure 5.3 The RIM1α C_2B domain does not bind to Ca^{2+} or to the synaptotagmin 1 C_2 domains.

(A) ^{1}H-^{15}N HSQC spectra of the RIM1α C_2B domain in the absence (black contours) and presence (red contours) of 10 mM Ca^{2+}. All spectra were acquired at 500 MHz.

(B) ^{1}H-^{15}N HSQC spectra of 80 μM ^{15}N-labeled RIM1α C_2B domain before (black contours) and after (red contours) addition of 100 μM unlabeled synaptotagmin 1 C_2AB fragment in the absence of 10 mM Ca^{2+}.

(C) ^{1}H-^{15}N HSQC spectra of 80 μM ^{15}N-labeled RIM1α C_2B domain before (black contours) and after (red contours) addition of 100 μM unlabeled synaptotagmin 1 C_2AB fragment in the presence of 10 mM Ca^{2+}.

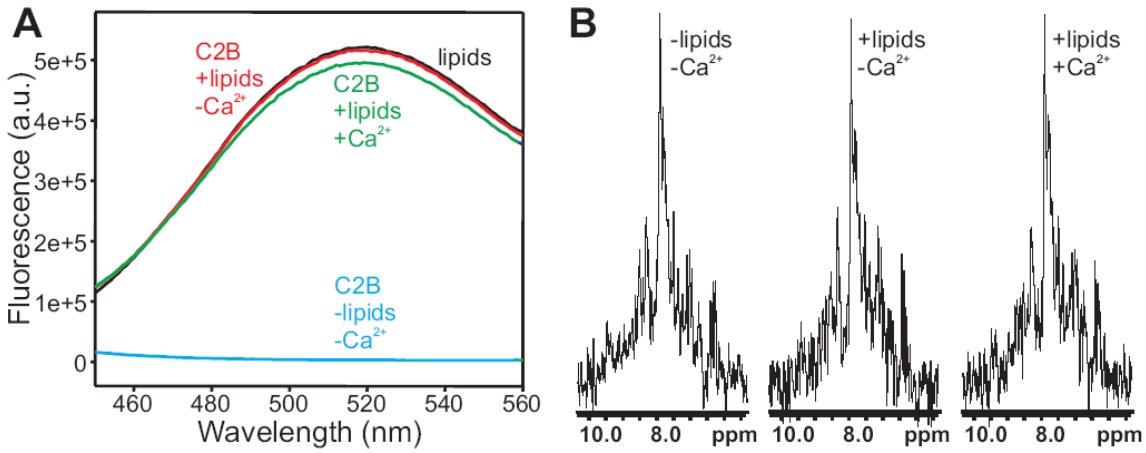

Figure 5.4 The RIM1α C_2B domain does not bind to phospholipids

(A) Fluorescence spectra (excitation at 285 nm) of samples containing 0.01mg/mL phospholipid vesicles composed of 65% PC, 25% PS, and 10% dansyl-PE (black line), 1 μM RIM1α C_2B domain (blue line), or 0.01 mg/mL phospholipid vesicles, and 1 μM RIM1α C_2B domain in 1 mM EDTA (red line) or 1 mM Ca^{2+} (green line).

(B) One dimensional ^{15}N-edited 1H NMR spectra of 5 μM RIM1α C_2B domain without (left panel) or with the addition of 1 mg/mL phospholipid vesicles in the presence of 1 mM EDTA (middle panel) or 1 mM Ca^{2+} (right panel).

this interaction using NMR spectroscopy and a synaptotagmin 1 fragment that spans most of its cytoplasmic region and contains its two C_2 domains (referred to as the C_2AB fragment). However, addition of an excess of unlabeled C_2AB fragment to ^{15}N-labeled RIM1α C_2B domain caused almost no perturbation in the ^{1}H-^{15}N HSQC spectrum of the latter in the absence or presence of 10 mM Ca^{2+} (Figure 5.3B, 5.3C). Analogous results were obtained when we recorded ^{1}H-^{15}N HSQC spectra of ^{15}N-labeled synaptotagmin 1 C_2A domain or C_2B domain in the absence or presence of unlabeled RIM1α C_2B domain (data not shown). It is important to note that ^{1}H-^{15}N HSQC spectra are highly sensitive to protein-protein interactions and that all these data were acquired with soluble, properly folded fragments that are well-characterized by spectroscopic techniques. Hence, these results clearly establish that the isolated RIM1α C_2B domain does not form binary complexes with the synaptotagmin 1 C_2 domains at the protein concentrations used in these experiments (ca. 100 μM), and suggest that sequences beyond the RIM1α C_2B domain and/or the synaptotagmin 1 C_2 domains may be required for direct interactions between these proteins. Using ^{1}H-^{15}N HSQC spectra, we were also unable to observe any interaction between ^{15}N-labeled RIM1α C_2B domain and an unlabeled liprin fragment that was identified as the RIM-binding region of liprins (Schoch et al., 2002), suggesting again that the RIM1α C_2B domain is not sufficient for these previously described interactions, which thus may require additional RIM1α sequences preceding the C_2B domain.

5.3.3 Crystal structure of the RIM1α C_2B domain dimer

Because of lack of obvious molecular mechanism accounting for the functional importance of RIM C2B domain and its limited degree of sequence identity with other C2 domains of known structure, we decided to determine the atomic structure of RIM1α C_2B domain to evaluate the potential existence of specific structural features that might be critical for its function. Based on the good quality of the ^{1}H-^{15}N HSQC spectra of the RIM1α C_2B domain (Figure 5.2B), and following our generally philosophy of using ^{1}H-^{15}N HSQC spectra as a guide for protein crystallization (Chen et al., 2002; Lu et al., 2006; Dai et al., 2004; Dai et al., 2005), we initiated crystallization trials of the RIM1α C_2B domain (fragment C2B-3). Cubic crystals of purified RIM1C2B grew out from 0.1 M sodium citrate (pH 4.1), 1.55 M $(NH_4)_2SO_4$ overnight (Figure 5.5A) and are diffracted to 1.75 Å (Figure 5.5B). Initially, I attempted to solve the crystal structure of the RIM1α C_2B domain using molecule replacement, but not successful. Therefore, I expressed and purified seleno-methionine labeled RIM1α C_2B domain and determined the RIM1α C_2B domain structure by the single-wavelength anomalous dispersion (SAD) method and refined using data to 1.73 Å resolution. A representative region of the electron density is shown in Figure 5.6A, and Table 5.1 summarizes the data collection and refinement statistics.

Each asymmetric unit contains two RIM1α C_2B domains, which form a symmetric dimer in the crystals. A ribbon diagram of one of the monomers is represented in Figure 5.6B, and a superposition of both monomers (Figure 5.6C) shows that they are almost identical (0.31 Å rms deviation between all common heavy atoms). The structure contains a β-sandwich formed by two four-stranded β-sheets (β2 (residues 1462-1472), β3 (residues

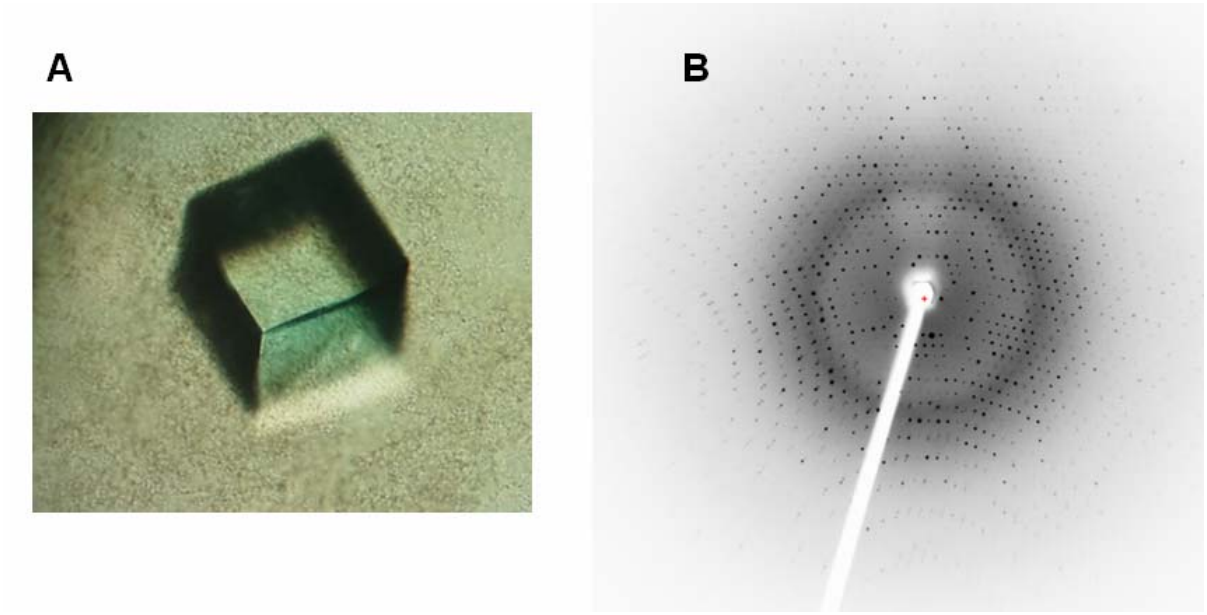

Figure 5.5 Crystallization of the rat RIM1α C_2B domain

(A) Cubic crystals of the rat RIM1α C_2B domain were obtained in 0.1 M sodium citrate (pH 4.1), 1.55 M $(NH_4)_2SO_4$.

(B) Diffraction pattern of the rat RIM1α C_2B domain crystals.

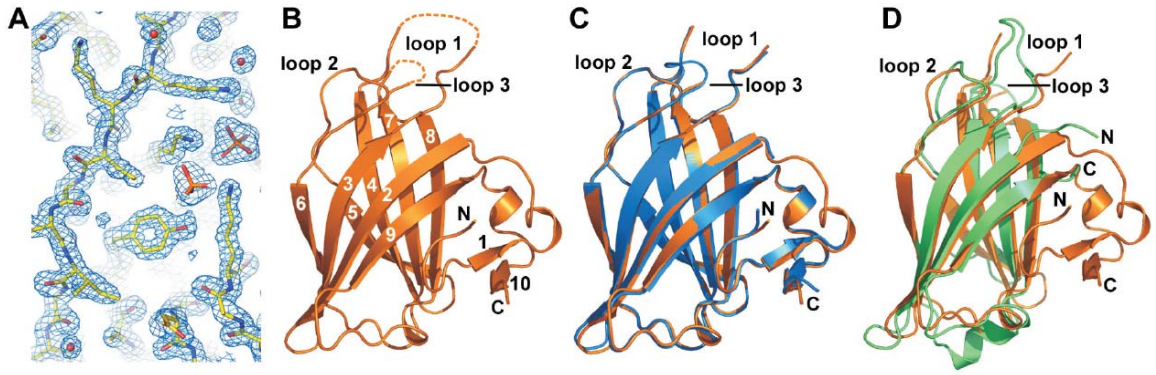

Figure 5.6 Crystal structure of the RIM1α C_2B domain

(A) A region of the $2F_0$-F_c electron density contoured at the 1σ level. Two sulfate ions are clearly visible.

(B) Ribbon diagram of one of the monomers of the RIM1α C_2B domain. The β-strands are labeled with numbers, and the N- and C-termini are indicated with N and C, respectively. The top loops (loops 1-3) that are commonly involved in Ca^{2+} binding to C_2 domains (Rizo and Sudhof, 1998) are also labeled. Note that dashed lines were used to represent arbitrary backbone conformations for a few some residues in these loop that were not observable, likely due to flexibility.

(C) Superposition of the two monomers found within the RIM1α C_2B domain dimer.

(D) Superposition of the RIM1α C_2B domain (orange) with the synaptotagmin 1 C_2A domain (green; PDB accession code 1RSY).

Table 5. 1 Data collection and refinement statistics[§]

A. Data collection	
Space group	$P3_121$
Unit cell dimensions	
a, b, c (Å)	62.0, 62.0, 145.2
Wavelength (Å)	0.97918
Resolution range (Å) [a]	26.41-1.73 (1.76–1.73)
Data completeness [a]	99.9 (100.0)
R_{merge} [‡] (%) [a]	5.7 (74.7)
I/σ(I) [a]	30.9 (2.1)
Multiplicity [a]	7.0 (7.1)
Wilson B factor (Å^2)	25.13
B. Phasing	
Anomalous scatterer	selenium (9 out of 10 possible sites)
Figure of merit (resolution range = 1.73 Å)	0.348
C. Refinement	
Resolution range (Å) [a]	26.40 – 1.73 (1.78-1.73)
No. of reflections R_{work}/R_{free}	33,139/1,400
R_{work}/R_{free} (%) [a]	17.9 (23.2)/21.5 (28.1)
Atoms (non-H protein/water/sulfate ion/ sodium ion/chloride ion)	2,256/189/35/1/3
Average B factor (Å^2)	26.0
R.m.s.d. bond lengths (Å)	0.017
R.m.s.d. bond angles (°)	1.81
Missing residues	A: 1,456-1,460; 1,491-1,493
	B: 1,491-1,493; 1,551-1,553
Ramachandran analysis (most favorable/allowed) (%)	88.0/12.0

[§] Data collection values are as defined in the program HKL2000.
[a] Values in parentheses are for the highest resolution shell.

[‡] $R_{merge} = 100 \sum_h \sum_i |I_{h,i} - \langle I_h \rangle| / \sum_h \sum_i I_{h,i}$, where the outer sum (h) is over the unique reflections and the inner sum (i) is over the set of independent observations of each unique reflection.

1475-1484), β6 (residues 1528-1533) and β9 (residues 1575-1582) forming one sheet, and β4 (residues 1497-1506), β5 (residues 1509-1515), β7 (residues 1540-1549), and β8 (residues 1557-1565) forming the other) that is characteristic of C_2 domains (Rizo and Sudhof, 1998) and encompasses the portion of the RIM1α C_2B domain that exhibits homology to the C_2 domain family (residues 1462-1582). The N- and C-terminal extensions beyond this region form a small subdomain that packs against a largely hydrophobic side of the β-sandwich and includes two separate helical turns and a short, two-stranded antiparallel β-sheet (strands 1 and 10). Such hydrophobic packing may explain the necessity of these N- and C-terminal extensions for the proper folding and/or stability of the RIM1α C_2B domain. Strands 1 and 10 are provided by the very N- and C-termini of the RIM1α C_2B domain, and the strand-strand interaction helps to bring the two termini in close proximity. Note that the loop connecting the short N-terminal strand (strand 1 in Figures 5.6B, 5.6C) to the first strand of the β-sandwich (strand 2 in Figures 5.6B, 5.6C) is partially disordered in one of the monomers (in blue in Figure 5.6C). Partial disorder is also observed in the loops emerging at the top of the β-sandwich that commonly bind Ca^{2+} in C_2 domains, but not in the case of the RIM1α C_2B domain (loops 1-3; Figures 5.6B, 5.6C). Several sulfate ions bound to clusters of basic residues of the RIM1α C_2B domain were observed in the electron density. It is unclear whether this finding arises from potential functional activities of these clusters or from the high concentration of sulfate ions in the crystallization conditions.

The two monomers of the RIM1α C_2B domain dimer are related by a two-fold axis (parallel to the vertical axis in the orientation of Figure 5.7A). The total surface area buried

by dimerization is 900 $Å^2$. Interestingly, the dimer interface is largely formed by the subdomains encompassing the N- and C-terminal extensions of each monomer. The subdomains from each monomer pack against each other and against the concave surface formed by strands 4, 5, 7 and 8 of the β-sandwich from the opposite monomer. The close-up of the dimer interface shown in Figure 5.7B reveals that contacts between the two monomers involve a number of hydrophobic and polar interactions, including a salt bridge between K1513 of one monomer and D1589 of the opposing monomer. A map of the electrostatic potential on the surface of the dimer exhibits a striking dipolar character, with the top half being largely positive and the bottom half large negative. A clear dipolar character was also observed in the RIM1α C_2A domain (Dai et al., 2005). This feature of the RIM C_2 domains may have functional significance, but further research will be required to assess this possibility.

The crystal structure of the RIM1α C_2B domain suggested its potential homodimerization. Consistent with this observation, during our NMR analyses of the RIM1α C_2B domain, we observed that the resonance line widths were concentration dependent. The resonance broadening is illustrated by the signals from well-resolved methyl groups in the 1D ^{1}H NMR spectra of 20 μM, 101 μM, and 406 μM RIM1α C_2B domain shown in Figure 5.8A. Note that the vertical scale of the spectra was normalized for the different protein concentrations, and the resonance broadening is thus manifested not only by the increasing line widths but also by the decreasing intensities at higher protein concentrations. The measured methyl line widths (after subtracting 7 Hz because of the homonuclear coupling

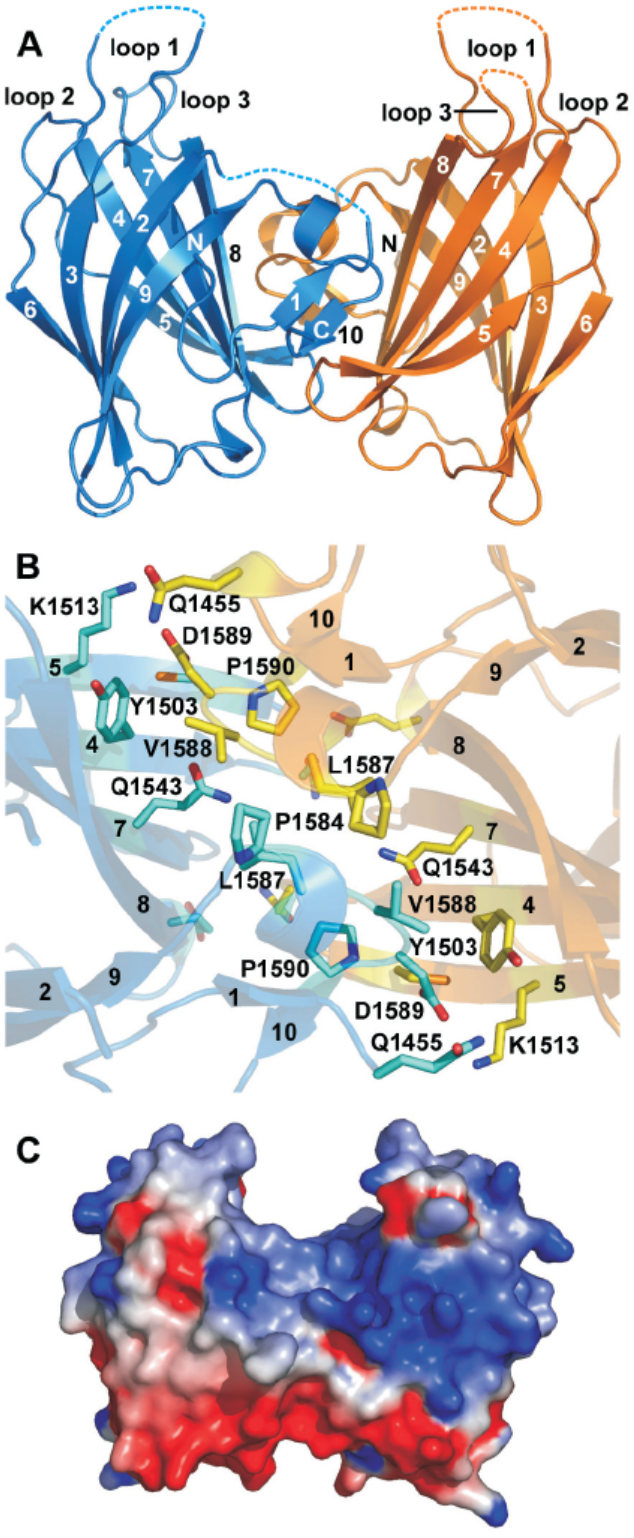
A
loop 1
loop 2
loop 3
loop 1
loop 3
loop 2
N
C
N
B
K1513
Q1455
D1589
P1590
Y1503
V1588
Q1543
P1584
L1587
L1587
Q1543
V1588
Y1503
P1590
D1589
Q1455
K1513
C

Figure 5.7 The RIM1α C_2B domain dimer

(A) Ribbon diagram of the RIM1α C_2B domain dimer with one monomer colored in blue and the other in orange. The labeling scheme for β-strands, termini and top loops is the same is in Figure 5B.

(B) Close-up view of the dimerization interface. The side chains from residues involved in intermolecular contacts and the Cα carbons of the same residues are shown as stick models. Oxygen atoms are in red and nitrogen atoms in blue. Carbon atoms are colored in cyan for one monomer and in yellow for the other monomer. The β-strands are labeled with the corresponding numbers, and the side chains are labeled with the one-letter amino acid code and the residue number.

(C) Surface electrostatic potential of the RIM1α C_2B domain dimer. The electrostatic potential was contoured at the 5 kT/e level, with red denoting negative potential and blue denoting positive potential.

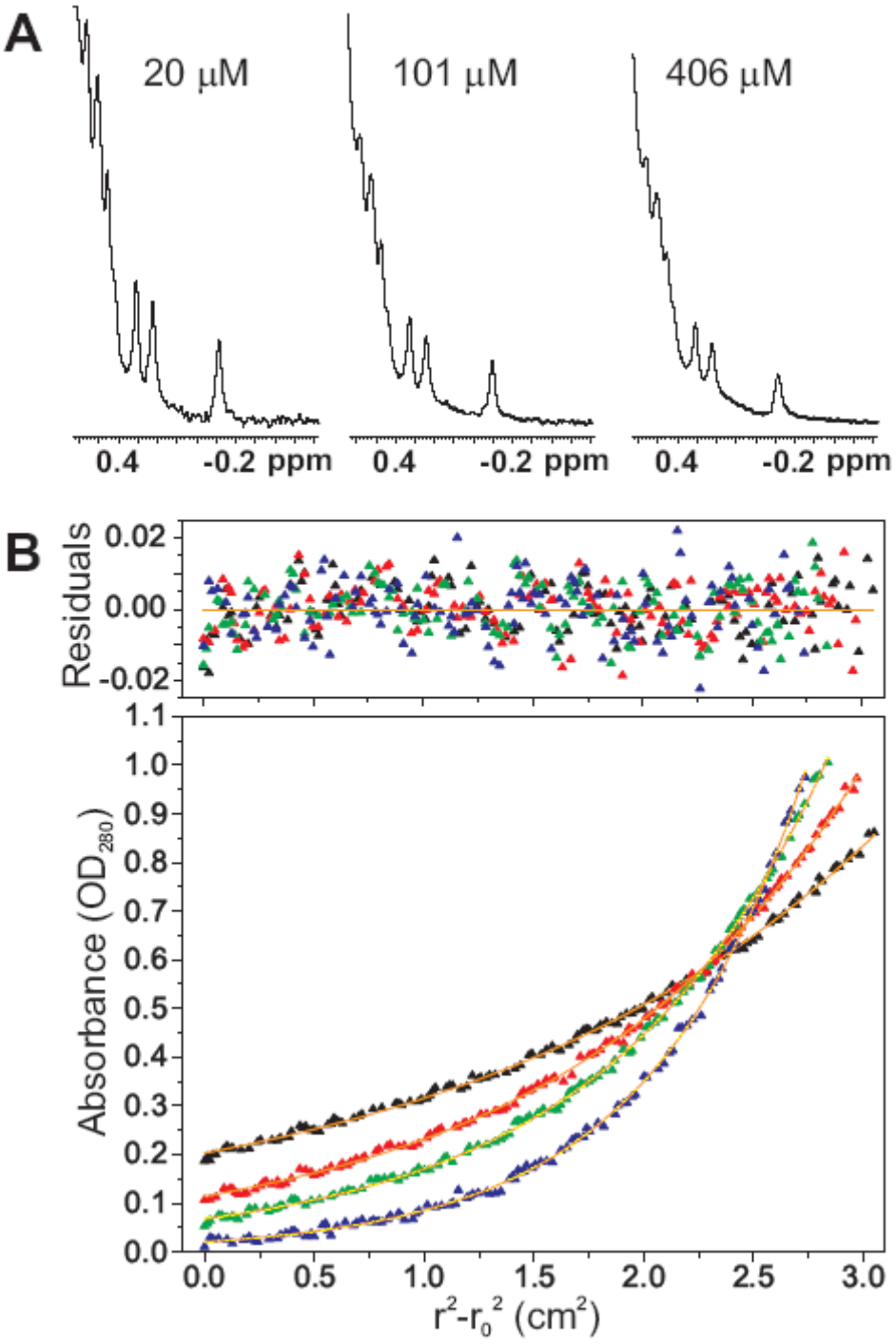
A
20 μM
101 μM
406 μM
0.4
-0.2 ppm
0.4
-0.2 ppm
0.4
-0.2 ppm
B
Residuals
0.02
0.00
-0.02
Absorbance (OD280)
1.1
1.0
0.9
0.8
0.7
0.6
0.5
0.4
0.3
0.2
0.1
0.0
0.0
0.5
1.0
1.5
2.0
2.5
3.0
r2-r02 (cm2)

Figure 5.8 Dimerization of the RIM1α C_2B domain

(A) Expansion of part of the methyl region of ^1H NMR spectra of the RIM1α C_2B domain domain at 20, 101, and 406 μM concentration. For comparison purposes, the vertical scale of the spectra was set to values that were inversely proportional to the protein concentration.

(B) Equilibrium sedimentation analysis of the RIM1α C_2B domain. The data were obtained at centrifugation speeds of 20,000 rpm (black), 25,000 rpm (red), 29,000 rpm (green), and 35,000 rpm (blue). Curves in the bottom panel were generated by fitting the data to a monomer-dimer equilibrium model. The top panel shows the residuals.

with the neighboring methine proton) ranged from 6 to 7 Hz at 12 μM RIM1α C_2B domain, as expected for a monomeric species, to 12-14 Hz at 1.22 mM RIM1α C_2B domain. These results indicated that the RIM1α C_2B domain dimerizes in solution. To confirm this conclusion, we also examined the possibility that the RIM1α C_2B domain might form a dimer using analytical ultracentrifugation. Indeed, equilibrium sedimentation data did not correspond to a monomeric species but could be fitted well to a monomer-dimer equilibrium with a dissociation constant of 96.3 ± 17.5 μM (Figure 5.8B). This result is consistent with the observed NMR line widths as well as the crystal structure of the RIM1α C_2B domain, demonstrating that the RIM1α C_2B domain forms weak dimers in solution.

Figure 5.9 shows a sequence alignment of RIM C_2B domains from different species, the rat RIM1α C_2A domain, and diverse Ca^{2+}-binding C_2 domains whose structures have been previously solved, including those of synaptotagmin 1, PKCs and rabphilin. The alignment illustrates the very high sequence conservation of RIM C_2B domains. Some of the conserved residues are shared with C_2 domains in general, whereas many other residues are selectively conserved in RIM C_2B domains. The alignment also illustrates how the Ca^{2+}-binding C_2 domains are distantly related to both RIM C_2 domains, which at the same time are also distantly related to each other [see (Dai et al., 2005) for a more detailed analysis]. In general, residues involved in dimerization of the RIM1α C_2B domain are highly conserved, domains are represented by magenta cylinders, green arrows and black bars, respectively. The black asterisks indicate residues involved in dimerization and the red asterisks denote the positions of the five aspartate residues that are commonly involved in binding of Ca^{2+} to C_2

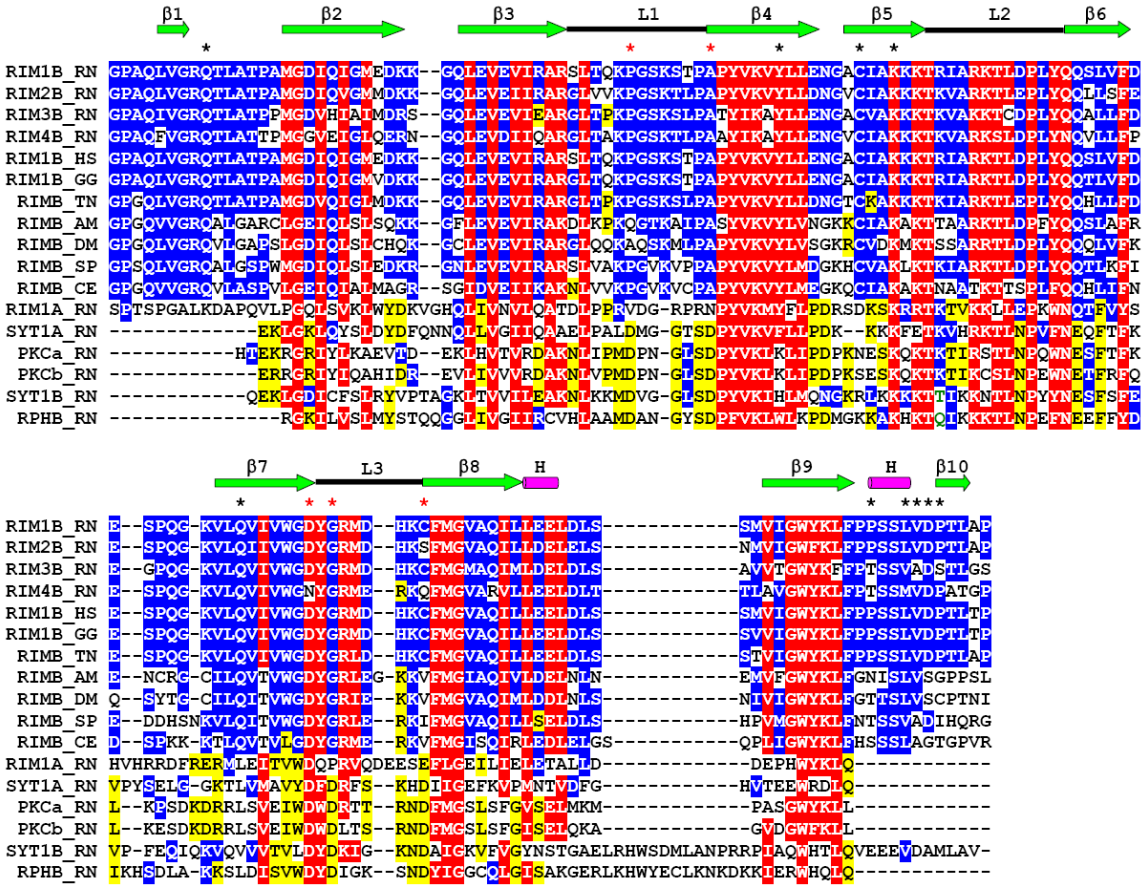

Figure 5.9 Sequence alignment of RIM C_2B domains from different species and selected rat C2-domains

Residues conserved in most C_2-domains (>80% of the sequences displayed; E = D, K = R, N = Q, L = V = I = M, F = Y =W, and S = T) are colored in white with a red background. Residues that appear to be selectively conserved in RIM C_2B domains are colored white with a blue background. Residues that appear to be selectively conserved in other C_2 domains, but not in RIM C_2B domains, are colored black with a yellow background. The secondary structure elements of the rat RIM1α C2B domain are shown at the top of the alignment. Helices, β-strands and the three top loops that are usually involved in binding of Ca^{2+} to C_2

abbreviated PKC, SYT, and RPH, respectively. A and B at the end of the protein name refers to the C_2A domain and the C_2B domain, respectively, whereas a and b at the end of the protein name refer to different PKC isoforms. Species abbreviations: RN, rat (*Rattus norvegicus*); HS, human (*Homo sapiens*); GG, chicken (*Gallus gallus*); TN, spotted green puffer fish (*Tetraodon nigroviridis*); DM, fruit fly (*Drosophila melanogaster*); AM, honey bee (*Apis mellifera*); SP, sea urchin (*Strongylocentrotus purpuratus*); and CE, round worm (*Caenorhabditis elegans*). GenBank entries Q9JIR4 for RIM1B_RN, Q9JIS1 for RIM2B_RN, Q9JIR3 for RIM3B_RN, AAN59931.1 for RIM4B_RN, Q86UR5 for RIM1B_HS, XP_419884.2 for RIM1B_GG, CAG00377.1 for RIMB_TN, XP_393489.3 for RIMB_AM, NP_001014630.1 for RIMB_DM, XP_794399.2 for RIMB_SP, Q22366 for RIMB_CE, Q9JIR4 for RIM1A_RN, P21707 for SYT1A_RN, XP_343976 for PKCa_RN, NP_036845 for PKCb_RN, P21707 for SYT1B_RN, and NP_598202 for RPHB_RN.

domains (Rizo and Sudhof, 1998). Protein kinase C, synaptotagmin, and rabphilin are although those belonging to the C-terminal extension are less conserved in invertebrates (Figure 5.9), suggesting that dimerization may only occur in vertebrate RIMs.

5.3.4 Comparison of the RIM1 C_2B domains with other C_2 domains

A structural comparison using the program DALI (http://www.ebi.ac.uk/dali) (Holm and Sander, 1993) revealed that, as expected, the structure of the RIM1α C_2B domain is similar to those of all C_2 domains deposited in the Protein Data Bank (PDB) (http://www.rcsb.org/pdb). The highest Z score yielded by DALI corresponded to the synaptotagmin 1 C_2A domain (1.65 Å rms deviation between 115 common Cα carbons). The superposition of ribbon diagrams of the RIM1α C_2B domain and the synaptotagmin 1 C_2A domain shown in Figure 5.6D illustrates the close structural similarity of their β-sandwiches despite their low sequence identity (21% using standard sequence alignment tools; 27% using the structure-based sequence alignment yielded by DALI). The superposition also illustrates that the most prominent difference between these two C_2 domains is the subdomain formed by the N- and C-terminal extensions of the RIM1α C_2B domain. It is noteworthy that, although most C_2 domains only contain the β-sandwich, the synaptotagmin 1 C_2B domain (Fernandez et al., 2001) and the Munc13-1 C_2A domain (Lu et al., 2006) provide two examples exhibiting additional structural elements that emerge at the same side of the β-sandwich where the unique subdomain of the RIM1α C_2B domain is located (a C-terminal α-helix in the synaptotagmin 1 C_2B domain and a β-hairpin formed by a long loop sequence in

the Munc13-1 C_2A domain).

5.4 Discussion

RIMs constitute a fascinating family of proteins that play crucial roles in regulating synaptic neurotransmitter release and different forms of presynaptic plasticity, acting also as scaffolds to organize the active zone. Among the different domains found in the different RIM isoforms, only the C_2B domain is present in all of them, suggesting that this domain is a key determinant of RIM function. This notion is also supported by the high evolutionary conservation of the RIM C_2B domain sequence and by rescue experiments of Unc10 mutants in *C. elegans* (Koushika et al., 2001). To provide a basis for understanding the function of the RIM1α C_2B domain, here we have analyzed its three-dimensional structure and interactions with diverse targets using NMR spectroscopy and X-ray crystallography. Our results define the boundaries of the RIM1α C_2B domain, showing that N- and C-terminal extensions are necessary to form a folded, stable module. We find that the RIM1α C_2B domain does not bind Ca^{2+}, as predicted from the fact that this domain contains only one of the five canonical aspartate residues that commonly form the Ca^{2+} binding sites of C_2 domains (see Figure 5.9). We were unable to verify previously described protein-protein interactions involving the RIM1α C_2B domain, but we uncovered a novel interaction, dimerization, that may be important for its function. The crystal structure of the RIM1α C_2B domain reveals how its signature C_2-domain sequence forms a β-sandwich characteristic of C_2 domains, and how the N- and C-terminal extensions form a subdomain that packs against a hydrophobic side of the

β-sandwich. This structure constitutes only the second three-dimensional structure described for a C_2 domain dimer, and the major participation of the unusual subdomain in dimerization suggests that C_2 domains may be able to act as protein-protein interaction domains by diverse mechanisms.

Our sedimentation equilibrium data show that dimerization of the RIM1α C_2B domain is characterized by a relatively weak affinity. However, the dimeric structure observed in the crystals of the RIM1α C_2B domain shows that dimerization arises from specific interactions involving the concave surface of the β-sandwich and the subdomain formed by the N- and C-terminal extensions. Moreover, it is plausible that dimerization may be strengthened by sequences N-terminal to the C_2B domain or by other protein-protein interactions that participate in organizing the active zone and may increase the local concentration of RIMs. Furthermore, the formation of RIM dimers could provide a mechanism to facilitate the Munc13-1 homodimer to Munc13-1/α-RIM heterodimer switch that is likely to play a key role in synaptic vesicle priming (Lu et al., 2006), because the RIM dimer could engage two Munc13-1 molecules during the switch (Figure 5.10). Clearly, further research will be necessary to assess the physiological relevance of the dimerization of the RIM1α C_2B domain and to test this model, but our data raise the possibility that dimerization may be a key aspect of RIM function and the crystal structure of the RIM1α C_2B domain described here will facilitate the design of mutagenesis experiments to test this notion.

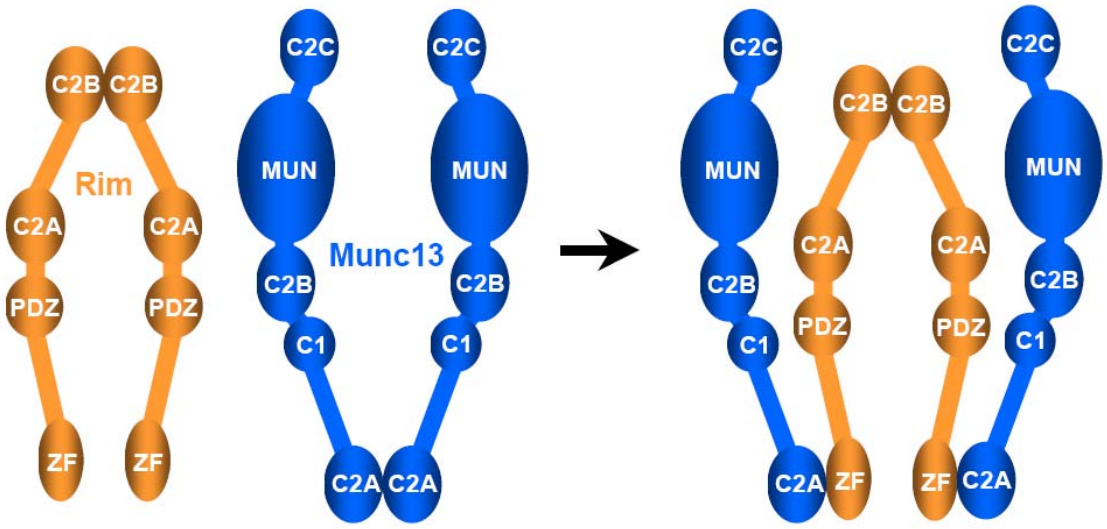

Figure 5.10 Speculative model of how RIM1α C_2B domain dimerization could facilitate the Munc13-1 homodimer to Munc13-1/α-RIM heterodimer switch during synaptic vesicle priming

The key aspect of the model is that the spatial proximity induced by RIM1α dimerization would facilitate binding of two RIM1α molecules to the two molecules that form the Munc13-1 homodimer. In contrast, binding of only one RIM1α molecule would leave one of the two Munc13-1 monomers free.

Two previous studies reported interactions between the RIM1α C_2B domain and synaptotagmin 1 (Coppola et al., 2001; Schoch et al., 2002). Since the synaptotagmin 1 C_2 domains for most of its cytoplasmic region and are largely responsible for synaptotagmin 1 function (Sudhof, 2004; Bai and Chapman, 2004; Rizo et al., 2006), it was surprising that we could not detect an interaction between the synaptotagmin 1 C_2AB fragment and the RIM1α C_2B domain. Because our data were obtained in solution with well-folded proteins that were well characterized by spectroscopic techniques, and because ^{1}H-^{15}N HSQC provides a very sensitive tool to detect protein-protein interactions, our data conclusively show that at least these recombinant RIM1α and synaptotagmin 1 fragments expressed in bacteria do not form binary complexes in the absence or presence of Ca^{2+}. It is noteworthy that in previous studies of the RIM2 C_2A domain by NMR spectroscopy (Dai et al., 2005), we were also unable to detect previously described interactions of this domain with SNAP-25 and synaptotagmin 1 (Coppola et al., 2001). It is plausible that these contradictions arise in part because some of the previous data were obtained with GST-pulldown experiments, which are prone to artifacts. However, it is also possible that RIM1α/synaptotagmin 1 interactions require RIM1α sequences adjacent to its C_2 domains. Note also that we did not detect binding between the isolated RIM1α C_2B domain and a liprin fragment containing the minimal RIM-binding sequence, but the RIM/liprin interaction appears to be tight (Schoch et al., 2002) and is likely to be functionally significant (Kaeser and Sudhof, 2005). Hence, sequences preceding the RIM1α C_2B domain may also be necessary for liprin binding. These results emphasize the need for further research including the sequences adjacent to the RIM C_2 domains to fully understand their biochemical and functional properties.

Our results also have implications for our overall understanding of how C_2 domains function. Initial studies of these widespread protein modules suggested that they generally function as Ca^{2+}-dependent phospholipid binding domains that exhibit little Ca^{2+}-induced structural changes (Rizo and Sudhof, 1998). However, as more C_2 domains are being studied, more examples are found that deviate from this paradigm. For instance, the Piccolo C_2A domain exhibits a drastic Ca^{2+}-induced conformational change (Garcia et al., 2004), and the rat synaptotagmin 4 C_2B domain does not bind Ca^{2+} despite containing a full complement of potential Ca^{2+} ligands (Dai et al., 2004). Recently, the crystal structures of the Munc13-1 C_2A domain homodimer and of the Munc13-1 C_2A domain/RIM2α ZF domain heterodimer (Lu et al., 2006) provided a first glimpse at atomic resolution of how a C_2 domain engages in protein-protein interactions. The crystal structure of the RIM1α C_2B domain described here now reveals the nature of a second C_2 domain dimer at atomic resolution. Although Munc13-1 C_2A domain dimerization also involved the concave sheet of the β-sandwich, the mode of dimerization involved formation of a β-barrel between the concave sheet of each monomer (Lu et al., 2006) and is thus different from the dimerization mode of the RIM1α C_2B domain. Hence, the novel mode of dimerization of the RIM1α C_2B domain suggests that C_2 domains may be able to dimerize and participate in protein-protein interactions by a variety of mechanisms. It appears that we are just starting to uncover this diversity.

BIBLIOGRAPHY

Arac,D., Murphy,T., and Rizo,J. (2003). Facile detection of protein-protein interactions by one-dimensional NMR spectroscopy. Biochemistry *42*, 2774-2780.

Araki,S., Kikuchi,A., Hata,Y., Isomura,M., and Takai,Y. (1990). Regulation of reversible binding of smg p25A, a ras p21-like GTP-binding protein, to synaptic plasma membranes and vesicles by its specific regulatory protein, GDP dissociation inhibitor. J. Biol. Chem. *265*, 13007-13015.

Augustin,I., Rosenmund,C., Sudhof,T.C., and Brose,N. (1999). Munc13-1 is essential for fusion competence of glutamatergic synaptic vesicles. Nature *400*, 457-461.

Bai,J. and Chapman,E.R. (2004). The C2 domains of synaptotagmin--partners in exocytosis. Trends Biochem. Sci. *29*, 143-151.

Bailey,S. (1994). The Ccp4 Suite - Programs for Protein Crystallography. Acta Crystallographica Section D-Biological Crystallography *50*, 760-763.

Barclay,J.W., Craig,T.J., Fisher,R.J., Ciufo,L.F., Evans,G.J., Morgan,A., and Burgoyne,R.D. (2003). Phosphorylation of Munc18 by protein kinase C regulates the kinetics of exocytosis. J. Biol. Chem. *278*, 10538-10545.

Basu,J., Shen,N., Dulubova,I., Lu,J., Guan,R., Guryev,O., Grishin,N.V., Rosenmund,C., and Rizo,J. (2005). A minimal domain responsible for Munc13 activity. Nat. Struct. Mol. Biol. *12*, 1017-1018.

Baumert,M., Maycox,P.R., Navone,F., De,C.P., and Jahn,R. (1989). Synaptobrevin: an integral membrane protein of 18,000 daltons present in small synaptic vesicles of rat brain. EMBO J. *8*, 379-384.

Bennett,M.K. and Scheller,R.H. (1993). The molecular machinery for secretion is conserved from yeast to neurons. Proc. Natl. Acad. Sci. U. S. A *90*, 2559-2563.

Bennett,M.K., Calakos,N., and Scheller,R.H. (1992). Syntaxin: a synaptic protein implicated in docking of synaptic vesicles at presynaptic active zones. Science *257*, 255-259.

Betz,A., Ashery,U., Rickmann,M., Augustin,I., Neher,E., Sudhof,T.C., Rettig,J., and Brose,N. (1998). Munc13-1 is a presynaptic phorbol ester receptor that enhances neurotransmitter release. Neuron *21*, 123-136.

Betz,A., Okamoto,M., Benseler,F., and Brose,N. (1997). Direct interaction of the rat unc-13 homologue Munc13-1 with the N terminus of syntaxin. J. Biol. Chem. *272*, 2520-2526.

Betz,A., Thakur,P., Junge,H.J., Ashery,U., Rhee,J.S., Scheuss,V., Rosenmund,C., Rettig,J.,

and Brose,N. (2001). Functional interaction of the active zone proteins Munc13-1 and RIM1 in synaptic vesicle priming. Neuron *30*, 183-196.

Blasi,J., Chapman,E.R., Link,E., Binz,T., Yamasaki,S., De Camilli,P., Sudhof,T.C., Niemann,H., and Jahn,R. (1993a). Botulinum neurotoxin A selectively cleaves the synaptic protein SNAP-25. Nature *365*, 160-163.

Blasi,J., Chapman,E.R., Yamasaki,S., Binz,T., Niemann,H., and Jahn,R. (1993b). Botulinum neurotoxin C1 blocks neurotransmitter release by means of cleaving HPC-1/syntaxin. EMBO J. *12*, 4821-4828.

Brenner,S. (1974). The genetics of Caenorhabditis elegans. Genetics *77*, 71-94.

Brose,N., Hofmann,K., Hata,Y., and Sudhof,T.C. (1995). Mammalian homologues of Caenorhabditis elegans unc-13 gene define novel family of C2-domain proteins. J. Biol. Chem. *270*, 25273-25280.

Calakos,N., Schoch,S., Sudhof,T.C., and Malenka,R.C. (2004). Multiple roles for the active zone protein RIM1alpha in late stages of neurotransmitter release. Neuron *42*, 889-896.

Carr,C.M., Grote,E., Munson,M., Hughson,F.M., and Novick,P.J. (1999). Sec1p binds to SNARE complexes and concentrates at sites of secretion. J. Cell Biol. *146*, 333-344.

Castillo,P.E., Schoch,S., Schmitz,F., Sudhof,T.C., and Malenka,R.C. (2002). RIM1alpha is required for presynaptic long-term potentiation. Nature *415*, 327-330.

Chen,X., Arac,D., Wang,T.M., Gilpin,C.J., Zimmerberg,J., and Rizo,J. (2006). SNARE-mediated lipid mixing depends on the physical state of the vesicles. Biophys. J. *90*, 2062-2074.

Chen,X., Tomchick,D.R., Kovrigin,E., Arac,D., Machius,M., Sudhof,T.C., and Rizo,J. (2002). Three-dimensional structure of the complexin/SNARE complex. Neuron *33*, 397-409.

Chen,Y.A. and Scheller,R.H. (2001). SNARE-mediated membrane fusion. Nat. Rev. Mol. Cell Biol. *2*, 98-106.

Chook,Y.M. and Blobel,G. (1999). Structure of the nuclear transport complex karyopherin-beta2-Ran x GppNHp. Nature *399*, 230-237.

Coppola,T., Magnin-Luthi,S., Perret-Menoud,V., Gattesco,S., Schiavo,G., and Regazzi,R. (2001). Direct interaction of the Rab3 effector RIM with Ca2+ channels, SNAP-25, and synaptotagmin. J. Biol. Chem. *276*, 32756-32762.

Cowtan,K. and Main,P. (1998). Miscellaneous algorithms for density modification. Acta Crystallogr. D. Biol. Crystallogr. *54*, 487-493.

Craig,T.J., Evans,G.J., and Morgan,A. (2003). Physiological regulation of Munc18/nSec1 phosphorylation on serine-313. J. Neurochem. *86*, 1450-1457.

Dai,H., Shen,N., Arac,D., and Rizo,J. (2007). A quaternary SNARE-synaptotagmin-Ca2+-phospholipid complex in neurotransmitter release. J. Mol. Biol. *367*, 848-863.

Dai,H., Shin,O.H., Machius,M., Tomchick,D.R., Sudhof,T.C., and Rizo,J. (2004). Structural basis for the evolutionary inactivation of Ca2+ binding to synaptotagmin 4. Nature Structural & Molecular Biology *11*, 844-849.

Dai,H., Tomchick,D.R., Garcia,J., Sudhof,T.C., Machius,M., and Rizo,J. (2005). Crystal Structure of the RIM2 C(2)A-Domain at 1.4 A Resolution(,). Biochemistry *44*, 13533-13542.

Darchen,F. and Goud,B. (2000). Multiple aspects of Rab protein action in the secretory pathway: focus on Rab3 and Rab6. Biochimie *82*, 375-384.

Davletov,B.A. and Sudhof,T.C. (1993). A single C2 domain from synaptotagmin I is sufficient for high affinity Ca2+/phospholipid binding. J. Biol. Chem. *268*, 26386-26390.

Deken,S.L., Vincent,R., Hadwiger,G., Liu,Q., Wang,Z.W., and Nonet,M.L. (2005). Redundant localization mechanisms of RIM and ELKS in Caenorhabditis elegans. J. Neurosci. *25*, 5975-5983.

Delaglio,F., Grzesiek,S., Vuister,G.W., Zhu,G., Pfeifer,J., and Bax,A. (1995). Nmrpipe - A Multidimensional Spectral Processing System Based on Unix Pipes. Journal of Biomolecular Nmr *6*, 277-293.

Dulubova,I., Khvotchev,M., Liu,S., Huryeva,I., Sudhof,T.C., and Rizo,J. (2007). Munc18-1 binds directly to the neuronal SNARE complex. Proc. Natl. Acad. Sci. U. S. A.

Dulubova,I., Lou,X., Lu,J., Huryeva,I., Alam,A., Schneggenburger,R., Sudhof,T.C., and Rizo,J. (2005). A Munc13/RIM/Rab3 tripartite complex: from priming to plasticity? EMBO J. *24*, 2839-2850.

Dulubova,I., Sugita,S., Hill,S., Hosaka,M., Fernandez,I., Sudhof,T.C., and Rizo,J. (1999). A conformational switch in syntaxin during exocytosis: role of munc18. EMBO J. *18*, 4372-4382.

Dulubova,I., Yamaguchi,T., Arac,D., Li,H., Huryeva,I., Min,S.W., Rizo,J., and Sudhof,T.C. (2003). Convergence and divergence in the mechanism of SNARE binding by Sec1/Munc18-like proteins. Proc. Natl. Acad. Sci. U. S. A *100*, 32-37.

Emsley,P. and Cowtan,K. (2004). Coot: model-building tools for molecular graphics. Acta Crystallogr. D. Biol. Crystallogr. *60*, 2126-2132.

Fasshauer,D., Eliason,W.K., Brunger,A.T., and Jahn,R. (1998a). Identification of a minimal

core of the synaptic SNARE complex sufficient for reversible assembly and disassembly. Biochemistry *37*, 10354-10362.

Fasshauer,D., Sutton,R.B., Brunger,A.T., and Jahn,R. (1998b). Conserved structural features of the synaptic fusion complex: SNARE proteins reclassified as Q- and R-SNAREs. Proc. Natl. Acad. Sci. U. S. A *95*, 15781-15786.

Feldmann,J., Callebaut,I., Raposo,G., Certain,S., Bacq,D., Dumont,C., Lambert,N., Ouachee-Chardin,M., Chedeville,G., Tamary,H., Minard-Colin,V., Vilmer,E., Blanche,S., Le,D.F., Fischer,A., and de Saint,B.G. (2003). Munc13-4 is essential for cytolytic granules fusion and is mutated in a form of familial hemophagocytic lymphohistiocytosis (FHL3). Cell *115*, 461-473.

Fernandez,I., Arac,D., Ubach,J., Gerber,S.H., Shin,O., Gao,Y., Anderson,R.G., Sudhof,T.C., and Rizo,J. (2001). Three-dimensional structure of the synaptotagmin 1 c(2)b-domain. Synaptotagmin 1 as a phospholipid binding machine. Neuron *32*, 1057-1069.

Fernandez,I., Ubach,J., Dulubova,I., Zhang,X., Sudhof,T.C., and Rizo,J. (1998). Three-dimensional structure of an evolutionarily conserved N-terminal domain of syntaxin 1A. Cell *94*, 841-849.

Fernandez-Chacon,R., Konigstorfer,A., Gerber,S.H., Garcia,J., Matos,M.F., Stevens,C.F., Brose,N., Rizo,J., Rosenmund,C., and Sudhof,T.C. (2001). Synaptotagmin I functions as a calcium regulator of release probability. Nature *410*, 41-49.

Ferro-Novick,S. and Jahn,R. (1994). Vesicle fusion from yeast to man. Nature *370*, 191-193.

Fischer,v.M., Sudhof,T.C., and Jahn,R. (1991). A small GTP-binding protein dissociates from synaptic vesicles during exocytosis. Nature *349*, 79-81.

Fletcher,A.I., Shuang,R., Giovannucci,D.R., Zhang,L., Bittner,M.A., and Stuenkel,E.L. (1999). Regulation of exocytosis by cyclin-dependent kinase 5 via phosphorylation of Munc18. J. Biol. Chem. *274*, 4027-4035.

Fujita,Y., Sasaki,T., Fukui,K., Kotani,H., Kimura,T., Hata,Y., Sudhof,T.C., Scheller,R.H., and Takai,Y. (1996). Phosphorylation of Munc-18/n-Sec1/rbSec1 by protein kinase C: its implication in regulating the interaction of Munc-18/n-Sec1/rbSec1 with syntaxin. J. Biol. Chem. *271*, 7265-7268.

Gallwitz,D. and Jahn,R. (2003). The riddle of the Sec1/Munc-18 proteins - new twists added to their interactions with SNAREs. Trends Biochem. Sci. *28*, 113-116.

Garcia,J., Gerber,S.H., Sugita,S., Sudhof,T.C., and Rizo,J. (2004). A conformational switch in the Piccolo C2A domain regulated by alternative splicing. Nat. Struct. Mol. Biol. *11*, 45-53.

Garner,C.C., Kindler,S., and Gundelfinger,E.D. (2000). Molecular determinants of presynaptic active zones. Curr. Opin. Neurobiol. *10*, 321-327.

Geppert,M., Bolshakov,V.Y., Siegelbaum,S.A., Takei,K., De Camilli,P., Hammer,R.E., and Sudhof,T.C. (1994a). The role of Rab3A in neurotransmitter release. Nature *369*, 493-497.

Geppert,M., Goda,Y., Hammer,R.E., Li,C., Rosahl,T.W., Stevens,C.F., and Sudhof,T.C. (1994b). Synaptotagmin I: a major Ca2+ sensor for transmitter release at a central synapse. Cell *79*, 717-727.

Giraudo,C.G., Eng,W.S., Melia,T.J., and Rothman,J.E. (2006). A clamping mechanism involved in SNARE-dependent exocytosis. Science *313*, 676-680.

Grosshans,B.L., Ortiz,D., and Novick,P. (2006). Rabs and their effectors: achieving specificity in membrane traffic. Proc. Natl. Acad. Sci. U. S. A *103*, 11821-11827.

Grote,E., Carr,C.M., and Novick,P.J. (2000). Ordering the final events in yeast exocytosis. J. Cell Biol. *151*, 439-452.

Hakes,D.J. and Dixon,J.E. (1992). New Vectors for High-Level Expression of Recombinant Proteins in Bacteria. Analytical Biochemistry *202*, 293-298.

Hanson,P.I., Roth,R., Morisaki,H., Jahn,R., and Heuser,J.E. (1997). Structure and conformational changes in NSF and its membrane receptor complexes visualized by quick-freeze/deep-etch electron microscopy. Cell *90*, 523-535.

Hayashi,T., McMahon,H., Yamasaki,S., Binz,T., Hata,Y., Sudhof,T.C., and Niemann,H. (1994). Synaptic vesicle membrane fusion complex: action of clostridial neurotoxins on assembly. EMBO J. *13*, 5051-5061.

Hess,D.T., Slater,T.M., Wilson,M.C., and Skene,J.H. (1992). The 25 kDa synaptosomal-associated protein SNAP-25 is the major methionine-rich polypeptide in rapid axonal transport and a major substrate for palmitoylation in adult CNS. J. Neurosci. *12*, 4634-4641.

Hibino,H., Pironkova,R., Onwumere,O., Vologodskaia,M., Hudspeth,A.J., and Lesage,F. (2002). RIM binding proteins (RBPs) couple Rab3-interacting molecules (RIMs) to voltage-gated Ca(2+) channels. Neuron *34*, 411-423.

Holm,L. and Sander,C. (1993). Protein structure comparison by alignment of distance matrices. J. Mol. Biol. *233*, 123-138.

Hu,K., Carroll,J., Fedorovich,S., Rickman,C., Sukhodub,A., and Davletov,B. (2002). Vesicular restriction of synaptobrevin suggests a role for calcium in membrane fusion. Nature *415*, 646-650.

Hunt,D.M., Johnson,S., Halford,S., Morris,A.M., Patel,R., Zhang,K., Hardcastle,A., and

Moore,A.T. (2002). Genomic structure and pattern of alternate splicing for RIM1. A candidate gene for CORD7. Investigative Ophthalmology & Visual Science *43*, U180.

Jahn,R. and Scheller,R.H. (2006). SNAREs--engines for membrane fusion. Nat. Rev. Mol. Cell Biol. *7*, 631-643.

Jahn,R. and Sudhof,T.C. (1999). Membrane fusion and exocytosis. Annu. Rev. Biochem. *68*, 863-911.

Johnson,B.A. and Blevins,R.A. (1994). Nmr View - A Computer-Program for the Visualization and Analysis of Nmr Data. Journal of Biomolecular Nmr *4*, 603-614.

Johnson,S., Halford,S., Morris,A.G., Patel,R.J., Wilkie,S.E., Hardcastle,A.J., Moore,A.T., Zhang,K., and Hunt,D.M. (2003). Genomic organisation and alternative splicing of human RIM1, a gene implicated in autosomal dominant cone-rod dystrophy (CORD7). Genomics *81*, 304-314.

Johnston,P.A., Archer,B.T., III, Robinson,K., Mignery,G.A., Jahn,R., and Sudhof,T.C. (1991). rab3A attachment to the synaptic vesicle membrane mediated by a conserved polyisoprenylated carboxy-terminal sequence. Neuron *7*, 101-109.

Jones,T.A., Zou,J.Y., Cowan,S.W., and Kjeldgaard,M. (1991). Improved Methods for Building Protein Models in Electron-Density Maps and the Location of Errors in These Models. Acta Crystallographica Section A *47*, 110-119.

Junge,H.J., Rhee,J.S., Jahn,O., Varoqueaux,F., Spiess,J., Waxham,M.N., Rosenmund,C., and Brose,N. (2004). Calmodulin and Munc13 form a Ca2+ sensor/effector complex that controls short-term synaptic plasticity. Cell *118*, 389-401.

Kaeser,P.S. and Sudhof,T.C. (2005). RIM function in short- and long-term synaptic plasticity. Biochem. Soc. Trans. *33*, 1345-1349.

Kandel,E.R., Schwartz,J.H., and Jessell,T.M. (1991). Principles of Neural Science. (New York: McGraw-Hill).

Khvotchev,M., Dulubova,I., Sun,J., Dai,H., Rizo,J., and Südhof,T.C. (2007) Dual modes of Munc18-1/SNARE interactions are coupled by functionally critical binding to syntaxin-1 N-terminus. J. Neurosci. (In press)

Koushika,S.P., Richmond,J.E., Hadwiger,G., Weimer,R.M., Jorgensen,E.M., and Nonet,M.L. (2001). A post-docking role for active zone protein Rim. Nat. Neurosci. *4*, 997-1005.

Kweon,D.H., Kim,C.S., and Shin,Y.K. (2003). Regulation of neuronal SNARE assembly by the membrane. Nat. Struct. Biol. *10*, 440-447.

Lackner,M.R., Nurrish,S.J., and Kaplan,J.M. (1999). Facilitation of synaptic transmission by

EGL-30 Gqalpha and EGL-8 PLCbeta: DAG binding to UNC-13 is required to stimulate acetylcholine release. Neuron *24*, 335-346.

Li,C., Takei,K., Geppert,M., Daniell,L., Stenius,K., Chapman,E.R., Jahn,R., De Camilli,P., and Sudhof,T.C. (1994). Synaptic targeting of rabphilin-3A, a synaptic vesicle Ca2+/phospholipid-binding protein, depends on rab3A/3C. Neuron *13*, 885-898.

Li,L., Shin,O.H., Rhee,J.S., Arac,D., Rah,J.C., Rizo,J., Sudhof,T., and Rosenmund,C. (2006). Phosphatidylinositol phosphates as co-activators of Ca2+ binding to C2 domains of synaptotagmin 1. J. Biol. Chem. *281*, 15845-15852.

Link,E., Edelmann,L., Chou,J.H., Binz,T., Yamasaki,S., Eisel,U., Baumert,M., Sudhof,T.C., Niemann,H., and Jahn,R. (1992). Tetanus toxin action: inhibition of neurotransmitter release linked to synaptobrevin proteolysis. Biochem. Biophys. Res. Commun. *189*, 1017-1023.

Lonart,G., Schoch,S., Kaeser,P.S., Larkin,C.J., Sudhof,T.C., and Linden,D.J. (2003). Phosphorylation of RIM1 alpha by PKA triggers presynaptic long-term potentiation at cerebellar parallel fiber synapses. Cell *115*, 49-60.

Lu,J., Li,H., Wang,Y., Sudhof,T.C., and Rizo,J. (2005). Solution structure of the RIM1alpha PDZ domain in complex with an ELKS1b C-terminal peptide. J. Mol. Biol. *352*, 455-466.

Lu,J., Machius,M., Dulubova,I., Dai,H., Sudhof,T.C., Tomchick,D.R., and Rizo,J. (2006). Structural basis for a Munc13-1 homodimer to Munc13-1/RIM heterodimer switch. PLoS. Biol. *4*, e192.

Maruyama,I.N. and Brenner,S. (1991). A phorbol ester/diacylglycerol-binding protein encoded by the unc-13 gene of Caenorhabditis elegans. Proc. Natl. Acad. Sci. U. S. A *88*, 5729-5733.

Matthews,B.W. (1968). Solvent content of protein crystals. J. Mol. Biol. *33*, 491-497.

Misura,K.M., Scheller,R.H., and Weis,W.I. (2000). Three-dimensional structure of the neuronal-Sec1-syntaxin 1a complex. Nature *404*, 355-362.

Murshudov,G.N., Vagin,A.A., and Dodson,E.J. (1997). Refinement of macromolecular structures by the maximum-likelihood method. Acta Crystallographica Section D-Biological Crystallography *53*, 240-255.

Newton,A.C. (1995). Protein kinase C: structure, function, and regulation. J. Biol. Chem. *270*, 28495-28498.

Otwinowski,Z. (1991). In Isomorphous Replacement and Anomalous Scattering, W.Wolf, P.R.Evans, and A.G.W.Leslie, eds. (Cambridge: Science & Engineering Research Council), pp. 80-86.

Otwinowski,Z. and Minor,W. (1997). Processing of X-ray diffraction data collected in oscillation mode. Macromolecular Crystallography, Pt A *276*, 307-326.

Oyler,G.A., Higgins,G.A., Hart,R.A., Battenberg,E., Billingsley,M., Bloom,F.E., and Wilson,M.C. (1989). The identification of a novel synaptosomal-associated protein, SNAP-25, differentially expressed by neuronal subpopulations. J. Cell Biol. *109*, 3039-3052.

Perin,M.S., Brose,N., Jahn,R., and Sudhof,T.C. (1991). Domain structure of synaptotagmin (p65). J. Biol. Chem. *266*, 623-629.

Perin,M.S., Fried,V.A., Mignery,G.A., Jahn,R., and Sudhof,T.C. (1990). Phospholipid binding by a synaptic vesicle protein homologous to the regulatory region of protein kinase C. Nature *345*, 260-263.

Poirier,M.A., Hao,J.C., Malkus,P.N., Chan,C., Moore,M.F., King,D.S., and Bennett,M.K. (1998a). Protease resistance of syntaxin.SNAP-25.VAMP complexes. Implications for assembly and structure. J. Biol. Chem. *273*, 11370-11377.

Poirier,M.A., Xiao,W., Macosko,J.C., Chan,C., Shin,Y.K., and Bennett,M.K. (1998b). The synaptic SNARE complex is a parallel four-stranded helical bundle. Nat. Struct. Biol. *5*, 765-769.

Powell,C.M., Schoch,S., Monteggia,L., Barrot,M., Matos,M.F., Feldmann,N., Sudhof,T.C., and Nestler,E.J. (2004). The presynaptic active zone protein RIM1alpha is critical for normal learning and memory. Neuron *42*, 143-153.

Reim,K., Mansour,M., Varoqueaux,F., McMahon,H.T., Sudhof,T.C., Brose,N., and Rosenmund,C. (2001). Complexins regulate a late step in Ca2+-dependent neurotransmitter release. Cell *104*, 71-81.

Reim,K., Wegmeyer,H., Brandstatter,J.H., Xue,M., Rosenmund,C., Dresbach,T., Hofmann,K., and Brose,N. (2005). Structurally and functionally unique complexins at retinal ribbon synapses. J. Cell Biol. *169*, 669-680.

Rhee,J.S., Betz,A., Pyott,S., Reim,K., Varoqueaux,F., Augustin,I., Hesse,D., Sudhof,T.C., Takahashi,M., Rosenmund,C., and Brose,N. (2002). Beta phorbol ester- and diacylglycerol-induced augmentation of transmitter release is mediated by Munc13s and not by PKCs. Cell *108*, 121-133.

Rhee,J.S., Li,L.Y., Shin,O.H., Rah,J.C., Rizo,J., Sudhof,T.C., and Rosenmund,C. (2005). Augmenting neurotransmitter release by enhancing the apparent Ca2+ affinity of synaptotagmin 1. Proc. Natl. Acad. Sci. U. S. A *102*, 18664-18669.

Richmond,J.E., Davis,W.S., and Jorgensen,E.M. (1999). UNC-13 is required for synaptic vesicle fusion in C. elegans. Nat. Neurosci. *2*, 959-964.

Richmond,J.E., Weimer,R.M., and Jorgensen,E.M. (2001). An open form of syntaxin bypasses the requirement for UNC-13 in vesicle priming. Nature *412*, 338-341.

Rigaud,J.L. and Levy,D. (2003). Reconstitution of membrane proteins into liposomes. Methods Enzymol. *372*, 65-86.

Rigaud,J.L., Pitard,B., and Levy,D. (1995). Reconstitution of membrane proteins into liposomes: application to energy-transducing membrane proteins. Biochim. Biophys. Acta *1231*, 223-246.

Rizo,J. and Sudhof,T.C. (1998). C2-domains, structure and function of a universal Ca2+-binding domain. J. Biol. Chem. *273*, 15879-15882.

Rizo,J. and Sudhof,T.C. (2002). Snares and munc18 in synaptic vesicle fusion. Nat. Rev. Neurosci. *3*, 641-653.

Rizo,J., Chen,X., and Arac,D. (2006). Unraveling the mechanisms of synaptotagmin and SNARE function in neurotransmitter release. Trends Cell Biol. *16*, 339-350.

Rosenmund,C., Rettig,J., and Brose,N. (2003). Molecular mechanisms of active zone function. Curr. Opin. Neurobiol. *13*, 509-519.

Rosenmund,C., Sigler,A., Augustin,I., Reim,K., Brose,N., and Rhee,J.S. (2002). Differential control of vesicle priming and short-term plasticity by Munc13 isoforms. Neuron *33*, 411-424.

Rothman,J.E. (1994). Intracellular membrane fusion. Adv. Second Messenger Phosphoprotein Res. *29*, 81-96.

Sabatini,B.L. and Regehr,W.G. (1999). Timing of synaptic transmission. Annu. Rev. Physiol *61*, 521-542.

Schaub,J.R., Lu,X., Doneske,B., Shin,Y.K., and McNew,J.A. (2006). Hemifusion arrest by complexin is relieved by Ca2+-synaptotagmin I. Nat. Struct. Mol. Biol. *13*, 748-750.

Schekman,R. and Orci,L. (1996). Coat proteins and vesicle budding. Science *271*, 1526-1533.

Schiavo,G., Benfenati,F., Poulain,B., Rossetto,O., Polverino,d.L., DasGupta,B.R., and Montecucco,C. (1992). Tetanus and botulinum-B neurotoxins block neurotransmitter release by proteolytic cleavage of synaptobrevin. Nature *359*, 832-835.

Schneider,T.R. and Sheldrick,G.M. (2002). Substructure solution with SHELXD. Acta Crystallogr. D. Biol. Crystallogr. *58*, 1772-1779.

Schoch,S., Castillo,P.E., Jo,T., Mukherjee,K., Geppert,M., Wang,Y., Schmitz,F.,

Malenka,R.C., and Sudhof,T.C. (2002). RIM1alpha forms a protein scaffold for regulating neurotransmitter release at the active zone. Nature *415*, 321-326.

Schoch,S., Mittelstaedt,T., Kaeser,P.S., Padgett,D., Feldmann,N., Chevaleyre,V., Castillo,P.E., Hammer,R.E., Han,W., Schmitz,F., Lin,W., and Sudhof,T.C. (2006). Redundant functions of RIM1alpha and RIM2alpha in Ca(2+)-triggered neurotransmitter release. EMBO J. *25*, 5852-5863.

Shao,X., Davletov,B.A., Sutton,R.B., Sudhof,T.C., and Rizo,J. (1996). Bipartite Ca2+-binding motif in C2 domains of synaptotagmin and protein kinase C. Science *273*, 248-251.

Shao,X., Fernandez,I., Sudhof,T.C., and Rizo,J. (1998). Solution structures of the Ca2+-free and Ca2+-bound C2A domain of synaptotagmin I: does Ca2+ induce a conformational change? Biochemistry *37*, 16106-16115.

Shen,J., Tareste,D.C., Paumet,F., Rothman,J.E., and Melia,T.J. (2007). Selective activation of cognate SNAREpins by Sec1/Munc18 proteins. Cell *128*, 183-195.

Shen,N., Guryev,O., and Rizo,J. (2005). Intramolecular occlusion of the diacylglycerol-binding site in the C1 domain of munc13-1. Biochemistry *44*, 1089-1096.

Shirakawa,R., Higashi,T., Tabuchi,A., Yoshioka,A., Nishioka,H., Fukuda,M., Kita,T., and Horiuchi,H. (2004). Munc13-4 is a GTP-Rab27-binding protein regulating dense core granule secretion in platelets. J. Biol. Chem. *279*, 10730-10737.

Shirataki,H., Kaibuchi,K., Sakoda,T., Kishida,S., Yamaguchi,T., Wada,K., Miyazaki,M., and Takai,Y. (1993). Rabphilin-3A, a putative target protein for smg p25A/rab3A p25 small GTP-binding protein related to synaptotagmin. Mol. Cell Biol. *13*, 2061-2068.

Shuang,R., Zhang,L., Fletcher,A., Groblewski,G.E., Pevsner,J., and Stuenkel,E.L. (1998). Regulation of Munc-18/syntaxin 1A interaction by cyclin-dependent kinase 5 in nerve endings. J. Biol. Chem. *273*, 4957-4966.

Sollner,T., Whiteheart,S.W., Brunner,M., Erdjument-Bromage,H., Geromanos,S., Tempst,P., and Rothman,J.E. (1993). SNAP receptors implicated in vesicle targeting and fusion. Nature *362*, 318-324.

Sollner,T.H. (2003). Regulated exocytosis and SNARE function (Review). Mol. Membr. Biol. *20*, 209-220.

Song,Y., Ailenberg,M., and Silverman,M. (1998). Cloning of a novel gene in the human kidney homologous to rat munc13s: its potential role in diabetic nephropathy. Kidney Int. *53*, 1689-1695.

Stevens,D.R., Wu,Z.X., Matti,U., Junge,H.J., Schirra,C., Becherer,U., Wojcik,S.M.,

Brose,N., and Rettig,J. (2005). Identification of the minimal protein domain required for priming activity of Munc13-1. Curr. Biol. *15*, 2243-2248.

Sudhof,T.C. (1995). The synaptic vesicle cycle: a cascade of protein-protein interactions. Nature *375*, 645-653.

Sudhof,T.C. (2004). The synaptic vesicle cycle. Annu. Rev. Neurosci. *27*, 509-547.

Sugita,S., Shin,O.H., Han,W., Lao,Y., and Sudhof,T.C. (2002). Synaptotagmins form a hierarchy of exocytotic Ca(2+) sensors with distinct Ca(2+) affinities. EMBO J. *21*, 270-280.

Sutton,R.B., Davletov,B.A., Berghuis,A.M., Sudhof,T.C., and Sprang,S.R. (1995). Structure of the first C2 domain of synaptotagmin I: a novel Ca2+/phospholipid-binding fold. Cell *80*, 929-938.

Sutton,R.B., Fasshauer,D., Jahn,R., and Brunger,A.T. (1998). Crystal structure of a SNARE complex involved in synaptic exocytosis at 2.4 A resolution. Nature *395*, 347-353.

Takao-Rikitsu,E., Mochida,S., Inoue,E., guchi-Tawarada,M., Inoue,M., Ohtsuka,T., and Takai,Y. (2004). Physical and functional interaction of the active zone proteins, CAST, RIM1, and Bassoon, in neurotransmitter release. J. Cell Biol. *164*, 301-311.

Tang,J., Maximov,A., Shin,O.H., Dai,H., Rizo,J., and Sudhof,T.C. (2006). A complexin/synaptotagmin 1 switch controls fast synaptic vesicle exocytosis. Cell *126*, 1175-1187.

Trimble,W.S., Cowan,D.M., and Scheller,R.H. (1988). Vamp-1 - A Synaptic Vesicle-Associated Integral Membrane-Protein. Proceedings of the National Academy of Sciences of the United States of America *85*, 4538-4542.

Ubach,J., Garcia,J., Nittler,M.P., Sudhof,T.C., and Rizo,J. (1999). Structure of the Janus-faced C2B domain of rabphilin. Nat. Cell Biol. *1*, 106-112.

Ubach,J., Zhang,X., Shao,X., Sudhof,T.C., and Rizo,J. (1998). Ca2+ binding to synaptotagmin: how many Ca2+ ions bind to the tip of a C2-domain? EMBO J. *17*, 3921-3930.

Varoqueaux,F., Sigler,A., Rhee,J.S., Brose,N., Enk,C., Reim,K., and Rosenmund,C. (2002). Total arrest of spontaneous and evoked synaptic transmission but normal synaptogenesis in the absence of Munc13-mediated vesicle priming. Proc. Natl. Acad. Sci. U. S. A *99*, 9037-9042.

Verhage,M., Maia,A.S., Plomp,J.J., Brussaard,A.B., Heeroma,J.H., Vermeer,H., Toonen,R.F., Hammer,R.E., van den Berg,T.K., Missler,M., Geuze,H.J., and Sudhof,T.C. (2000). Synaptic assembly of the brain in the absence of neurotransmitter secretion. Science

287, 864-869.

Voets,T., Toonen,R.F., Brian,E.C., de Wit,H., Moser,T., Rettig,J., Sudhof,T.C., Neher,E., and Verhage,M. (2001). Munc18-1 promotes large dense-core vesicle docking. Neuron *31*, 581-591.

Wang,X., Hu,B., Zimmermann,B., and Kilimann,M.W. (2001). Rim1 and rabphilin-3 bind Rab3-GTP by composite determinants partially related through N-terminal alpha -helix motifs. J. Biol. Chem. *276*, 32480-32488.

Wang,Y. and Sudhof,T.C. (2003). Genomic definition of RIM proteins: evolutionary amplification of a family of synaptic regulatory proteins. Genomics *81*, 126-137.

Wang,Y., Liu,X., Biederer,T., and Sudhof,T.C. (2002). A family of RIM-binding proteins regulated by alternative splicing: Implications for the genesis of synaptic active zones. Proc. Natl. Acad. Sci. U. S. A *99*, 14464-14469.

Wang,Y., Okamoto,M., Schmitz,F., Hofmann,K., and Sudhof,T.C. (1997). Rim is a putative Rab3 effector in regulating synaptic-vesicle fusion. Nature *388*, 593-598.

Wang,Y., Sugita,S., and Sudhof,T.C. (2000). The RIM/NIM family of neuronal C2 domain proteins. Interactions with Rab3 and a new class of Src homology 3 domain proteins. J. Biol. Chem. *275*, 20033-20044.

Weber,T., Zemelman,B.V., McNew,J.A., Westermann,B., Gmachl,M., Parlati,F., Sollner,T.H., and Rothman,J.E. (1998). SNAREpins: minimal machinery for membrane fusion. Cell *92*, 759-772.

Weimer,R.M., Richmond,J.E., Davis,W.S., Hadwiger,G., Nonet,M.L., and Jorgensen,E.M. (2003). Defects in synaptic vesicle docking in unc-18 mutants. Nat. Neurosci. *6*, 1023-1030.

Wu,M.N., Littleton,J.T., Bhat,M.A., Prokop,A., and Bellen,H.J. (1998). ROP, the Drosophila Sec1 homolog, interacts with syntaxin and regulates neurotransmitter release in a dosage-dependent manner. EMBO J. *17*, 127-139.

Xiao,W., Poirier,M.A., Bennett,M.K., and Shin,Y.K. (2001). The neuronal t-SNARE complex is a parallel four-helix bundle. Nat. Struct. Biol. *8*, 308-311.
Yamaguchi,T., Dulubova,I., Min,S.W., Chen,X., Rizo,J., and Sudhof,T.C. (2002). Sly1 binds to Golgi and ER syntaxins via a conserved N-terminal peptide motif. Dev. Cell *2*, 295-305.

Yang,B., Steegmaier,M., Gonzalez,L.C., Jr., and Scheller,R.H. (2000). nSec1 binds a closed conformation of syntaxin1A. J. Cell Biol. *148*, 247-252.

Zhang,X., Rizo,J., and Sudhof,T.C. (1998). Mechanism of phospholipid binding by the C2A-domain of synaptotagmin I. Biochemistry *37*, 12395-12403.

VITAE

Rong Guan was born in Cenxi, Guangxi Zhuang Autonomous Region, People's Republic of China on September 9th, 1977, a youngest daughter of Yongming Guan and Honglan Ye. After completing her work at Cenxi Middle School, Cenxi, Guangxi in 1995, she entered Nanjing University in Nanjing, Jiangsu. She received the degree of Bachelor of Science with a major in Biochemistry from Nanjing University in June, 1999. In June 2002, she received the degree of Master with a major in Biochemistry from Nanjing University. She entered the Graduate School of Biomedical Sciences at the University of Texas Southwestern Medical Center at Dallas in July, 2002. In May 2003, she joined Dr. Zhijian Chen's laboratory. In October 2004, she switched to Dr. Jose Rizo-Rey's laboratory. After five-year hard work, she was awarded the degree of Doctor of Philosophy in December 2007 from the Genetics and Development Program at the University of Texas Southwestern Medical Center at Dallas.

Permanent Address: 10 Alton Ct., Apt. 2
Brookline, MA 02446